

Hybrid Vision and Force Control in Robotic Manufacturing Systems

Bahar Ahmadi

A Thesis

in

The Department

of

Mechanical, Industrial and Aerospace Engineering

Presented in Partial Fulfillment of the Requirements

for the Degree of

Doctor of Philosophy (Mechanical Engineering) at

Concordia University

Montréal, Québec, Canada

July 2022

© Bahar Ahmadi, 2022

CONCORDIA UNIVERSITY

School of Graduate Studies

This is to certify that the thesis prepared

By: **Mrs. Bahar Ahmadi**

Entitled: **Hybrid Vision and Force Control in Robotic Manufacturing Systems**

and submitted in partial fulfillment of the requirements for the degree of

Doctor of Philosophy (Mechanical Engineering)

complies with the regulations of this University and meets the accepted standards with respect to originality and quality.

Signed by the Final Examining Committee:

Dr. Bruno Lee Chair

Dr. John Xiupu Zhang External Examiner

Dr. Brandon Gordon Examiner

Dr. Youmin Zhang Examiner

Dr. Wen-Fang Xie Supervisor

Approved by

Martin D. Pugh, Chair
Department of Mechanical, Industrial and Aerospace Engineering

August 18, 2022

Mourad Debbabi, Dean
Faculty of Engineering and Computer Science

Abstract

Hybrid Vision and Force Control in Robotic Manufacturing Systems

Bahar Ahmadi, Ph.D.

Concordia University, 2022

The ability to provide a physical interaction between an industrial robot and a workpiece in the environment is essential for a successful manipulation task. In this context, a wide range of operations such as deburring, pushing, and polishing are considered. The key factor to successfully accomplish such operations by a robot is to simultaneously control the position of the tool-tip of the end-effector and interaction force between the tool and the workpiece, which is a challenging task. This thesis aims to develop new reliable control strategies combining vision and force feedbacks to track a path on the workpiece while controlling the contacting force. In order to fulfill this task, the novel robust hybrid vision and force control approaches are presented for industrial robots subject to uncertainties and interacting with unknown workpieces. The main contributions of this thesis lie in several parts. In the first part of the thesis, a robust cascade vision and force approach is suggested to control industrial robots interacting with unknown workpieces considering model uncertainties. This cascade structure, consisting of an inner vision loop and an outer force loop, avoids the conflict between the force and vision control in traditional hybrid methods without decoupling force and vision systems. In the second part of the thesis, a novel image-based task-sequence/path planning scheme coupled with a robust vision and force control method for solving the multi-task operation problem of an eye-in-hand (EIH) industrial robot interacting with a workpiece is suggested. Each task is defined as tracking a predefined path or positioning to a single point on the workpiece's surface with a desired interacting force signal, i.e., interaction with the workpiece. The proposed method suggests an optimal task sequence planning scheme to carry out all the tasks and an optimal path planning method to generate a collision-free path between the tasks, i.e., when the robot performs free-motion (pure vision control). In the third part of the project, a novel multi-stage method

for robust hybrid vision and force control of industrial robots, subject to model uncertainties is proposed. It aims to improve the performance of the three phases of the control process: a) free-motion using the image-based visual servoing (IBVS) before the interaction with the workpiece; b) the moment that the end-effector touches the workpiece; and c) hybrid vision and force control during the interaction with the workpiece. In the fourth part of the thesis, a novel approach for hybrid vision and force control of eye-in-hand industrial robots is presented which addresses the problem of camera's field-of-view (FOV) limitation. The merit of the proposed method is that it is capable of expanding the workpiece for eye-in-hand industrial robots to cope with the FOV limitation of the interaction tasks on the workpiece. All the developed algorithms in the thesis are validated via tests on a 6-DOF Denso robot in an eye-in-hand configuration.

ACKNOWLEDGEMENTS

I would like to take the opportunity to greatly thank my supervisor, Dr. WenFang Xie for her nonstop supports, suggestions, and direction. I will always count on her to provide direction and support whenever I feel lost or stressed. I would like to thank her for all her contributions, guidance and encouragements. Hearty thanks also go to my colleagues and friends who accompanied me along these years: Ehsan Zakeri, Xinyi Wu, Pengcheng Li. I am also grateful to all those people who have given me support and I didn't have the chance to thank them. I ultimately would like to thank my lovely parents and my sister for their support, kindness and being always there, regardless of my choices, and for having allowed me, with their efforts, to get to where I am now. I would like to acknowledge the financial support from the Natural Sciences and Engineering Research Council of Canada (NSERC) throughout the course of this study and also Quanser Company for providing us with the experimental setup which brought a great value to this research.

Contents

List of Figures.....	ix
List of Tables	xi
NOMENCLATURES	xii
Abbreviation	xii
Symbols	xii
CHAPTER 1 INTRODUCTION	1
1.1 Introduction.....	1
1.2 Basic Principles.....	2
1.2.1 Visual Servoing.....	2
1.2.2 Force Control	5
1.3 A Review on Vision and Force Control.....	8
1.3.1 Hybrid IBVS/Force Control Methods.....	9
1.3.2 Hybrid Vision and Force Control for Multi-task Operations.....	10
1.3.3 Hybrid Vision and Force Control Dealing with Feature Loss	14
1.4 Research Objectives and Scopes.....	15
1.5 Contributions of the Thesis.....	16
1.6 Publications.....	18
1.7 Outline.....	19
CHAPTER 2 Cascade Vision and Force Control	20
2.1 Introduction.....	20
2.2 System Modeling	21
2.2.1 Visual Servoing Modeling	22
2.2.2 Force Modeling.....	25
2.3 Robust Cascade Vision and Force Control Method.....	26
2.3.1 Desired Image Feature Extraction.....	26
2.3.2 Cascade Vision and Force Controller Design Using CISMV	28
2.3.3 Contacting Detection and Managing the Robot’s Task	30
2.3.4 Stability Analysis	32
2.4 Experimental Results and Discussion.....	37
2.4.1 Extraction of Desired Image Features.....	38
2.4.2 Test 1: Free-motion and Hybrid Vision and Force Task.....	40
2.4.3 Test 2: Interaction with a Curved Workpiece	42

2.5	Summary.....	46
CHAPTER 3 Optimal Image-Based Task-Sequence and Path Planning.....		47
3.1	Introduction.....	47
3.2	Problem Statement.....	49
3.3	Image-Based Task Sequence and Path Planning	50
3.3.1	Optimal Task-Sequence and Path Planning	51
3.3.2	Mapping From Cartesian Space to Image Plane.....	60
3.4	Hybrid Vision and Force Controller Design	62
3.4.1	Variable-Gain Orthogonal Sliding Manifold.....	62
3.4.2	Filtered Quasi Sliding Mode Controller.....	65
3.5	Experimental Results and Discission.....	70
3.5.1	Result of Training the Neural Network.....	70
3.5.2	Design of the Experimental Test.....	71
3.5.3	Results and Discussion of the Experimental Tests	73
3.6	Summary.....	87
CHAPTER 4 Multi-Stage Vision and Force Control.....		90
4.1	Introduction.....	90
4.2	Multi-Stage Vision and Force Control Design.....	91
4.2.1	Vision Motion Decomposition.....	91
4.2.2	Stages of the Proposed Method.....	92
4.2.3	Switching stage supervisor.....	94
4.3	Super-Twisting Sliding Mode Controller.....	95
4.3.1	Variable-gain Sliding Surface	96
4.3.2	Deriving STSMC Law	97
4.4	Experimental Results	99
4.5	Summary.....	101
CHAPTER 5 Expansion of IBVS Workspace		103
5.1	Introduction.....	103
5.2	Problem Statement.....	105
5.2.1	Modeling of the Vision System	106
5.2.2	Modeling of Interaction Force	107
5.3	Extracting the Desired Image Features Trajectories Using Learning-From-Demonstration Method.....	108
5.4	Designing Hybrid Vision and Force Control Using Hierarchical Sliding Mode Control Method	
	112	

5.4.1	Hierarchical Sliding Surface	113
5.4.2	Continuous Integral Sliding Mode Control.....	116
5.5	Experimental Results	121
5.5.1	First Experiment.....	121
5.5.2	Second Experiment	125
5.6	Summary	128
CHAPTER 6 Conclusion and Future Works		130
6.1	Summary of the Thesis	130
6.2	Future Work.....	133

List of Figures

Figure 1.1: Visual servoing applications: a) Car steering [88], b) Fruit picking [86], c) Medical surgery [87], d) Grasping object on conveyer belts [85]	2
Figure 1.2: PBVS structure	3
Figure 1.3: IBVS structure	4
Figure 1.5: Hybrid vision and force control [7]	8
Figure 2.1: a) The 6-DOF robot equipped with a force sensor and an EIH camera, b) Feature points.	22
Figure 2.2: a) Decomposition of S_d , b) Collecting image features data while moving on the desired path.	26
Figure 2.3: a) Schematic of the proposed robust cascade vision and force controller, b) Detection of contact with the workpiece and automatic activation and deactivation of the force controller.	28
Figure 2.4: Experimental setup.	38
Figure 2.5: Desired path in cartesian space: a) Test 1, b) Test 2, Extracted desired features in image space: c) Test 1, d) Test 2.	40
Figure 2.6: Control process of test 1 using the proposed method.	41
Figure 2.7: Results of Test 1: a) Image feature tracking, b) 2D mage feature tracking, c) Force control. .	43
Figure 2.8: Results of Test 2: image feature tracking a) S_1 to S_3 , b) S_4 to S_6 , c) 2D-image path tracking, d) Norm of four image features.....	44
Figure 2.9: Results of test 2 force control.....	44
Figure 2.10: Desired path in cartesian space: a) Test 1, b) Test 2, Extracted desired features in image space: c) Test 1, d) Test 2.	45
Figure 3.1: Task sequence planning: a) In the workspace, b) In the image plane.	53
Figure 3.2: Rotational potential force.	57
Figure 3.3: a) The three-layer NN, b) P_d , P_{DF} , and P_{dI}	62
Figure 3.4: Schematic of the proposed robust hybrid controller.....	67
Figure 3.5: Training the NN.....	71
Figure 3.6: Op. 1-Desired paths and points of four tasks on the workpiece	76
Figure 3.7: The robot operating Op. 1.	76
Figure 3.8: Path tracking in the image space and force control of all the tasks of OP. 1: a) Tracking the paths and points in the image space of Op. 1, b) Controlling the force of Op. 1.....	76
Figure 3.9: Op. 2: a) Desired paths and points of three tasks on the workpiece using APF method, b) Desired paths and points of three tasks on the workpiece using MAPF method.	78
Figure 3.10: The robot operating Op. 2.	78
Figure 3.11: Path tracking in the image space and force control of all the tasks of OP. 2: a) Tracking the paths and points in the image space of Op. 2, b) Controlling the force of Op. 2.....	78
Figure 3.12: The robot operating Op. 3.	80
Figure 3.13: Path tracking in the image space and force control of all the tasks of OP. 3, a) Tracking the paths and points in the image space of Op. 3, b) Controlling the force of Op. 3.....	80
Figure 3.14: Op. 3 (a) Desired paths and points of three tasks on the workpiece using APF method, b) Desired paths and points of three tasks on the workpiece using MAPF method.	80
Figure 3.15: Op. 4: a) Desired paths and points of two tasks on the workpiece using APF method, b) Desired paths and points of three tasks on the workpiece using MAPF method.	81
Figure 3.16: The robot operating Op. 4.	82
Figure 3.17: Path tracking in the image space and force control of all the tasks of OP. 4: a) Tracking the paths and points in the image space of Op. 4, b) Controlling the force of Op. 4.....	82

Figure 3.18:Op. 1-Desired paths and points of four tasks on the workpiece	84
Figure 3.19: Test 5: a) Desired path on the workpiece, b) Corresponding feature.	86
Figure 3.20:Tracking image features of the third test: a) x , b) y , c) af , d) Sx , e) Sy f) θf	86
Figure 3.21: Force control of the third test.	86
Figure 3.22: Robot joint velocities (test 3): a) SMC, b) P/PI, c) FQSMC.....	87
Figure 4.1: Different stages of the proposed strategy.	95
Figure 4.2: Schematic of the proposed hybrid vision and force control method.	98
Figure 4.3: The control process of the experiment using the proposed method.	100
Figure 4.4: Results of the experiment: image features: a) P/PI, b) STSMC, Norms: c) P/PI, d) STSMC, Interacting force: e) P/PI, f) STSMC.	101
Figure 5.1: Six-DOF industrial robot equipped with a force sensor and camera with EIH configuration interacting with a planar workpiece containing an array of image objects.	106
Figure 5.2: a) The schematic of the proposed FIS, b) Membership functions.....	112
Figure 5.3: Desired feature loss at the beginning of IBVS and trajectory tracking by free motion to converge to ksA	116
Figure 5.4: Schematic of the proposed robust hybrid controller.....	118
Figure 5.5: a) Workspace for one image object, b) Workspace for two image object, c) Workspace for four image object, d) Workspace for six image object, e) Workspace for twelve image object, f) Workspace for eighteen image object.....	122
Figure 5.6: a) Data collecting process by the robot for generating the desired image signal; b) Desired obtained signals.....	123
Figure 5.7: a) Robot operating the first test along with the captured image features in real time, b) Tracking the desired path and tracking the desired force signal.	124
Figure 5.8: Robot operating the second test along with the captured image features in real time when the desired feature is not available in the FOV.....	126
Figure 5.9: a) Tracking the desired vision signal using CISMCM compared with the P/PI and SMC b) Tracking the desired force signal using the P/PI, SMC and CISMCM.....	127

List of Tables

Table 2.1. System's physical parameters.	38
Table 2.2: The computed indices for vision and force control in test 2.	45
Table 3.1: The optimized parameters for MAPF-CGTSP using MTOA.	74
Table 3.2: Results of the different optimization algorithms for all operations expressed in meters (m). ...	83
Table 3.3: The computed values of the indicators for the norms of system errors of the third test.	87
Table 3.4: The computed values of the indicators for the controller output of the third test.	87
Table 4.1: The indicators' values for the experimental test.	101
Table 5.1: The computed values of the indicators for the norms of system errors of the third test.	128

NOMENCLATURES

Abbreviation

IBVS	Image-based visual servoing
EIH	Eye-in-hand
ETH	Eye-to-hand
CISMC	Continuous integral sliding mode control
MSTA	Modified super twisting algorithm
CDA	Contact detector algorithm
DOF	Degree of freedom
MAPF	Modified artificial potential field
MAPF-CGTSP	MAPF-constrained-generalized-traveling-salesman-problem
MTOA	Multi-tracker optimization algorithm
FQSMC	Filtered quasi sliding mode controller
VGOSM	Variable-gain orthogonal-sliding-manifold
FOV	Field of view
FIS	Fuzzy Interface System
STSMC	Super-twisting sliding mode controller

Symbols

F_c	Camera frame
S	Image features
f	Focal length
P_{ci}	Coordinates of the i^{th} feature point with respect to the camera frame
$[X_{ci} \ Y_{ci} \ Z_{ci}]$	Coordinates of the i^{th} feature point with respect to the camera frame

\dot{s}_i	The time derivative of the i^{th} image feature
V	The velocity screw of the camera
L_{s_i}	The interaction matrix
l_{CE}	Distance between camera frame and feature points in normal direction
\bar{S}	Modified image features
\bar{L}_s	Modified interaction matrix
J_q	The robot Jacobian matrix
\dot{q}	The vector of joint velocities
$\bar{\Delta}_s$	The uncertain part of the vision model
K_f	The nominal stiffness between the workpiece surface and tool-tip
P_f	The displacement of the tool tip in its normal direction
F_z	The exerted normal force to the tool tip
$\bar{\Delta}_F$	The uncertain part of the force model
\bar{S}_d	The desired vector of image features
\bar{S}_{dn}	The normal desired vector of image features
\bar{S}_{dt}	The tangential desired vector of image features

CHAPTER 1 INTRODUCTION

1.1 Introduction

Nowadays, robotic systems have been widely used in industrial applications such as automotive industry, aerospace industry and composite manufacturing, etc. However, they are generally limited to operate in structured (the environment with known and calibrated parameters) environments. Conventional robots use open-loop kinematic calculations to determine the end effector position with respect to a known reference frame. The target object position must also be known with respect to the same coordinate frame. The issue is that any uncertainty of the relevant parameters would cause the task to fail. Vision sensors can deal with these uncertainties by providing non-contact and real time measurements of the environment to determine position of the end-effector and target object with respect to each other and the reference frame. Closed-loop position control of the end-effector by exploiting the vision signal as a feedback is referred to as visual servoing [1]. As the tasks become complicated, it poses challenges to the robot control design, which needs to integrate the information from various sensors and to generate control commands not only to control the position of the end-effector but also the interaction force between the end-effector and the environment. Position/force control is the topic that is frequently studied in the recent years. Due to the increasing development of robotic tasks in industrial applications such as polishing, deburring, pounding, polishing, grinding, twisting, cutting and excavating.

1.2 Basic Principles

In this subsection, the basic principles of the visual servoing and force control are presented. The basics and classifications of visual servoing will be introduced first and followed by those of the force control.

1.2.1 Visual Servoing



Figure 1.1: Visual servoing applications: a) Car steering [88], b) Fruit picking [86], c) Medical surgery [87], d) Grasping object on conveyer belts [85]

Visual Servoing is an approach to controlling the motion of a robot manipulator using visual feedback signals. Visual servoing robot takes advantage of the vision captured by a camera to acquire the accurate positions of the target objects and the end-effector and uses it as a feedback for controlling system. In visual servoing, the robot uses the image captured by the camera to determine the position of the end effector and the target object and uses it as feedback to control

the position of the robotic system. Visual servoing has been adopted in a wide range of applications such as robotic welding, teleoperation, missile tracking cameras, fruit picking, robotic ping-pong, juggling, car steering and even aircraft landing [1] (Figure 1.1).

Position Based Visual Servoing (PBVS)- In this method, the pose of the target object is obtained with respect to the camera by using the image features. The errors of position and orientation can be computed by comparing the current and desired target position and orientation in the Cartesian frame. So, the important benefit of PBVS is to control the pose of end-effector directly in the Cartesian space. However, this control scheme has some drawbacks. First, a tedious vision system calibration is required. Second, in order to measure the target position, an accurate geometric model of the system is required [2].

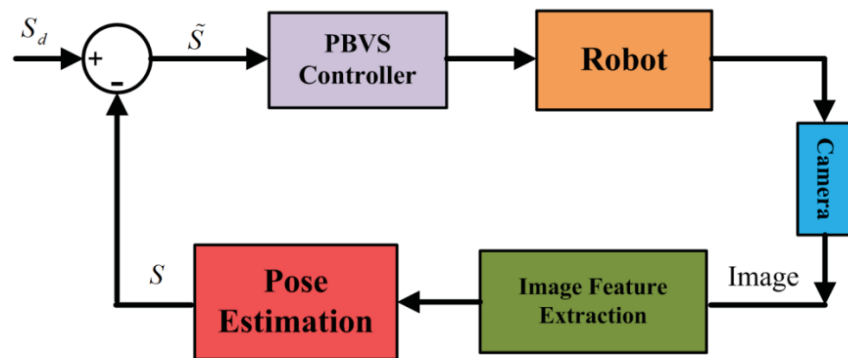


Figure 1.2: PBVS structure

Image Based Visual Servoing (IBVS)- In this method, the feature error signal which is used for generating the control signal is obtained directly in the image space. Different types of image features have been used in the literature [3] including an area size, an area length, the center point of a region and so on. The benefits of this visual servoing approach are listed as follows [4]:

1. In contrast to position-based method, no image processing and calculation of pose is needed in this method which allows using high sampling rate for real time control.

2. Since this method does not require a full model of the target, no camera calibration is required and also the errors due to target model uncertainties would be reduced.

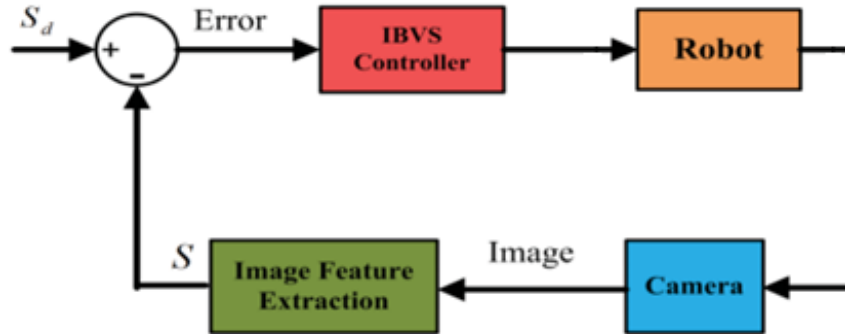


Figure 1.3: IBVS structure

Hybrid Visual Servoing (HVS)- This technique combines the advantages of 2-D (pixel-space) and 3-D (task-space) visual servoing feedback to guarantee the stability in a large displacement servoing. More precisely, it is based on estimation of the camera displacement (the rotation and translation of the camera) between the current and desired image features. Comparing with other techniques, this method owns stronger robustness to the calibration error. Moreover, the trajectories of end effector in both the Cartesian and image spaces are simultaneously straight lines. In addition, this method is known as a target model free method [5]. Nevertheless, there are some shortcomings for hybrid system. First, it is necessary to find at least 4 and 8 different feature points for a planar and non-coplanar target object respectively. Second, it also requires partial pose estimation. Third, it still needs to consider the image boundary and robot singularity.

1.2.2 Force Control

The ability to provide a physical interaction between a robot and the environment is a crucial issue for a successful manipulation. In the tasks where the robot is in contact with the environment, even a small change in the trajectory will lead to operation failure and damage to the work-piece.

Thus, force controllers play a fundamental role in performing the tasks in an unstructured environment. An accurate model of manipulator kinematics, dynamics and environment geometry is required in order to succeed in fulfilling the interaction tasks. Force control is normally classified into two groups: active and passive control [6]. The passive strategy is very simple and ease to implement because they do not require force/torque sensors. Nevertheless, passive strategy lacks the flexibility in industrial applications due to the limitation on dealing with position and orientation deviations of the trajectory. Also, due to the lack of force sensors which can provide the force signal, it cannot avoid the high contact forces occurring, which may lead to collision. The basic principle of active force control is based on regulating the energy to actuators. In this approach, the desired trajectory of the manipulator is generated by measuring the contact force and providing feedback to the controller. The aforementioned problems with passive force control can be overcome by using active interaction control, but the design process of the active control is more complicated than that of the passive one [7]. Also, the implementation of such control system is more expensive and the computation load is heavier. Therefore, active force control strategy has been designed in integration with some degrees of passive method to achieve a more satisfactory performance [8]. The active force control can be categorized in two classes: indirect force control and direct force control [7].

1.2.2.1 Indirect Force Control

In the indirect force control, there is no need to close the force feedback loop and the controlling force interaction between the manipulator and the environment is done via motion control. Impedance and Admittance control are two types of force indirect control strategy. In indirect strategies, the contact force is related to the deviation of end effector motion from the desired motion through a mechanical impedance/admittance.

Impedance Control- One of the mostly used indirect force controllers is the impedance control [9]. This type of force control is designed to regulate the mechanical impedance of the robot. After measuring the user's motion signal by the impedance control, a force feedback signal will be provided to the operator (i.e. the operator velocity is used to drive the output force). So, the impedance of the manipulator is defined as the connection between input velocity and the applied force. Impedance control is normally used in high speed applications in order to provide a stable contact with the object surface [10]. The simplest form of impedance control is stiffness control which provides a relation among output force, input displacement and stiffness [11]. The dynamic model of the robot is required to address the stability issue in impedance control. Thus, both the robot and the environment are modeled as an equivalent mass-spring-damper system with adjustable parameters.

Stiffness Force Control- Stiffness control is a fundamental type of force control, which smooths the effects of end-effector forces simulating spring properties. In order to compensate the orientation errors, the mechanical parts including springs and dampers can be exploited. Also, it is possible to turn the stiffness control into a programmable spring by having a closed-loop force feedback.

Admittance Control- Admittance control differs from impedance control in the way reacting to the motion deviation. In this type of force control, the forces exerted by the user are measured by the admittance control and then the commanded input is fed back in the form of velocity. By adjusting the stiffness and the damping matrices, the end-effector velocity command signal can be changed. One possible solution to developing an admittance force control is provided in [4]. Admittance control shows that the desired performance is achieved by using force outer loops and an inner position or velocity loop.

1.2.2.2 Direct Force Control

Hybrid force/motion control- The general scheme of hybrid force/motion control is proposed by Raibert and Craig [12]. This type of control strategy is based on controlling the motion along the unconstrained task directions and force along the constrained task directions. Thus, the system presents two separated control loops for motion and force, respectively. Therefore, in those directions assigned to the motion control, the current position/velocity is determined, whereas in the directions assigned to the force control, the interaction forces between the robot and the environment are controlled.

Explicit Force Control- In this method, the desired and measured force signals are compared to generate the force errors and to provide an actuation input to the system. The ideal option for explicit force control is the integral control due to its simple structure, low pass nature and its stability. However, the problem with this type of controller is that it tends to become unstable. Therefore, any force controller using the derivative of force signal is not suitable since it works as a band pass filter for the natural frequency of the system. Furthermore, the time derivative of force input contains a lot of noises.

1.3 A Review on Vision and Force Control

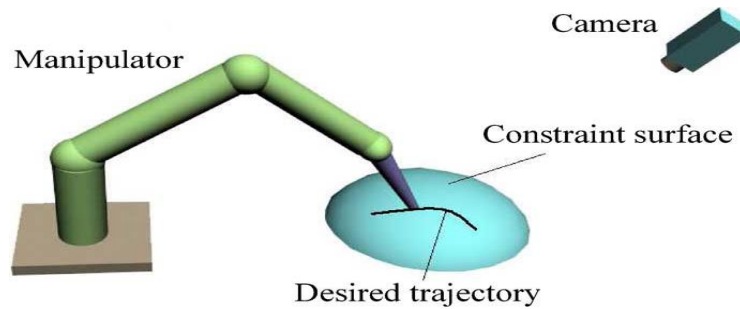


Figure 1.4: Hybrid vision and force control [7]

Two main approaches for controlling the end effector position while interacting with a workpiece are the impedance/admittance control and hybrid position/force control [13]-[15] (Figure 1.4). In the former approach, the relation between the force and position of the tool is derived and both force and position are controlled simultaneously. However, there is a trade-off between controlling force and position, which means neither force nor position converges towards its desired reference, and thus results in low precision [13], [16]. However, in the hybrid position/force control approach, the force and the position are controlled separately [15]-[17]. In lots of research work, the orthogonality principle is employed to decompose the constraint surface into the constrained directions where the force and the motion are controlled on the workpiece [15], [16]. The performance of a robotic system in fulfilling such tasks is largely dependent on the accurate model of the robot and knowledge of environment. Since the everyday environment and the workpiece may be subjected to change, it is not easy or practical to get an exact model. Therefore, the major problem of hybrid position/force control lies in the need for exact knowledge of the physical model of the robot and workpiece, which might be inaccessible [15]-[17].

1.3.1 Hybrid IBVS/Force Control Methods

To cope with the problems of using position/force method, the combination of image-based visual servoing (IBVS) with force control, as hybrid vision and force control method, has been suggested [16]-[18], [21]-[24]. In this method, the image features are controlled in the image plane to track the desired image features corresponding to the desired path on the constrained surface. Therefore, regardless of the physical properties of the surface, the camera detects the image points on the surface and tracks the corresponding image features, which is equivalent to tracking the desired path on the unknown constraint surface [16]. Although IBVS can tackle the problem of the uncertainties of the constraint surface, the uncertainties in the vision model such as the interaction matrix may deteriorate the control performance [17] and even cause instability. Besides, the uncertainties in kinematics or dynamics of the robot itself may result in undesirable control performance such as low precision, chattering, and slow convergence. This may limit the extensive use of robots for applications in industries. For instance, the tool tip may generate some vibration disturbance in contact with the surface of the workpiece or may be guided to the wrong place which results in poor productivity or even damaging the workpiece or the robot. To handle this issue, adaptive control methods have been suggested [16]-[18]. In [17], an adaptive hybrid vision and force controller is proposed. The adaptive part estimates the existing uncertainties in kinematics, dynamics of the robot, and image interaction matrix to improve the performance of the control process. In [18], a neural network-based hybrid vision and force control method is proposed, where the neural network estimates the constraints of the surface adaptively. In [16], an adaptive hybrid vision and force control method is presented to deal with the uncertainties in robot dynamics, camera model, and constraint surface, while dead-zone input is considered. Despite the effectiveness of the proposed adaptive methods, some major issues still exist. The control methods

employ the estimated parameters to generate the control signals, which may introduce low convergence speed and tracking precision. To avoid this issue, robust methods, solely or in combination with adaptive methods, are suggested [25], [26]. Also, in most cases, eye-to-hand (ETH) camera configuration is employed which solve the problem with the uncertainty of the workpiece position. However, the uncertainty of constraint surface still remains unaddressed. In these studies, by assuming a frictionless contact between the tool-tip and the surface, the angle of the contact relative to the surface is estimated, which may not be accurate. It is worth noting that some limited studies have suggested using IBVS with eye-in-hand (EIH) camera, which handles the uncertainty issue of the constraint surface [24]. However, the system uncertainties are not considered and the stability proof of controller is not provided. Besides, due to the lack of a practical method for extracting the image features corresponding to the desired path in 3D space, the current studies on eye-in-hand IBVS have mainly focused on regulation on some specific points on the workpiece. Another common issue in IBVS lies in a non-invertible image interaction matrix, which results in the IBVS with local stability [19], [20]. In [20], SMC is adopted for IBVS in a free-motion task which can only guarantee the local stability when the model of the visual system is subject to uncertainties. In [21], SMC is utilized to design a robust vision and force control considering both dynamics and kinematics uncertainties. However, the unknown constraint surface and the uncertainties of the vision system are not considered in the context of robust hybrid force/vision control.

1.3.2 Hybrid Vision and Force Control for Multi-task Operations

In many industrial robotic operations such as spot welding, milling, drilling, and electrical circuit soldering, the robot may need to interact with the workpiece several times on different paths or points, each of which can be considered as a task [27], [28]. To carry out such a multi-task

operation, one solution is to consider each task as an individual operation. Then, the operator will program the robot to perform each task one-by-one, i.e., manual task planning. Although widely used, this method is time-consuming, and the operator's mistakes may result in a collision and damaging the workpiece. Therefore, planning an optimal sequence of the tasks and generating a collision-free path for performing free motion between the tasks are crucial for industrial manufacturing to gain high productive, low cost, efficient, and safe operations [29].

The task sequence planning aims at determining the order of performing the tasks in a way that the overall operation time duration is minimized. Usually, the task sequence problem is defined as a traveling salesman problem (TSP) whose solution is the optimal sequence of the tasks. Depending on the tasks' types and constraints, different types of TSP problems, such as standard TSP [30], generalized TSP [31] and clustered TSP can be defined [27]. In [30], the task sequence problem of a fruit picking operation is addressed. To this end, the problem is directly formulated and solved as a standard TSP. In [31], robotic multi-hole drilling operation is addressed, where the robot task sequence problem is considered as a modified generalized TSP. In [27], a clustering-based TSP algorithm is used to solve the task sequence problem of a robot manipulator for a large number of target points and greater spatial constraints in a cluttered environment. In these studies, the operational areas are assumed to be free of obstacles. In real operations, however, several obstacles may exist in the robot workspace. Therefore, the lack of designing a suitable path planning method between the tasks may result in collision or generation of non-optimal paths.

Path planning involves the strategy of generating the shortest path between the initial and destination positions while avoiding the obstacles under several constraints. Among different methods of path planning, artificial potential field (APF) method is one of the most well-known and feasible methods for generating a collision-free path. The basic concept of the APF method

requires filling the activity area with the artificial potential field in which the agent is attracted to its target position, and is repulsed away from the obstacles and other agents [33]-[35]. In [33], a non-collision trajectory planning strategy based on APF is developed for path optimization of serial robots. In [34], a path planning method is proposed with an APF method for redundant robots. In [35], a new strategy is developed for assessing the collision risk and avoiding it using an APF and the fuzzy inference system. Although conventional APF is very effective for obstacle avoidance, it suffers from major drawbacks, the most important of which is trapping in local minima. This phenomenon is the result of aligning the repulsive and attractive force but in the opposite direction. Several approaches have been presented to address this problem. In [39], a new technique is employed to add repulsive force normal to the direction of attractive force which provides more flexibility for the APF method and results in the escaping from a local minimum. Another solution is to use metaheuristic optimization algorithms to set the parameters of the APF, to find a short path that reaches the target. In [38], a repulsive potential field is proposed by considering the relative distance between the robot and the target. Then it is optimized by using particle swarm optimization (PSO) to find the APF parameters in a way that an optimal path between the target and the departure point is generated. In [36] a dynamic membrane method combined with the pseudo-bacterial genetic algorithm for adjusting the parameters of APF is introduced to enhance the optimization procedure. In [37], a membrane evolutionary artificial potential field approach was proposed to solve the mobile robot route planning problem, which combines membrane computing with a genetic algorithm and the artificial potential field method to find the parameters to generate a feasible and safe route. The results show the superiority of the proposed method to the others.

Although all these studies have shown successful results, they are only applicable to single task operations. However, in [32], an integrated path planning and task sequencing approach is presented for robotic remote laser welding (RLW) operation, which is a multi-task operation. A TSP with neighborhoods and durative visits (TSP-ND) is defined to find the optimal path and sequence of tasks. However, the proposed method cannot be adopted when physical interaction with the workpiece is required. In addition to the path/sequence planning problem, interaction with a workpiece by an industrial robot is a challenging task that entails simultaneous control of the position of the end-effector and interaction force [36]. To handle this issue, hybrid vision and force control has been suggested, in which a vision system provides non-contact measurement of some features of the workpiece or the end-effector [41]-[44]. Note that for hybrid vision and force manipulation with multiple tasks, the task-sequence/path planning must be carried out in the image feature space. Lots of research has been devoted to path planning in image space for pure visual servoing with different objectives [45], [46]. In [45], a path planning method is coupled with IBVS that suggests a modification of the projective interpolation algorithm to ensure the visibility of the target, while the camera calibration is not required. In [46], an image-based trajectory planning algorithm is proposed to avoid the problems caused by the camera's field of view of IBVS methods by parametrizing the camera velocity screw utilizing time-based profiles. However, integrating task sequence/path planning with the vision and force control is a challenging task. The reason is that the planning must be done in Cartesian space to gain an optimal path and avoid the collision, while in IBVS, the image feature feedback is employed, and the position of the end-effector cannot be measured directly in real-time. The fulfillment of the task demands a feasible method to map any arbitrary desired trajectory from Cartesian space to image feature space. It is noted that some mapping methods have been proposed such as learning by demonstration and spline fitting [47],

[48]. However, these techniques cannot be utilized to map the specified paths as it is required for task sequence/path planning. In [47], a spline method has been developed to transform the desired trajectory from Cartesian space to the desired trajectory in image space. However, in this method, a new desired image feature path is required to be extracted corresponding to every different desired pose in the Cartesian space. The same method is suggested in [48]. However, no fitting method is used and the smoothed signals in the feature space are utilized instead. In addition to the mapping method, a technique should be integrated with the overall control law for managing the switching between the interaction and free-motion tasks. By employing such an algorithm, the robot can touch the surface or detach from it at the beginning and end of each task.

1.3.3 Hybrid Vision and Force Control Dealing with Feature Loss

Another major issue is the FOV limitation of the traditional IBVS method. However, some research work in visual trajectory planning is presented to cope with FOV constraints and feature loss problem. [49] presented an extensive overview of the path-planning strategies used in visual servoing to guarantee occlusion-free trajectories, as well as to consider FOV limitations. In [54], an enhanced switch image-based visual servoing method is suggested in which a Kalman filter-based feature prediction algorithm is employed and combined with switch IBVS to make the switch IBVS control robust in reaction to feature loss. The feature prediction algorithm can predict the lost feature points based on the previously estimated points. Also, some studies have been carried out in visual trajectory planning considering feature loss avoidance [50]-[53]. In [50], a model predictive control method is employed in visual servoing to prevent feature loss. Despite the success of these studies on dealing with feature loss for pure visual servoing control, the FOV limitation is not investigated for the hybrid vision and force control. Also, the proposed strategies suffer from the limited maneuvering workspace of the robot, due to the conservative design

required to satisfy many constraints. In hybrid vision and force control methods with EIH configuration, the end-effector needs to be in the closest distance to the workpiece's surface such that the tool touches the surface for interaction. Consequently, the FOV will be too small which limits the robot's workspace and also may lead to moving the image features points out of the FOV, i.e., feature loss, which results in failure of the manipulation task.

1.4 Research Objectives and Scopes

Industrial application of vision and force control in many cases requires high speed of the task and adequate robustness to uncertainties and also camera limitations. The uncertainties include those in the vision model such as the interaction matrix, in kinematics or dynamics of the robot, the force model uncertainties and the main camera limitation is its FOV. Thus, the main objective of this thesis is to develop a series of new vision and force methods to simultaneously increase the speed of the task, improve its robustness to the mentioned uncertainties and limitations while keeping the stability of the controller and also enabling the robot to accomplish the multi-task operation successfully. In addition, this thesis aims to find the solution to expand the workspace to prevent the feature loss problem. The objectives and scopes of this thesis can be summarized as follows:

1. Presenting a robust cascade vision and force approach consisting of an inner vision loop and an outer force loop to control industrial robots interacting with unknown workpieces.
2. Developing a novel image-based task-sequence/path planning scheme coupled with a robust vision and force control method for solving the multi-task operation problem of an industrial robot interacting with a workpiece.
3. Developing a novel approach for hybrid vision and force control of eye-in-hand industrial robots which addresses the problem of FOV limitation.

1.5 Contributions of the Thesis

This PhD research work is carried out in different stages. The contributions of each stage of the research work are summarized as follows:

First, a robust cascade vision and force approach is designed to control industrial robots interacting with unknown workpieces considering model uncertainties. This cascade structure, consisting of an inner vision loop and an outer force loop, avoids the conflict between the force and vision control in traditional hybrid methods without decoupling force and vision systems. To apply an advanced image-based visual servoing (IBVS) compensator, some newly modified image features are used which render an invertible image interaction matrix. A practical task-based method is proposed to extract the features corresponding to the desired path in 3D space. A robust continuous integral sliding mode control method (CISMC) is developed for both IBVS and force compensators. CISMC exploits advantages of the modified super twisting algorithm (MSTA) to reduce the chattering. The stability of the proposed cascade controller is proved. Additionally, a contact detector algorithm (CDA) is developed to manage the robot's free motion and its interaction with the workpiece.

Second, a novel image-based task-sequence/path planning scheme coupled with a robust vision and force control method is suggested for solving the multi-task operation problem of an eye-in-hand (EIH) industrial robot interacting with a workpiece. The proposed method suggests an optimal task sequence planning scheme to perform all the tasks and an optimal path planning method to generate a collision-free path between the tasks when the robot performs free-motion. To this end, a new method is presented which solves both problems simultaneously. A novel deadlock-free modified artificial potential field (MAPF) based on rotational potential force is developed for generating the collision-free path between tasks in

the three-dimensional (3D) environment. The parameters of the MAPF and the sequence of the tasks are found by an optimizer simultaneously. This problem can be considered as a MAPF-constrained-generalized-traveling-salesman-problem (MAPF-CGTSP), which is a mix-integer optimization problem. The mix-integer version of multi-tracker optimization algorithm (MTOA) is developed to solve the problem. However, since image-based visual servoing (IBVS) is used for motion control, the planning is conducted in the image space. Integrated with the proposed planning method, a novel chattering-free filtered quasi sliding mode controller (FQSMC) is specially designed for robust vision and force control of the robot. FQSMC exploits a novel variable-gain orthogonal-sliding-manifold (VGOSM) which enables the robot to switch between free-motion mode and interaction mode. FQSMC overcomes large uncertainties and filters out the existing noises by exploiting an intrinsic filter within its control law.

Third, a novel multi-stage method for robust hybrid vision and force control of industrial robots, subject to model uncertainties is proposed. It aims to improve the performance of the three phases of the control process: a) free-motion using the image-based visual servoing (IBVS) before the interaction with the workpiece; b) the moment that the end-effector touches the workpiece; and c) hybrid vision and force control during the interaction with the workpiece. First, the camera motion is decomposed into transitional and angular movements. Then, utilizing a switching method, the rotational and translational movements of the camera are controlled in the first two stages, respectively. In the last stage, hybrid vision and force control is activated. For each stage, super-twisting sliding mode controller (STSMC) is utilized. Employing STSMC results in robustness against uncertainties while addressing the chattering problem. A variable-gain sliding surface is also proposed to address the instability and

convergence speed issues of the traditional switch IBVS. The experimental results demonstrate the effectiveness and superiority of the proposed multi-stage method compared to other traditional approaches.

Fourth, a novel approach for hybrid vision and force control of eye-in-hand industrial robots is presented which addresses the problem of camera's field-of-view (FOV) limitation. During the interaction with the workpiece, the distance of the camera and the workpiece's surface is rather short. Thus, the FOV is very small which restricts the robot's workspace. To handle this issue, instead of using only a feature object, an array of objects is provided on the workpiece in a way that at least one object is entirely in the FOV at each time step. However, conventional IBVS cannot be employed for hybrid vision and force control of such tasks. Thus, for this purpose, using a fuzzy inference system (FIS) and orthogonality principle, a novel hierarchical sliding surface is devised, and the continuous integral sliding mode controller (CISMC) is adopted, which leads to a robust and precise control method, applicable to the mentioned task. The stability of the proposed method is also proved. Additionally, a method based on the virtual desired image features is devised for the free motion before starting the interaction when the robot is not fully convergent.

The performance of all the proposed methods is examined by experimental tests on a 6-DOF robot manipulator with an EIH vision system and their performance is compared with that of traditional methods.

1.6 Publications

The presented research work is published (or submitted for publication) in some journals and conferences. Following is the list of author's contributions followed by the related publications.

- **Journal Papers**

1. B. Ahmadi, W. -F. Xie and E. Zakeri, "Robust cascade vision/force control of industrial robots utilizing continuous integral sliding mode control method," in IEEE/ASME Transactions on Mechatronics, doi: 10.1109/TMECH.2021.3067619
2. B. Ahmadi, E. Zakeri and W. -F. Xie, "Optimal Image-Based Task-Sequence/Path Planning and Robust Hybrid Vision/Force Control of Industrial Robots," in IEEE Access, vol. 10, pp. 26347-26368, 2022, doi: 10.1109/ACCESS.2022.3156919.
3. B. Ahmadi, W. -F. Xie and E. Zakeri, "Expansion of the workspace of an eye-in-hand industrial robot for hybrid vision/force control," Submitted to International Journal of Control, Automation and Systems, 2022.

- **Conferences**

4. B. Ahmadi, W. -F. Xie and E. Zakeri, "Robust multi-stage hybrid vision/force control of industrial robots," 2021 IEEE International Conference on Multisensor Fusion and Integration for Intelligent Systems (MFI), 2021, pp. 1-6, doi: 10.1109/MFI52462.2021.9591190.

1.7 Outline

This thesis starts with an introduction and literature review on hybrid vision and force along with the research scope and objectives of the thesis. In Chapter 2, the cascade vision and force method is presented. In Chapter 3, the optimal image-based task-sequence/path planning integrated with the hybrid vision and force control is introduced. In Chapter 4, a multi-stage vision force control strategy is developed. In Chapter 5, the expansion of the workspace of an eye-in-hand industrial robot for hybrid vision and force control is proposed. Finally, the conclusion and future work are explained in Chapter 6.

CHAPTER 2 Cascade Vision and Force Control

2.1 Introduction

This chapter presents a robust cascade vision and force approach to control industrial robots interacting with unknown workpieces considering model uncertainties. It enables the tool tip to track a path on the workpiece while controlling the contacting force. This approach adopts a cascade structure which comprises two feedback loops: inner vision feedback loop and outer force feedback loop. The main advantage of such a cascade structure is that the inner loop focuses on visual servoing and handling the existing uncertainties associated with the robot kinematics, workpiece, and vision system model. As a result, the outer loop focuses on controlling the contacting force and overcoming the existing uncertainties associated with contacting force model parameters such as stiffness coefficient. Thus, the problem of local-minima due to the conflict between controlling the force and vision of traditional hybrid control schemes can be solved.

In the inner loop, IBVS is exploited to track the desired image features path in the image space corresponding to the desired path on the workpiece surface. Additionally, a novel method based on the spline fitting [55] and modified images features in [46] is developed to transform the desired path on the workpiece in the Cartesian space to the desired image feature paths in the image space. Hence, an invertible interaction matrix can be obtained for an advanced visual servoing controller while the global stability of the system is guaranteed.

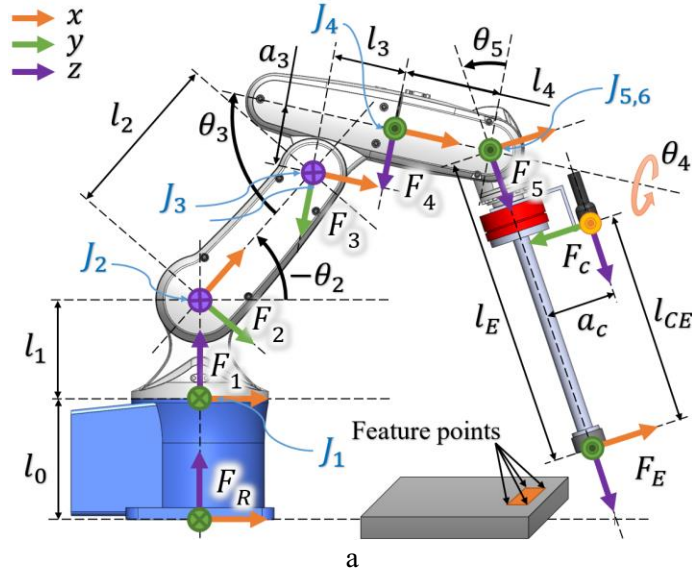
In the outer force feedback loop, the force compensator's output is the desired modified image features velocity corresponding to the camera velocity in the normal direction to the workpiece's

surface. This output is combined with the extracted desired features from the desired path on the workpiece's surface to generate the ultimate desired image features. Tracking these image features by the IBVS results in controlling the force as well.

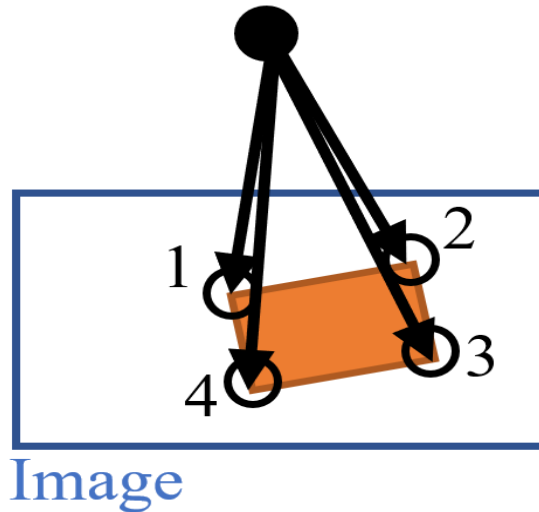
A continuous integral sliding mode control (CISMC) method is developed for vision and force compensators, which aim at removing the reaching phase by adopting an integral sliding surface and handling the existing uncertainties. In this chapter, the designed CISMC is an extension of the conventional ISMC which uses a fast terminal controller (FTC), as the nominal controller, and modified super-twisting algorithm (MSTA) for perturbation rejection [56], [57]. This combination can improve control performance in terms of robustness against uncertainties, fast convergence, precise tracking, and low-level of chattering. A contact detection algorithm (CDA) is also developed to manage the switching between the pure IBVS task when the robot is not in contact with the workpiece, i.e., free-motion, and vision and force control task when the robot is interacting with the workpiece. The finite-time stability of the cascade vision and force controller is proved, and experimental tests are carried out to validate its effectiveness.

2.2 System Modeling

In this section, the problem of hybrid vision and force control of an industrial robot interacting with a workpiece is investigated. Referring to Figure 2.1a, a 6-DOF serial robot equipped with a force sensor and an EIH camera is considered. Also, a rectangular object is placed on the workpiece whose corners are considered as four feature points (Figure 2.1b).



Feature points



Image

b

Figure 2.1: a) The 6-DOF robot equipped with a force sensor and an EIH camera, b) Feature points.

2.2.1 Visual Servoing Modeling

To design an IBVS controller with an EIH camera, the kinematic relationship between the image features $S = [s_1^T, \dots, s_4^T]^T$ and the camera frame $\{F_c\}$ should be derived. Generally, the image features are the projections of the feature points on the image plane which are derived using the perspective projection technique [3] as follows:

$$s_i = [x_{c_i} \quad y_{c_i}]^T = \frac{f}{z_{c_i}} [X_{c_i} \quad Y_{c_i}]^T, i = 1:4, \quad (2.1)$$

where, f is the focal length and $P_{c_i} = [X_{c_i} \quad Y_{c_i} \quad Z_{c_i}]^T$ describes the coordinates of the i^{th} feature point with respect to the camera frame. The relation between the time derivative of the i^{th} image feature \dot{s}_i on the image plane and the velocity screw of the camera V is denoted as [24]:

$$\dot{s}_i = \mathbf{L}_{s_i} V, \quad (2.2)$$

where \mathbf{L}_{s_i} describes the interaction matrix:

$$\mathbf{L}_{s_i} = \begin{bmatrix} -\frac{f}{z_{c_i}} & 0 & \frac{x_{c_i}}{z_{c_i}} & \frac{x_{c_i}y_{c_i}}{f} & -\frac{1+x_{c_i}^2}{f} & y_{c_i} \\ 0 & -\frac{f}{z_{c_i}} & \frac{y_{c_i}}{z_{c_i}} & \frac{1+y_{c_i}^2}{f} & -\frac{x_{c_i}y_{c_i}}{f} & x_{c_i} \end{bmatrix}. \quad (2.3)$$

Accordingly, from (2.2) and (2.3) the following relation yields:

$$\dot{S} = \mathbf{L}_S V, \quad (2.4)$$

where S is the image feature velocity vector and

$$\mathbf{L}_S = [\mathbf{L}_{s_1}^T \quad \mathbf{L}_{s_2}^T \quad \mathbf{L}_{s_3}^T \quad \mathbf{L}_{s_4}^T]^T. \quad (2.5)$$

During the interaction, the tool tip is in contact with the surface in the normal direction. Therefore, referring to Figure 2.1a, the distance between the camera frame and the feature points in the normal direction, i.e., Z_{c_i} , is approximately considered as l_{cE} . The IBVS controller aims at reducing the norm of image feature errors. In this case, although the system is locally stable, the global stability cannot be guaranteed [24]-[26]. Hence, advanced IBVS control strategies are needed to guarantee the convergence and stability. To cope with this problem, a vector of modified image features \bar{S} [46] is adopted as:

$$\bar{S} = [\bar{x}_c \quad \bar{y}_c \quad \bar{D}_c \quad \bar{\theta}_{cx} \quad \bar{\theta}_{cy} \quad \bar{\theta}_{cz}]^T, \quad (2.6)$$

where:

$$\begin{aligned}
\bar{x}_c &= \frac{\sum_{i=1}^4 x_{c_i}}{4}, \bar{y}_c = \frac{\sum_{i=1}^4 y_{c_i}}{4}, \\
\bar{D}_c &= \sum_{i=1}^3 \sqrt{(x_{c_{i+1}} - x_{c_i})^2 + (y_{c_{i+1}} - y_{c_i})^2} + \sqrt{(x_{c_1} - x_{c_4})^2 + (y_{c_1} - y_{c_4})^2} \\
\bar{\theta}_x &= \frac{1}{2} \left(\text{atan} \left(\frac{x_{c_2} - x_{c_1}}{y_{c_1} - y_{c_2}} \right) - \text{atan} \left(\frac{x_{c_3} - x_{c_4}}{y_{c_4} - y_{c_3}} \right) \right) \\
\bar{\theta}_y &= \frac{1}{2} \left(\text{atan} \left(\frac{y_{c_3} - y_{c_2}}{x_{c_3} - x_{c_2}} \right) - \text{atan} \left(\frac{y_{c_4} - y_{c_1}}{x_{c_4} - x_{c_1}} \right) \right) \\
\bar{\theta}_z &= \frac{1}{2} \left(\text{atan} \left(\frac{y_{c_1} - y_{c_4}}{x_{c_4} - x_{c_1}} \right) + \text{atan} \left(\frac{y_{c_2} - y_{c_3}}{x_{c_3} - x_{c_2}} \right) \right).
\end{aligned} \tag{2.7}$$

Accordingly, the kinematic relation between the camera and the modified image features velocities is:

$$\dot{\bar{S}} = \bar{\mathbf{L}}_s V, \tag{2.8}$$

where $\bar{\mathbf{L}}_s$ is the modified interaction matrix [46]. Since $\bar{\mathbf{L}}_s$ is a 6×6 matrix with full rank, it would be invertible. Consequently, designing advanced IBVS strategies will be feasible by employing this modified interaction matrix. The camera velocity is mapped to the joint space using the following relation:

$$V = \mathbf{J}_q \dot{q}, \tag{2.9}$$

where $\mathbf{J}_q \in \mathbb{R}^{6 \times 6}$ and $\dot{q} \in \mathbb{R}^{6 \times 1}$ are the robot Jacobian matrix and the vector of joint velocities, respectively. Substituting (2.9) into (2.8), one has

$$\dot{\bar{S}} = \bar{\mathbf{L}}_s \mathbf{J}_q \dot{q}. \tag{2.10}$$

In the real applications, the uncertainties exist in the interaction matrix and robotic Jacobian matrix, i.e., $\bar{\mathbf{L}}_s \mathbf{J}_q = \hat{\bar{\mathbf{L}}}_s \hat{\mathbf{J}}_q + \Delta_s$. Accordingly, the equation is rewritten as:

$$\dot{\bar{S}} = \hat{\bar{\mathbf{L}}}_s \hat{\mathbf{J}}_q \dot{q} + \bar{\Delta}_s, \tag{2.11}$$

where, $\bar{\Delta}_s = \Delta_s \dot{q}$ is the uncertain part of the vision model.

2.2.2 Force Modeling

To design a hybrid vision and force controller, the model of contact interaction between the tool and the workpieces should be derived. To this end, the stiffness model is exploited [6]. Accordingly, the mathematical formulation of the contact force when the tool-tip touches the workpiece surface is modeled as:

$$F_z = K_f P_f, \quad (2.12)$$

where K_f is the nominal stiffness between the workpiece surface and tool-tip, P_f is the displacement of the tool tip in its normal direction, i.e., z-axis of the end-effector or camera frame, and F_z is the exerted normal force to the tool tip. In the cases where the tool tip is normal to the surface, F_z would be normal to that surface as well. Taking time derivative of (2.12) yields:

$$\dot{F}_z = K_f D V_n, \quad (2.13)$$

where $D = [0 \ 0 \ 1 \ 0 \ 0 \ 0]$ and $D V_n = \dot{P}_f$. $V_n = \mathbf{Q}V$ is the linear velocity of the end-effector in the z-direction of its frame where $\mathbf{Q} = \text{diag}(D)$. Using (2.8), (2.13) is written as:

$$\dot{F}_z = K_f D \bar{\mathbf{L}}_s^{-1} \dot{\hat{S}}. \quad (2.14)$$

Considering the uncertainties in the kinematic relations and stiffness coefficient, i.e., $K_f D \bar{\mathbf{L}}_s^{-1} = \hat{K}_f D \hat{\mathbf{L}}_s^{-1} + \Delta_F$, we have:

$$\dot{F}_z = \hat{K}_f D \hat{\mathbf{L}}_s^{-1} \dot{\hat{S}} + \bar{\Delta}_F, \quad (2.15)$$

where, $\bar{\Delta}_F = \Delta_F \dot{\hat{S}}$ is the uncertain part of the force model, and notation $\hat{\cdot}$ denotes the nominal part.

2.3 Robust Cascade Vision and Force Control Method

In this section, the design of the cascade EIH vision and force controller using CISM is presented. IBVS in the proposed hybrid controller is designed to track the desired image features. Therefore, it is required to extract the desired image feature paths on the image plane corresponding to the desired path on the workpiece. For this purpose, an image feature extraction method is developed and presented in the following subsection.

2.3.1 Desired Image Feature Extraction

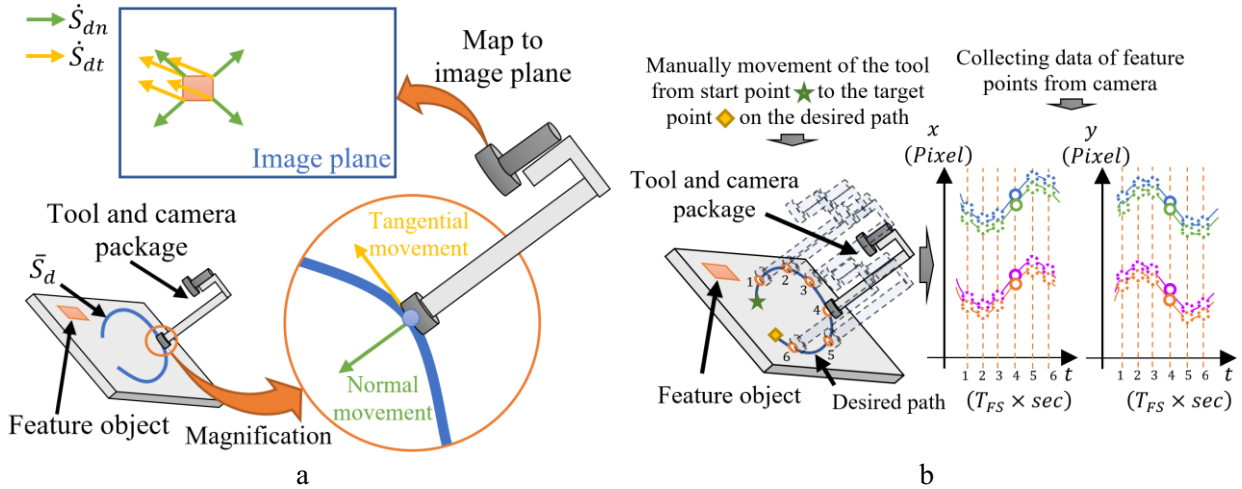


Figure 2.2: a) Decomposition of \bar{S}_d , b) Collecting image features data while moving on the desired path.

The robot manipulator tracks the desired path while the normal force on the workpiece's surface is controlled. Therefore, the desired vector of image features comprises two orthogonal vectors as follows:

$$\bar{S}_d = \bar{S}_{dt} + \bar{S}_{dn}, \quad (2.16)$$

where, \bar{S}_d is the desired vector of image features, \bar{S}_{dn} is the normal desired vector of image features corresponding to the movement of the end-effector or camera in the direction of z-axis of the camera frame. The value of \bar{S}_{dn} is determined by the force compensator, the procedure of which

will be explained in the controller design subsection. \bar{S}_{dt} is the tangential desired vector of image features which is associated with the tangential movement of the end-effector on the surface of the workpiece, i.e., the desired path on the workpiece in Cartesian space (Figure 2.2a). To extract \bar{S}_{dt} , a novel technique based on experimental data and spline is suggested. First, the robot's end-effector is guided to the desired path on the workpiece manually. While the end-effector is moving on the desired path, the image features coordinates captured by the camera are collected with a specific sampling time T_{FS} (Figure 2.2b). Then, a spline is fitted to each series of feature points and eight desired image feature paths are generated. $S_{dt} \in \mathbb{R}^{8 \times 1}$, is obtained as

$$S_{dt} = [\text{SPL}(\hat{s}_{dt_1}, t) \quad \cdots \quad \text{SPL}(\hat{s}_{dt_8}, t)]^T, \quad (2.17)$$

where $\hat{S}_{dt} = [\hat{s}_{dt_1}^T \quad \cdots \quad \hat{s}_{dt_8}^T]^T \in \mathbb{R}^{8 \times n_l}$ is the matrix that contains eight series of collected imaged features, i.e., $\hat{s}_{dt_i}, i \in \{1, \dots, 8\}$, with the length n_l . $\text{SPL}(\cdot, \cdot)$ [59] is the spline function that takes the collected data and instant time t , then fits a spline function to those data and finally returns the value of the fitted curve at the time t . The extracted S_{dt} should be converted to the modified \bar{S}_{dt} using (2.6) and (2.7) for the proposed hybrid controller.

2.3.2 Cascade Vision and Force Controller Design Using CISM

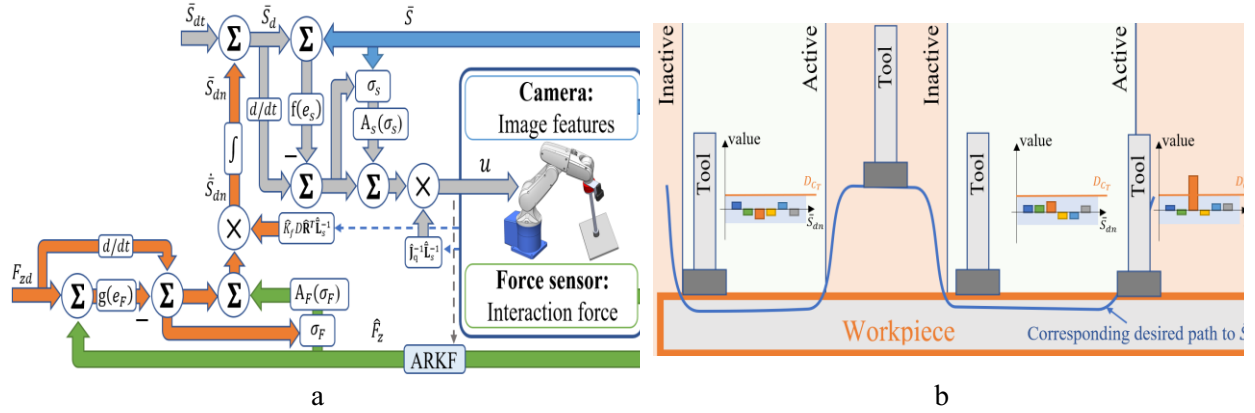


Figure 2.3: a) Schematic of the proposed robust cascade vision and force controller, b) Detection of contact with the workpiece and automatic activation and deactivation of the force controller.

In this subsection, a robust cascade control scheme based on CISM is designed to achieve a robust and high precision vision and force tracking performance. CISM is the generalization of the traditional ISMC whose discontinuous part is replaced with MSTA to achieve a continuous output and hence, to reduce the chattering [56], [57]. Additionally, its nominal part is chosen to be an FTC, which results in high tracking accuracy and fast finite-time convergence.

The proposed cascade scheme uses inner and outer feedback loops of image features and the force signal to perform the control task. The inner loop feeds the vision compensator with \bar{s} . The vision compensator compares \bar{s} with the desired signal, i.e., \bar{s}_d , and computes the control command accordingly. The outer loop feeds the force compensator with the normal force signal. The force compensator compares it with the desired force signal F_{zd} and generates the output. Note that the force compensator's output is the velocity of the desired image features in the normal direction, i.e., $\dot{\bar{s}}_{dn}$. Since \bar{s}_{dn} and \bar{s}_{dt} are orthogonal to each other, they satisfy (2.16) and (2.18) [17]:

$$\bar{s}_{dt} = \left(\mathbf{I} - \frac{\bar{s}_{dn}^T \bar{s}_{dn}}{\|\bar{s}_{dn}\|^2} \right) \bar{s}_d. \quad (2.18)$$

Accordingly, if $\bar{S} \rightarrow \bar{S}_d$ then $\bar{S}_t \rightarrow \bar{S}_{dt}$, which is equivalent to tracking the desired path on the workpiece's surface, and $\bar{S}_n \rightarrow \bar{S}_{dn}$, which results in controlling the interaction force. Thus, the control problem is to derive a hybrid control law, i.e., $u = \dot{q}$ that leads to $e_s \rightarrow 0$ and $e_F \rightarrow 0$, where:

$$e_s = \bar{S} - \bar{S}_d, e_F = F_Z - F_{zd}. \quad (2.19)$$

In (2.19), e_s and e_F are the vision and force system errors. Taking the time derivative of (2.19) and substituting (2.11) and (2.15) in it yields:

$$\dot{e}_s = \hat{\mathbf{L}}_s \hat{\mathbf{J}}_q u + \bar{\Delta}_s - \dot{\bar{S}}_d, \dot{e}_F = \hat{K}_f D \hat{\mathbf{L}}_s^{-1} \dot{\bar{S}} + \bar{\Delta}_F - \dot{F}_{zd}. \quad (2.20)$$

Generally, ISMC divides the controller commands into two parts which are the nominal controller command and the uncertainty eliminator [57]. Accordingly, the IBVS control law for controlling the images features is suggested as:

$$u = u_0 + u_1, u_0 = \hat{\mathbf{J}}_q^{-1} \hat{\mathbf{L}}_s^{-1} \left(-f(e_s) + \dot{\bar{S}}_d \right), u_1 = \hat{\mathbf{J}}_q^{-1} \hat{\mathbf{L}}_s^{-1} A_s(\sigma_s), \quad (2.21)$$

where u_0 and u_1 are the nominal and uncertainty eliminator control commands, $f(\cdot)$ is the fast terminal law function, σ_s is the integral sliding mode variable for IBVS, and $A_s(\cdot)$ is the MSTA law for IBVS, all of which are given as follows:

$$f(e_s) = \mathbf{C}_1 e_s + \mathbf{C}_2 \text{sig}^\alpha(e_s), \quad (2.22)$$

$$A_s(\sigma_s) = -\mathbf{K}_1 \sigma_s - \mathbf{K}_2 \text{sig}^{\frac{1}{2}}(\sigma_s) + \int_{t_0}^t (-\mathbf{K}_3 \sigma_s - \mathbf{K}_4 \text{sign}(\sigma_s)) dt, \quad (2.23)$$

$$\sigma_s = \bar{S} - \bar{S}_0 - \int_{t_0}^t (\hat{\mathbf{L}}_s \hat{\mathbf{J}}_q u_0) dt. \quad (2.24)$$

where \mathbf{C}_1 and \mathbf{C}_2 are positive diagonal matrices of controller gains, $0 < \alpha < 1$, and $\text{sig}^*(\cdot) = |\cdot|^* \text{sign}(\cdot)$. \mathbf{K}_1 to \mathbf{K}_4 are positive diagonal matrices of MSTA's gains.

As mentioned before, the force compensator output is $v = \dot{S}_{dn}$. The suggested control law of (2.21) results in controlling the images features in finite-time, hence one has $\dot{S}_{dn} = \dot{S}_n$. Given this fact and based on (2.20), the output of the interaction force compensator v using CISM is obtained as:

$$v = v_0 + v_1, v_0 = \hat{K}_f^{-1} \hat{\mathbf{L}}_s D^+ (-g(e_F) + \dot{F}_{zd}), v_1 = \hat{K}_f^{-1} \hat{\mathbf{L}}_s D^+ A_f(\sigma_f), \quad (2.25)$$

where v_0 and v_1 are the nominal and uncertainty eliminator control commands, $g(\cdot)$ is the fast terminal law function, σ_f is the integral sliding mode variable for interaction force system, and $A_f(\cdot)$ is the MSTA law for interaction force system, all of which are presented as the following relations:

$$g(e_F) = D_1 e_F + D_2 \text{sig}^\beta(e_F), \quad (2.26)$$

$$A_f(\sigma_f) = -L_1 \sigma_f - L_2 \text{sig}^{\frac{1}{2}}(\sigma_f) + \int_{t_0}^t (-L_3 \sigma_f - L_4 \text{sign}(\sigma_f)) dt, \quad (2.27)$$

$$\sigma_f = F - F_0 - \int_{t_0}^t \left(\hat{K}_f D \hat{\mathbf{L}}_s^{-1} (-f(e_s) + \dot{S}_{dt} + v_0) \right) dt, \quad (2.28)$$

where D_1 and D_2 are positive diagonal matrices of controller gains, L_1 to L_4 are positive diagonal matrices of MSTA's gains.

Substituting (2.25) into (2.21), the overall cascade vision and force control law is obtained as:

$$u = \hat{\mathbf{J}}_q^{-1} \hat{\mathbf{L}}_s^{-1} \left(-f(e_s) + \dot{S}_{dt} + \hat{K}_f^{-1} \hat{\mathbf{L}}_s D^+ \left(-g(e_F) + \dot{F}_{zd} + A_f(\sigma_f) \right) + A_s(\sigma_s) \right). \quad (2.29)$$

2.3.3 Contacting Detection and Managing the Robot's Task

The vision and force control occurs when the robot interacts with the workpiece. Otherwise, it has a free motion in the workspace, i.e., pure visual servoing. Accordingly, for each task, a proper controller must be applied. This can be done by modifying the overall control law of (2.29) as follows:

$$u = \hat{J}_q^{-1} \hat{\mathbf{L}}_s^{-1} \left(-f(e_s) + \dot{\bar{S}}_{dt} + \delta_M(\hat{F}_z) \hat{K}_f^{-1} \hat{\mathbf{L}}_s D^+ \left(-g(e_F) + \dot{F}_{zd} + A_F(\sigma_F) \right) + A_s(\sigma_s) \right), \quad (2.30)$$

where $\delta_M(\cdot)$ is a switching function which returns 1 or 0 when its input \hat{F}_z is greater than zero or equal to zero, respectively. Theoretically, when the tool tip touches the surface, one has $\hat{F}_z > 0$, $\delta_M(\hat{F}_z) = 1$ and the vision and force control law will be activated. However, when there is no contact, one has $\hat{F}_z = 0$, $\delta_M(\hat{F}_z) = 0$ and the pure vision control law will be applied to the robot (Figure 2.3a). In this case, e_F is set to zero.

In practice, however, during the free motion operation, the force signal is not absolutely zero due to the existing noises and low resolution. To cope with this problem, a feasible contact detection algorithm (CDA) is developed to sense the contact and manage between the tasks. CDA detects the contact by taking the force signal feedback as the input. Its procedure is presented in Algorithm 1. The algorithm inputs are \hat{F}_z , FCA_p , and \bar{S}_{dn} , where FCA_p is the force activation indicator of the previous time instant. The output of the algorithm is FCA , i.e., the force activation indicator. The algorithm supervises the contact as follows: a) while the force compensator is inactive i.e., $FCA_p = \delta_M(\hat{F}_z) = 0$, increasing the magnitude of \hat{F}_z beyond F_{TH} leads to $FCA = \delta_M(\hat{F}_z) = 1$; b) For the values of \hat{F}_z below F_{TL} , or the values of \bar{S}_{dn_3} beyond D_{CT} , $FCA = 0$. \bar{S}_{dn_3} is the third entry of \bar{S}_{dn} and D_{CT} is the threshold of detachment. Note that \bar{S}_{dn_3} indicates the displacement change in the normal direction to the workpiece's surface. When it is positive, it means that the force compensator intends to move the tool tip towards the surface. However, when its value increases and passes the threshold, it means the tool tip tends to detach from the surface, while the force compensator tries to keep the tool tip on the surface and control the normal force. Thus, \bar{S}_{dn_3} will increase (Figure 2.3b).

Algorithm 1. Contact detection algorithm.

```

Initialize  $F_{T_H}, F_{T_L}, D_{C_T}$ ;
Input:  $\hat{F}_z, \bar{S}_{dn}$ ;
 $FCA = FCA_p$ ;
If ( $FCA_p == 0 \ \&\& \ \hat{F}_z > F_{T_H}$ ) Then  $FCA = 1$ ;
If ( $\hat{F}_z < F_{T_L} \ \parallel \ \bar{S}_{dn_3} > D_{C_T}$ ) Then  $FCA = 0$ ;
Return  $FCA$ ;

```

Remark 2.1. In the proposed method, the force compensation will be activated automatically once the contact is detected. Therefore, to activate the force compensator, the desired path in the Cartesian space corresponding to \bar{S}_{dt} should be defined beneath the surface of the workpiece. Thus, the tool tip touches the surface while tracking \bar{S}_{dt} . Then, CDA detects the contact and the force compensator will be activated. To deactivate the force compensator, the reverse process must be adopted and the desired path must be defined out of the workpiece (Figure 2.3b).

2.3.4 Stability Analysis

In this subsection, the stability of the proposed hybrid vision and force controller is analyzed. In Theorem 2.1, the finite-time convergence of the overall cascade vision and force controller considering existing uncertainties is proved. The following assumptions are employed in Theorem 2.1.

Assumption 2.1. The time derivatives of $\bar{\Delta}_s$ and $\bar{\Delta}_F$ are bounded as in (2.31). Also Γ_1 and Γ_2 are bounded as in (2.32).

$$\dot{\bar{\Delta}}_s \leq \delta_s \mid \delta_s \in \mathbb{R}^{6 \times 1}, \delta_s > 0, \dot{\bar{\Delta}}_F \leq \delta_F \mid \delta_F \in \mathbb{R}, \delta_F > 0, \quad (2.31)$$

$$\Gamma_1 \leq \delta_{L1} \mid \delta_{L1} \in \mathbb{R}^{6 \times 6}, \Gamma_2 \leq \delta_{L2} \mid \delta_{L2} \in \mathbb{R}^{6 \times 6}, \quad (2.32)$$

where Γ_1 and Γ_2 are:

$$\begin{aligned}\Gamma_1 &= \frac{\delta_M(\hat{F}_Z)\bar{K}_f^2}{4D_1} \left(D \frac{d(\hat{\mathbf{L}}_s^{-1})}{dt} \mathbf{C}_1 \right)^T D \hat{\mathbf{L}}_s^{-1}, \\ \Gamma_2 &= \frac{\delta_M(\hat{F}_Z)\bar{K}_f^2}{4D_1} \frac{2}{\alpha+1} \left(D \frac{d(\hat{\mathbf{L}}_s^{-1})}{dt} \mathbf{C}_2 \right)^T D \hat{\mathbf{L}}_s^{-1}.\end{aligned}\quad (2.33)$$

Assumption 2.2. $\gamma \in \mathbb{R}^+$ must be chosen large enough, so that the following condition is satisfied:

$$\min\{\{\bar{\lambda}_{\min}\{(\gamma\mathbf{C}_1 - \delta_{L1}) + (\gamma\mathbf{C}_1 - \delta_{L1})^T\}, \bar{\lambda}_{\min}(\gamma\mathbf{C}_2 - \delta_{L2}) + (\gamma\mathbf{C}_2 - \delta_{L2})^T\} > 0, \quad (2.34)$$

where $\lambda_{\min}\{\star\}$ returns the minimum value of the set of eigenvalues of \star .

Assumption 2.3. The MSTAs' coefficients satisfy the following inequalities:

$$\begin{aligned}[\mathbf{K}_3]_{i,i} &> \left(\frac{[\mathbf{K}_2]_{i,i}^3 [\mathbf{K}_2]_{i,i}^2 + \frac{5}{2} [\mathbf{K}_2]_{i,i}^2 p_i}{p_{s_i} - \frac{1}{2} [\mathbf{K}_2]_{i,i}^3} - \frac{1}{2} [\mathbf{K}_1]_{i,i}^2 \right), [\mathbf{K}_3]_{i,i} > [\mathbf{K}_1]_{i,i}, \\ p_{s_i} &= [\mathbf{K}_2]_{i,i}^2 \left(\frac{1}{4} [\mathbf{K}_2]_{i,i}^2 - [\delta_s]_i + [\mathbf{K}_4]_{i,i} + \frac{1}{4} [\mathbf{K}_2]_{i,i}^2 \right), \\ [\mathbf{K}_2]_{i,i} &> 2\sqrt{[\delta_s]_i}, [\mathbf{K}_1]_{i,i} > 0, [\mathbf{K}_4]_{i,i} > [\delta_s]_i, i \in \{1, \dots, n\},\end{aligned}\quad (2.35)$$

$$\begin{aligned}L_3 &> \left(\frac{L_2^3 L_2^2 + \frac{5}{2} L_2^2 p_i}{p_{f_i} - \frac{1}{2} L_2^3} - \frac{1}{2} L_1^2 \right), L_3 > L_1, L_4 > \delta_F, \\ p_{f_i} &= L_2^2 \left(\frac{1}{4} L_2^2 - \delta_F + L_4 + \frac{1}{4} L_2^2 \right), L_2 > 2\sqrt{\delta_F}, L_1 > 0.\end{aligned}\quad (2.36)$$

Theorem 2.1. Consider a robot with an EIH camera interacting with a workpiece (Figure 2.1a).

Applying hybrid control law (2.30) to the robot with uncertain vision and force systems as given in (2.11) and (2.15) leads to their stabilities in finite-time, i.e., $e_s = 0$ and $e_F = 0$, when $t > T_c$, where $T_c \in \mathbb{R}^+$.

Proof. Taking time derivative of (2.24) and substituting (2.11) and the hybrid control law of (2.30) into it, one has:

$$\dot{\sigma}_s = A_s(\sigma_s) + \bar{\Delta}_s. \quad (2.37)$$

By substituting (2.23) into (2.37), the following system is obtained:

$$\begin{cases} \dot{\sigma}_s = -\mathbf{K}_1 \sigma_s - \mathbf{K}_2 \text{sig}^{1/2}(\sigma_s) + \zeta_s \\ \dot{\zeta}_s = -\mathbf{K}_3 \sigma_s - \mathbf{K}_4 \text{sign}(\sigma_s) + \dot{\bar{\Delta}}_s \end{cases}. \quad (2.38)$$

Considering (2.31) and (2.35), and applying Lemma 2.1 to (2.37), σ_s and $\dot{\sigma}_s$ converge to zero in finite time. Accordingly, performing the same procedure for $\dot{\sigma}_F$ yields:

$$A_s(\sigma_s) + \bar{\Delta}_s = 0, A_F(\sigma_F) + \bar{\Delta}_F = 0. \quad (2.39)$$

Consider the candidate Lyapunov function V_1 as:

$$V_1 = V_s + V_F + V_a, \quad (2.40)$$

where:

$$\begin{aligned} V_s &= (1/2)\gamma e_s^T e_s, & V_F &= (1/2)e_F^2, \\ V_a &= \frac{\delta_M(\hat{F}_z)\hat{K}_f^2}{8D_1} \left(D\hat{\mathbf{L}}_s^{-1}\mathbf{C}_1 e_s \right)^T \left(D\hat{\mathbf{L}}_s^{-1} e_s \right) + \\ &\frac{\delta_M(\hat{F}_z)\hat{K}_f^2}{8D_1} \frac{2}{\alpha+1} \left(D\hat{\mathbf{L}}_s^{-1}\mathbf{C}_2 \text{sig}^{\frac{(\alpha+1)}{2}}(e_s) \right)^T \left(D\hat{\mathbf{L}}_s^{-1} \text{sig}^{\frac{(\alpha+1)}{2}}(e_s) \right). \end{aligned} \quad (2.41)$$

When $e_s = 0$ and $e_F = 0$, one has $V_1 = 0$. Otherwise, $V_1 > 0$. From (2.40), \dot{V}_1 is derived as:

$$\dot{V}_1 = \dot{V}_s + \dot{V}_F + \dot{V}_a, \quad (2.42)$$

where:

$$\begin{aligned} \dot{V}_s &= \gamma e_s^T \dot{e}_s, \dot{V}_F = e_F \dot{e}_F, \dot{V}_a = \frac{\delta_M(\hat{F}_z)\hat{K}_f^2}{4D_1} \left(e_s^T \left(D \frac{d(\hat{\mathbf{L}}_s^{-1})}{dt} \mathbf{C}_1 \right)^T D\hat{\mathbf{L}}_s^{-1} e_s \right) + \\ &\frac{\delta_M(\hat{F}_z)\hat{K}_f^2}{4D_1} \frac{2}{\alpha+1} \left(\left(\text{sig}^{\frac{(\alpha+1)}{2}}(e_s) \right)^T \left(D \frac{d(\hat{\mathbf{L}}_s^{-1})}{dt} \mathbf{C}_2 \right)^T D\hat{\mathbf{L}}_s^{-1} \text{sig}^{\frac{(\alpha+1)}{2}}(e_s) \right) + \frac{\delta_M(\hat{F}_z)\hat{K}_f^2}{4D_1} (\mathbf{C}_1 e_s + \\ &\mathbf{C}_2 \text{sig}^\alpha(e_s))^T (D\hat{\mathbf{L}}_s^{-1})^T D\hat{\mathbf{L}}_s^{-1} \dot{e}_s. \end{aligned} \quad (2.43)$$

Substituting the control laws (2.30) and (2.39) into (2.20) yields:

$$\begin{aligned} \dot{e}_s &= \hat{\mathbf{L}}_s \hat{\mathbf{J}}_q \left(\hat{\mathbf{J}}_q^{-1} \hat{\mathbf{L}}_s^{-1} \left(-f(e_s) + \dot{S}_{dt} + \delta_M(\hat{F}_z)\hat{K}_f D\hat{\mathbf{L}}_s^{-1} \left(-g(e_F) + \dot{F}_{zd} + A_s(\sigma_f) \right) + \right. \right. \\ &\left. \left. A_s(\sigma_s) \right) \right) + \bar{\Delta}_s - \dot{S}_d = -\mathbf{C}_1 e_s - \mathbf{C}_2 \text{sig}^\alpha(e_s). \end{aligned} \quad (2.44)$$

Since $\dot{S}_{dt} = \hat{\mathbf{L}}_s(I - D^T D)\hat{\mathbf{L}}_s^{-1}\dot{S}_d$, by substituting the hybrid control law of (2.30) into (2.11) and then the result into (2.20), the following relation is obtained:

$$\dot{e}_F = -\delta_M(\hat{F}_z) \left(D_1 e_F + D_2 \text{sig}^\beta(e_F) - \dot{F}_{zd} - A_F(\sigma_F) \right) + \hat{K}_f D \hat{\mathbf{L}}_s^{-1} (-f(e_s) + A_s(\sigma_s) + \bar{\Delta}_s) + \bar{\Delta}_F - \dot{F}_{zd}. \quad (2.45)$$

By substituting (2.44) and (2.45) into (2.43), one has:

$$\dot{V}_s = \gamma e_s^T (-\mathbf{C}_1 e_s - \mathbf{C}_2 \text{sig}^\alpha(e_s)) \quad (2.46)$$

$$\dot{V}_F = e_F \left(-\delta_M(\hat{F}_z) \left(D_1 e_F + D_2 \text{sig}^\beta(e_F) - \dot{F}_{zd} - A_F(\sigma_F) \right) + \hat{K}_f D \hat{\mathbf{L}}_s^{-1} (-f(e_s) + A_s(\sigma_s) + \bar{\Delta}_s) + \bar{\Delta}_F - \dot{F}_{zd} \right) \quad (2.47)$$

$$\dot{V}_a = e_s^T \Gamma_1 e_s + \left(\text{sig}^{\frac{(\alpha+1)}{2}}(e_s) \right)^T \Gamma_2 \text{sig}^{\frac{(\alpha+1)}{2}}(e_s) - \frac{\delta_M(\hat{F}_z) \hat{K}_f^2}{4D_1} (\mathbf{C}_1 e_s + \mathbf{C}_2 \text{sig}^\alpha(e_s))^T (D \hat{\mathbf{L}}_s^{-1})^T D \hat{\mathbf{L}}_s^{-1} (\mathbf{C}_1 e_s + \mathbf{C}_2 \text{sig}^\alpha(e_s)), \quad (2.48)$$

If $\delta_M(\hat{F}_z) = 0$ then $e_F = 0$ and substituting (2.39) into (2.46) to (2.48) results in the following relation:

$$\dot{V}_1 = -\gamma e_s^T (\mathbf{C}_1 e_s + \mathbf{C}_2 \text{sig}^\alpha(e_s)) \leq 0, \quad (2.49)$$

and if $\delta_M(\hat{F}_z) = 1$, one has:

$$\dot{V}_1 = -e_s^T (\gamma \mathbf{C}_1 - \mathbf{\Gamma}_1) e_s - e_s^T (\gamma \mathbf{C}_2 - \mathbf{\Gamma}_2) \text{sig}^\alpha(e_s) - D_2 |e_F|^{\beta+1} - \left(D_1^{\frac{1}{2}} e_F + \frac{\hat{K}_f D \hat{\mathbf{L}}_s^{-1}}{2D_2^{\frac{1}{2}}} (\mathbf{C}_1 e_s + \mathbf{C}_2 \text{sig}^\alpha(e_s)) \right)^2. \quad (2.50)$$

Given (2.32) and Assumption 2.2, based on non-symmetrical positive definite matrix definition in [29], $(\gamma \mathbf{C}_1 - \mathbf{\Gamma}_1)$ and $(\gamma \mathbf{C}_2 - \mathbf{\Gamma}_2)$ are positive definite. Hence, $\dot{V}_1 \leq 0$ and therefore, systems (2.11) and (2.15) are stable. According to (2.41), one has $e_s^T e_s = 2V_s$. Thus, the following conditions are satisfied.

$$-e_s^T \mathbf{C}_1 e_s \leq -c_{1m} (2V_s), \quad -e_s^T \mathbf{C}_2 \text{sig}^\alpha(e_s) \leq -c_{2m} (2V_s)^{\alpha/2} \quad (2.51)$$

$$, c_{im} = \min_{k \in \{1,2,\dots,6\}} [\mathbf{C}_i]_{k,k}.$$

Comparing (2.51) with (2.46), the following inequality is obtained.

$$\dot{V}_s \leq -c_{1m} 2V_s - c_{2m} (2V_s)^{\alpha/2}. \quad (2.52)$$

Considering $\alpha_T = \frac{\alpha}{2}$ and $C_T = -2^{\alpha_T} c_{2m}$, the inequality above results in $\dot{V}_s \leq -C_T V_s^{\alpha_T}$. Since $C_T > 0$ and $0 < \alpha_T < 1$, based on finite-time theory in [59], V_s converges to zero in finite time $T_s \leq \frac{V_s^{1-\alpha_T}}{c_{2m}(1-\alpha_T)}$. Hence, after T_s , one has $e_s = 0$. Accordingly, after T_s , if $\delta_M(\hat{F}_z) = 0$, then $e_F = 0$.

However, if $\delta_M(\hat{F}_z) = 1$, substituting (2.39) into (2.47) yields:

$$\dot{V}_F = -e_F (D_1 e_F + D_2 \text{sig}^\beta(e_F)). \quad (2.53)$$

Equation (2.53) is equivalent to (2.46). Hence, V_F converges to zero in finite time $T_C = T_s + T_F$,

where $T_F \leq \frac{V_F^{1-\beta_T}}{D_2(1-\beta_T)}$ and $\beta_T = \frac{\beta}{2}$. Consequently, after T_C , one has $e_s = 0$ and $e_F = 0$.

Remark 2.2. The closed-loop systems (2.44) and (2.45) include two feedback control terms. The first term is linear and results in converging the system states to zero with a moderate rate. The second term is a nonlinear S-shaped function which results in finite-time convergence and increasing the tracking precision when the error of the system is small.

Lemma 2.1 (MSTA). The perturbed system given in (2.54) is stable as 2-SM if the inequalities in (2.55) are satisfied.

$$\begin{cases} \dot{\sigma} = -k_1 \sigma - k_2 \text{sig}^{1/2}(\sigma) + \zeta \\ \dot{\zeta} = -k_3 \sigma_s - k_4 \text{sign}(\sigma) + \dot{\Delta} \end{cases}, \quad (2.54)$$

$$\begin{aligned} & |\dot{\Delta}| < \delta \in \mathbb{R}^+, k_2 > 2\sqrt{\delta}, k_1 > 0, k_4 > \delta, k_3 > k_1, \\ & k_3 > \left(\frac{k_2^3 k_2^2 + \frac{5}{2} k_2^2 p_i}{p - \frac{1}{2} k_2^3} - \frac{1}{2} k_1^2 \right), p = k_2^2 \left(\frac{1}{4} k_2^2 - \delta + k_4 + \frac{1}{4} k_2^2 \right). \end{aligned} \quad (2.55)$$

Proof. The proof of this lemma is available in [61].

Remark 2.3. In the first-order SMCs, the conservative high-value controller gains must be selected for the switching function to ensure the stability. Such gain adjustment and high frequency switching may lead to high level of chattering and exciting the control input, which may degrade the control performance. However, in MSTA, this problem is addressed by applying an integral operation to the switching term which results in a continuous output and thus, alleviating the chattering and preventing the control input excitation.

Remark 2.4. In MSTA, the robust gains are selected based on the bound of the derivative of the uncertainty. As a result, the value of the uncertainty does not affect the robustness as long as the derivative of the uncertainty is in the admissible range. This is a very advantageous feature, since the uncertainty in the hybrid vision and force control system consists of the parameters such as stiffness coefficient, arm lengths, and focal length.

2.4 Experimental Results and Discussion

An experimental setup is provided to test the proposed approach in real time. The setup consists of a 6-DOF DENSO VP6242G robot, a Quanser open architecture control module, a Logitech C270 digital camera with 1280 by 720 pixel resolution with an EIH configuration, two PCs (PC1: CPU i5-2400-3.1GHz and RAM 4GB, PC2: CPU i7-8700-3.7GHz and RAM 16GB), one for controlling the robot and the other for image acquisition, and a 6-axis ATI model 200 industrial automation force sensor with $[-100\ 100]$ N measurement range, 14 bits digital resolution, and 32 LSB/N detection sensitivity installed on the robot end-effector. Also, a piece of rubber is implemented on the tip of tool. The control process sampling time t_s is set to 0.01s. The setup components are shown in Figure 2.4. The actual and/or accurate estimated system parameters are tabulated in Table 2.1 as known parameters. To evaluate the influence of uncertainties on the control process, the parameters are adopted with about 5% change in their values as nominal ones.

Note that the uncertainties are usually emanated from the estimation or calibration errors which have been observed to be smaller than 5%.

Table 2.1. System's physical parameters.

	$[l_1, \dots, l_4, l_{CE}, l_E]$ (m)	a_3 (m)	a_c (m)	f (m)	k_f ($\frac{\text{kN}}{\text{m}}$)
known	[0.28,0.21,0.21,0.07,0.275,0.345]	0.075	0.105	0.004	4.694
Nominal	[0.265,0.2,0.2,0.065,0.2,0.33]	0.08	0.11	0.0038	4.3

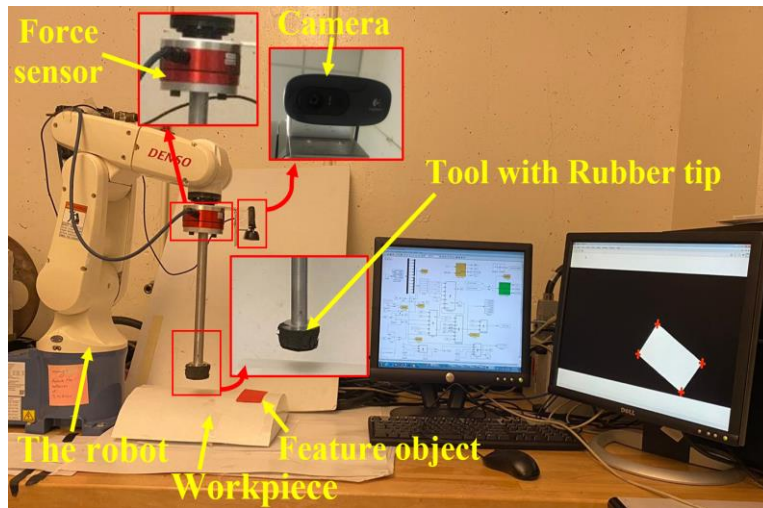


Figure 2.4: Experimental setup.

2.4.1 Extraction of Desired Image Features

In order to comprehensively evaluate the performance of the proposed method in various situations, two experimental tests are designed. In the first test, the effectiveness of the proposed method in terms of free-motion task, hybrid vision and force task, and switching between the two etc. is evaluated. This test comprises two cases. In each case, the robot starts from an initial pose and converges towards the circular path on the workpiece (Figure 2.5a). The desired circular path is designed such that in the odd quarters (i.e., 1st, 3rd,...), the tool moves above the workpiece and has free-motion, and in the even quarters (i.e., 2nd, 4th,...), it touches the workpiece surface and the

hybrid vision and force control is performed. Also, to test the robustness of the hybrid method to workpiece's pose, a various poses are considered for each case (Figure 2.6).

In the second test, the performance of the proposed method in terms of precision, chattering, robustness, and control effort is compared to those of the other well-known methods such as impedance, traditional vision and force (PD/PI), and standard ISMC method. To this end, an infinite-shape path is considered on a workpiece with a curved surface (Figure 2.5b).

For both tests, the desired interacting force is set as a sinusoidal signal. Utilizing the proposed image feature extraction method, the desired image feature signals corresponding to the desired path of both tests are derived and presented in Figure 2.5.c and d. The gains of the proposed controller are set as follows: \bar{k}_1 to $\bar{k}_4 = 7.5, 2.1, 2, 1.05$, $C_1 = D_1 = 1.2$, $C_2 = D_2 = 0.8$, and $\alpha = \beta = 0.5$.

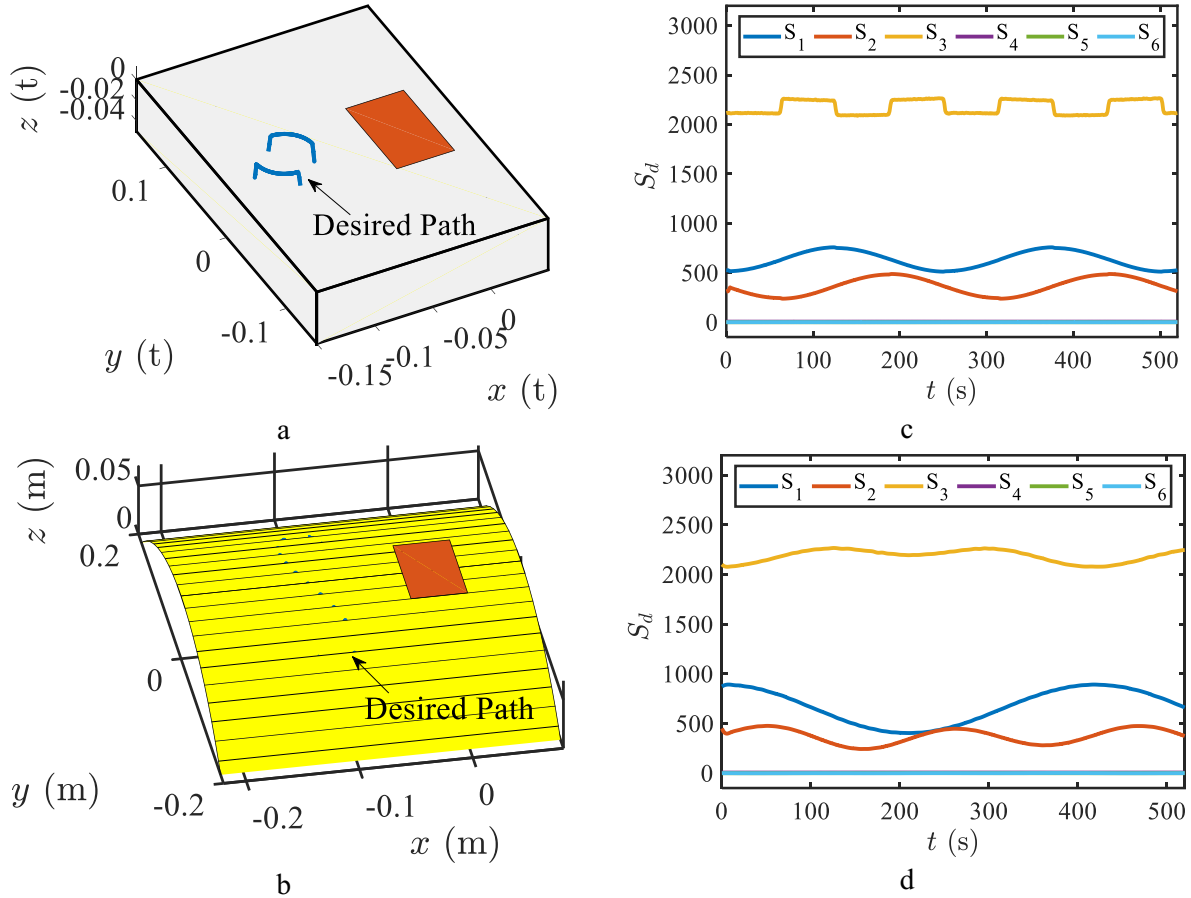


Figure 2.5: Desired path in cartesian space: a) Test 1, b) Test 2, Extracted desired features in image space: c) Test 1, d) Test 2.

2.4.2 Test 1: Free-motion and Hybrid Vision and Force Task

The sequence of the robot behavior for the first test is presented in Figure 2.6. Referring to this figure, the robot starts from the same pose for all cases at the beginning, while the pose of the workpiece varies. Then the robot starts converging towards the desired pose on the workpiece corresponding to the desired image features. Afterwards, the tool-tip interacts with the workpiece and detaches from it several times. Although the pose of the workpiece is different in each case, the tool-tip converges to the same pose relative to the workpiece, which means it is robust to the position and orientation of the workpiece. This advantage is also illustrated with the feature object. The object has different positions and shapes at the beginning of the control process for each case.

However, it has converged to the same position and shape during the control process for both cases. The results of tracking the image features and controlling the interacting force are presented in Figure 2.7 for both cases. Referring to Figure 2.7a, the signals of image features start from different values and then converge towards their desired signals. In Figure 2.7b, the 2-D plot of $S_1 = \bar{x}$ and $S_2 = \bar{y}$ is presented which shows path tracking in the image plane. It can be seen that in both cases, the 2-D image features, i.e., \bar{x} and \bar{y} , have converged to the values of the same point and then tracked the desired path, although their initial positions are different. Besides, Figure 2.7c shows that the interacting force tracks the desired signal properly in both cases. These results show the effectiveness of the proposed algorithm in terms of hybrid control of vision and force on a workpiece with different positions and orientations.

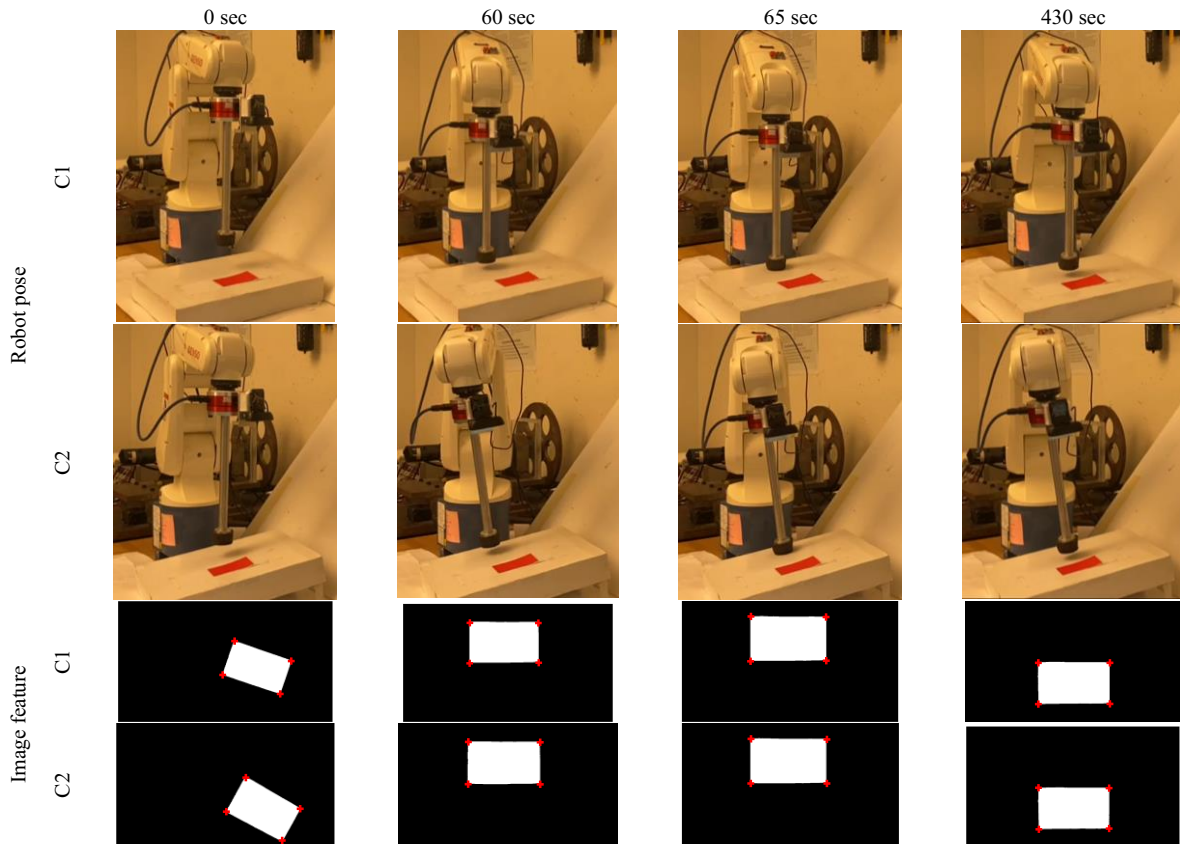


Figure 2.6: Control process of test 1 using the proposed method.

2.4.3 Test 2: Interaction with a Curved Workpiece

The results of the second test are plotted in Figure 2.8 to Figure 2.10. Referring to Figure 2.8a and b, CISMIC outperforms ISMC in terms of tracking image features precision, convergence speed, and chattering level and oscillation. The chattering issue of ISMC is also evident in Figure 2.8c which shows tracking the desired path in the image plane, while CISMIC tracks the desired path smoothly and accurately. Since the image features used in impedance and traditional methods are different from the ones used in CISMIC and ISMC, the norms of the four feature point errors are computed and plotted in Figure 2.8d for comparison. According to this plot, the convergence rate of the CISMIC is higher than those of the impedance and traditional methods. In addition, CISMIC outperforms those methods in terms of tracking precision. Also, as expected, it can be seen that the tracking precision of the impedance method is lower than that of the traditional one. Figure 2.9 shows the results of force control. It can be seen that CISMIC can track the sinusoidal desired signal precisely and smoothly. ISMC can track the desired signal but with high level of chattering. PD/PI and impedance methods have almost failed to track the desired signal and generated high level of error. To compare the chattering and control effort level of the applied controllers, the results of the control input (joint velocities) are presented in Figure 2.10. According to this figure, compared to the ISMC, the level of chattering introduced by CISMIC is mitigated. Also, compared to PD/PI and impedance methods, the level of control effort is much lower, which is the result of having a continuous output and higher precision of CISMIC. Additionally, several numerical indices are considered for a quantitative comparative study. These indices consist of integral absolute error (IAE), integral time absolute error (ITAE), standard deviation (STD), root mean square error (RMSE) and integral absolute controller output (IACO). These indices are

computed for the tracking error and controller output of Test 2 and presented in Table 2.2.

Referring to

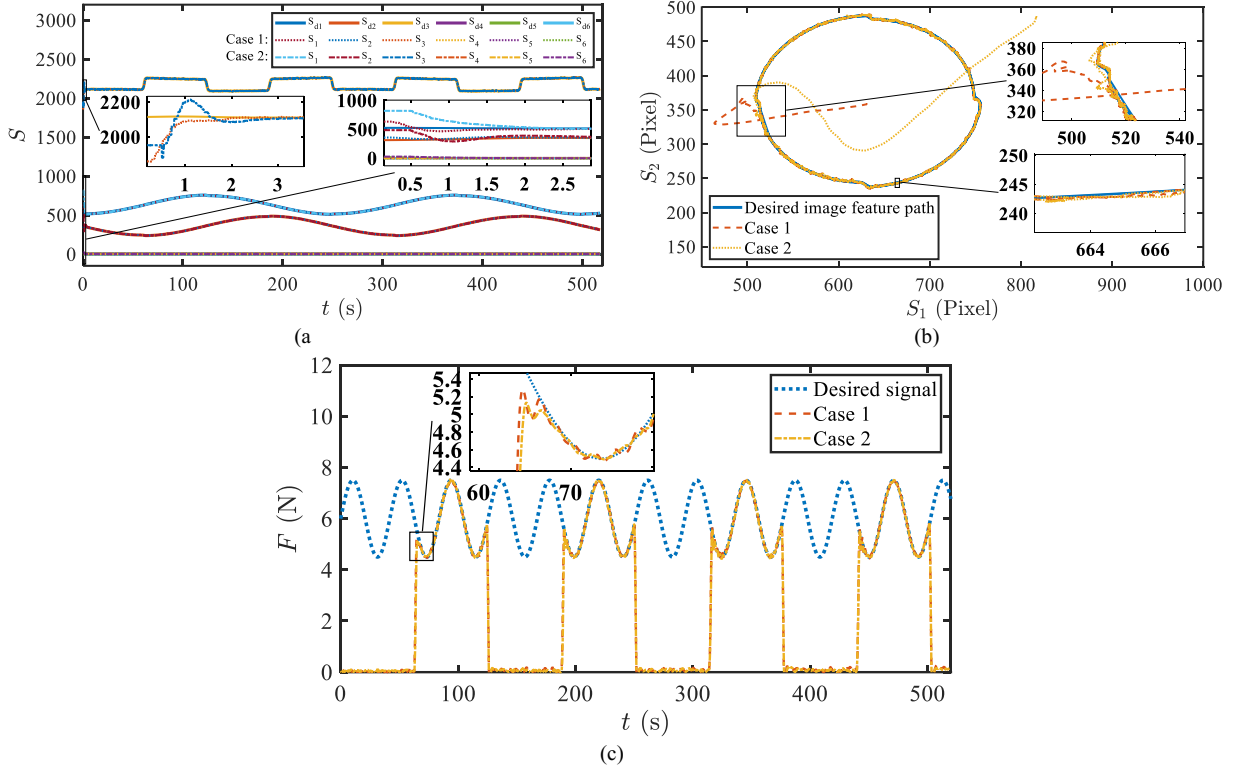


Figure 2.7: Results of Test 1: a) Image feature tracking, b) 2D mage feature tracking, c) Force control.

Table 2.2, CISMIC has improved the vision control performance in comparison with ISMC over 30.1%, 15.1%, 53.9%, and 35.5% in terms of IAE, ITAE, SDT, and RMSE, respectively. Also, it has improved the control performance compared to traditional and impedance methods over 50.7%, 50.1%, 73.6%, 53.6% and 50.8%, 39.9%, 73.7%, 53.71% in terms of IAE, ITAE, SDT, and RMSE, respectively. For force control, CISMIC has improved the performance over 21.7%, 17.1%, 29.4%, and 25.6% in terms of IAE, ITAE, SDT, and RMSE, respectively, compared to ISMC, 53.5%, 54.7%, 47.0%, and 32.2% compared to PD/PI, and 59.1%, 58.4%, 44.5%, and 35.1% compared to impedance method. Accordingly, the numerical results show the superiority of the proposed controller to impedance, traditional, and ISMC methods, in terms of precision, convergence speed, chattering, and control effort.

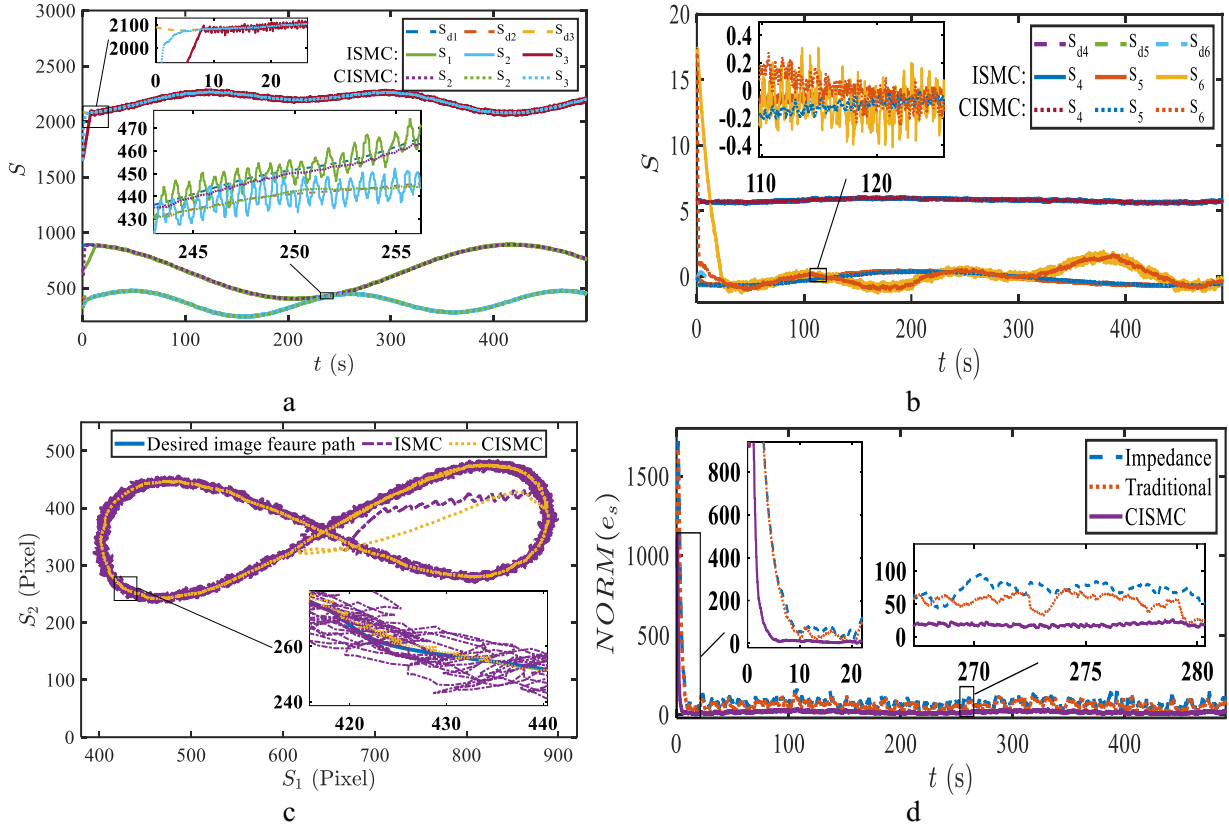


Figure 2.8: Results of Test 2: image feature tracking a) S_1 to S_3 , b) S_4 to S_6 , c) 2D-image path tracking, d) Norm of four image features.

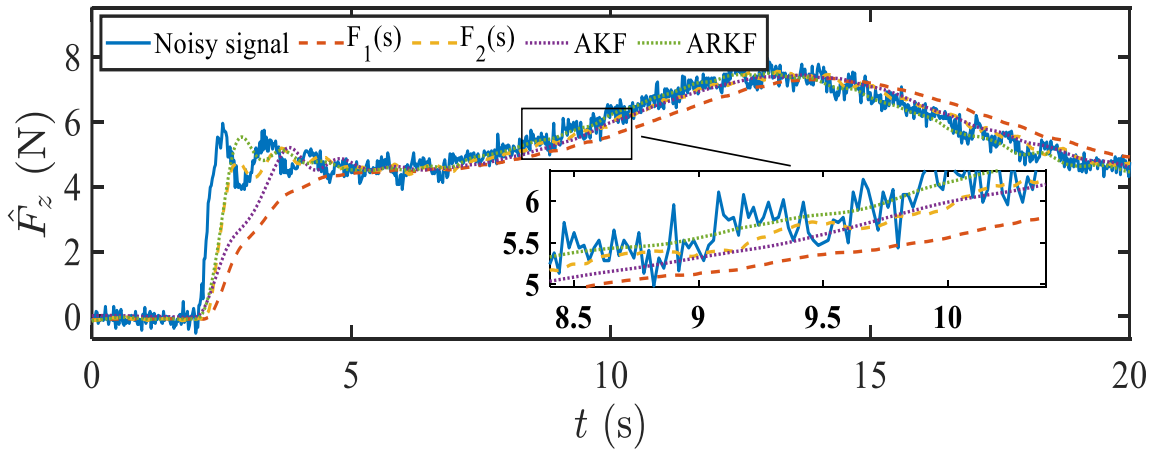


Figure 2.9: Results of test 2 force control.

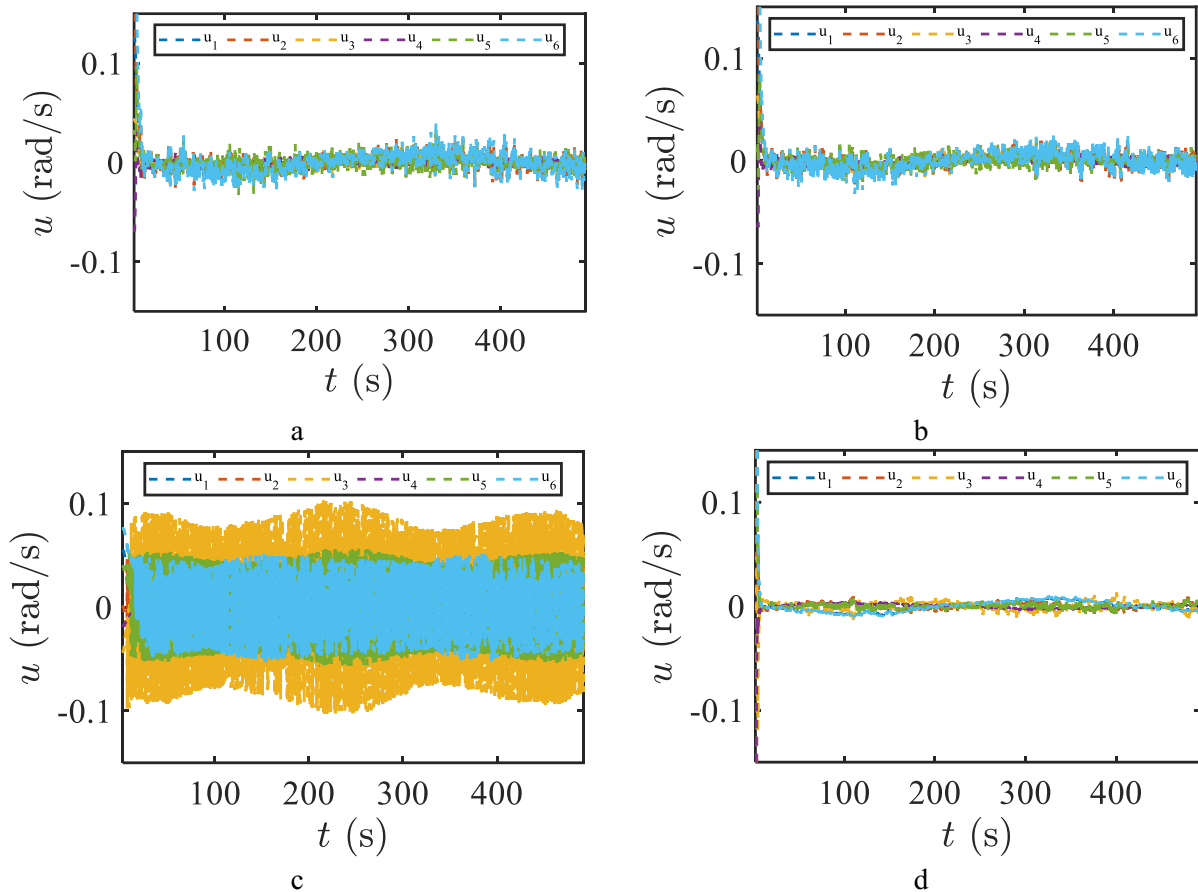


Figure 2.10: Desired path in cartesian space: a) Test 1, b) Test 2, Extracted desired features in image space: c) Test 1, d) Test 2.

Table 2.2: The computed indices for vision and force control in test 2.

	Comp.	Indicator			
		IAE	ITAE	STD	RMSE
Vision	Impedance	18111	512.22e04	29.720	43.412
	PD	18078	513.06e04	29.646	43.395
	ISMC	12728	362.42e04	16.928	30.238
	CISMC	8900	307.54e04	7.8017	20.096
Force	Impedance	695.77	1.7259e05	1.8919	2.1543
	PI	612.99	1.5843e05	1.9807	2.0621
	ISMC	364.52	8.7438e04	1.4886	1.8806
	CISMC	285.19	7.1763e04	1.0498	1.3982

2.5 Summary

In this chapter, a robust cascade vision and force method for industrial robots is presented to control the interaction force while tracking the desired path on the workpiece. A set of six image features with a full rank interaction matrix is employed for designing advanced robust controller with global finite-time stability. The designed CISMV in the inner vision loop and outer force loop of the cascade structure used FTC for its nominal part which result in fast convergence and high tracking precision and MSTA for the discontinuous part to alleviate the chattering. Also, a method is introduced to extract the desired image features from desired 3D-path. Then, CDA is developed to manage the switching between the free-motion and hybrid vision and force tasks. To prove the effectiveness of the proposed method, two experimental tests are designed. In the first test, the performance of proposed method in robustness against the workpiece's pose uncertainty and feasibility of the CDA on a planar workpiece is evaluated. In the second test, the performance of the proposed controller on a curved workpiece is compared with the other methods such as impedance, traditional PD/PI, and ISMC. The results show the superiority of the proposed approach in terms of precision, convergence rate, robustness, control effort, and chattering reduction both graphically and quantitatively.

CHAPTER 3 **Optimal Image-Based Task-Sequence and Path Planning**

3.1 Introduction

As mentioned before, the industrial robot in this study uses an eye-in-hand IBVS. The conventional IBVS methods are not suitable for tracking a trajectory on the image plane or performing a multi-task operation which needs switching between the free-motion and interaction with the workpiece several times. In the previous chapter, a cascade vision and force method was proposed and demonstrated that the controller was able to improve the speed and tracking performance for vision and force control of a single task. However, the failure of the proposed method in dealing with the obstacles on the workpiece or finding the sequence of performing the tasks in a multi-task operation still prevents the method from being fully efficient and being applicable to multi-task operations.

In this chapter, a novel approach on an optimal path/task sequence planning scheme and a robust hybrid vision and force control method is developed.

Building upon the results on the literature, a novel approach named modified APF-constrained generalized TSP (MAPF-CGTSP) is developed to solve the task sequence planning for multi-task operations with the optimal path length and obstacle avoidance. MAPF-CGTSP can be divided into two parts: a) modified APF (MAPF); and b) constrained generalized TSP (CGSTP).

MAPF is the modification of APF in which a rotational repulsive force is added to the repulsive force in 3D space. This repulsive force can be defined by two rotational parameters for each obstacle in the environment. If the parameters of the MAPF are adjusted properly, a deadlock-free

path will be achieved. CGTSP is a TSP problem that can model multi-tasks operations sequence for an industrial robot. Employing MAPF for path planning between each two selected tasks by CGTSP results in MAPF-CGTSP model. Note that the parameters of MAPF are continuous while the sequence of the CGTSP is integers and binaries. Therefore, to adjust the parameters of the MAPF and find the optimal solution of CGTSP a mix-integer optimization algorithm can be employed. To this end, the mix-integer version of multi-tracker optimization algorithms (MTOA) is developed and applied to the problem [62]. Note that MTOA is a population-based optimizer that can find the optimal solution with higher precision and reliability compared to those of the other well-known methods such as genetic algorithm (GA) [63], particle swarm optimization algorithm (PSO) [64], and grey wolf optimizer (GWO) [65]. The objective function of the optimization problem is the summation of the length of the paths between every two tasks generated using the MAPF and CGTSP sequence. When this function is minimized, i.e., MAPF-CGTSP is solved, an optimal path between the optimal sequence of the tasks is generated. Since IBVS method is used for controlling the robot, the initial position of the end-effector (IP) is unknown in the Cartesian space while it is known in the image feature space. Therefore, the cost value cannot be calculated in the cartesian space directly. To address this issue, first, the MAPF-CGTSP is transformed from the Cartesian space into image feature space. To this end, using the real data and a multi-layer perceptron neural network (MLP-NN) [67], [68] a novel method is developed to obtain the image features corresponding to the desired path in the Cartesian space. Then, the equivalent cost value will be calculated using the trajectories in the image feature space.

In this chapter, a novel filtered Quasi SMC (FQSMC) is designed for hybrid vision and force control. FQSMC exploits a variable-gain orthogonal sliding manifold (VGOSM) comprising orthogonal terms of force and vision errors with variable gains. Thus, the convergence of sliding

manifold towards zero leads to the convergences of both force and vision errors towards zero. The variable gains in VGOSM also contribute to increasing the convergence speed, smaller tracking error, and preventing unwanted oscillation. Additionally, a binary contact variable is defined and incorporated in the VGOSM whose value changes when the robot performs free motion or interacts with the surface. A method is also developed to manage to switch between the free-motion and hybrid vision and force operations. FQSMC has a continuous output which results in Quasi-motion and elimination of chattering. Besides, by analyzing the control law of FQSMC, an intrinsic low-pass filter appears, which leads to filtering out the measurement noises associated with the camera and force sensor. Since the intrinsic filter is part of the control law, it will be involved in the stability proof and performance analysis.

3.2 Problem Statement

Referring to Figure 2.1a, a six-DOF serial industrial robot equipped with a force sensor and an eye-in-hand (EIH) camera is considered. The workpiece is fixed with respect to the robot's reference frame. Also, a rectangular feature object is marked on the workpiece's surface whose corners are considered as four feature points (Figure 2.1b). The surface of the workpiece satisfies $f_S(X_S) = 0$ where $f_S: \mathbb{R}^3 \rightarrow \mathbb{R}$ is the constraint function depending on the workpiece geometry; $X_S = (x_s, y_s, z_s)$ is the coordinate of any point on the workpiece's surface.

An operation may consist of two types of tasks: the tasks in which the end-effector should interact with the workpiece while a) tracks a path; b) positions to a single point. For the former tasks, the coordinates of one of the path's endpoints can be considered as the departure point and the other endpoint as the destination point. The desired tracking speed and the desired interaction force are dependent on the position of the tool-tip on the path. For the latter task, the duration of

the regulation on the point is determined. Also, the desired interaction force could be chosen as a function of time. These tasks are defined as follows:

$$\text{Task } i: \begin{cases} \text{Type: } \begin{cases} 1, & \text{for point} \\ 2, & \text{for path} \end{cases} \\ P_{wd}(\vartheta) = [f_x(\vartheta) \quad f_y(\vartheta) \quad f_z(\vartheta)]^T \\ \begin{cases} T_t, & \text{for point} \\ v_d(\vartheta), & \text{for path} \end{cases} \\ \begin{cases} F_{zd}(t), & \text{for point} \\ F_{zd}(\vartheta), & \text{for path} \end{cases} \end{cases} \quad i = 1, 2, \dots, n_T, \quad \vartheta = [0 \quad 1]. \quad (3.1)$$

where n_T is the number of tasks, ϑ is an auxiliary variable which can vary from zero to one; $P_{wd}(\vartheta)$ is the desired path on the planar workpiece which is generated from the departure point to the destination point when ϑ changes from zero to one; T_t is the duration of the interaction with the workpiece for the type 1 tasks, and $v_d(\vartheta)$ is the desired velocity for tracking the type 2 tasks. F_{zd} is the desired interacting force signal, which is the function of time or ϑ for type 1 and type 2 tasks, respectively. Note that $(f_x(\vartheta), f_y(\vartheta), f_z(\vartheta))$, i.e. the coordinate of a point on the predefined path of the task for $\vartheta \in [0 \quad 1]$, must satisfy the surface constraint since the task is defined on the surface of the workpiece, i.e., $f_s(f_x(\vartheta), f_y(\vartheta), f_z(\vartheta)) = 0$.

The main objective is to develop an image-based task sequence/path planning coupled with a hybrid vision and force control method for the industrial robot to complete the entire multi-task operations effectively.

3.3 Image-Based Task Sequence and Path Planning

To accomplish the multi-task operation, the robot should start from its initial position, select a task, and move towards the position above the start point of the path associated with the first task by a free motion. When the robot has fully converged to this position, the robot will move towards

the surface to come into contact with it. Then, the interaction begins, and the robot starts tracking the desired path and the force signal, simultaneously. When the path is tracked completely, the robot will detach from the surface and the first task is completed. Then the robot selects the next task, and the same procedure will be performed. This procedure continues till all tasks are completed. To make this procedure automatic, four main parts must be considered: a) an optimal task sequence/path planning method; b) a mechanism to contact with and/or detach from the workpiece's surface; c) a method to map the desired path from the Cartesian space to image space, and d) a proper vision and force control method for performing the tasks and free motions. The first three items are discussed in the following subsections and a novel hybrid control method will be presented in the next section.

3.3.1 Optimal Task-Sequence and Path Planning

Planning the sequence of the tasks is of significant importance since between every two tasks there is a distance or path that the robot should pass to reach the next task with a free motion (pure IBVS). Optimal sequence planning would decrease the overall length of free motion distance and thereby reduce the operation time and energy consumption. At the same time, generating a feasible and safe path between the tasks and the avoidance of all obstacles in the environment is desired. Therefore, the combination of the task sequence and path planning for a multi-task operation result in decreasing the overall length of the path tracked by the robot for the whole operation. To this end, in this section, a hybrid optimal task sequence/path planning method is developed while avoiding the obstacles. First, the predefined tasks are described in the following subsections, and then, the task sequencing and path planning problems are presented in detail.

3.3.1.1 Predefined Tasks

For type 1 task, the robot is controlled to the desired point. However, for type 2 task, the desired path should be transformed to the desired signals so that the robot can track it. Therefore, the following relation holds for the desired path:

$$(v_d(\vartheta))^2 = \left(\left(\frac{\partial f_x(\vartheta)}{\partial \vartheta} \right)^2 + \left(\frac{\partial f_y(\vartheta)}{\partial \vartheta} \right)^2 + \left(\frac{\partial f_z(\vartheta)}{\partial \vartheta} \right)^2 \right) \left(\frac{d\vartheta}{dt} \right)^2, \quad (3.2)$$

where v_d is the tracking velocity. According to (3.2), $\vartheta(t)$ is derived as follows:

$$\vartheta(t) = \int_0^t v_d(\vartheta) \left(\left(\frac{\partial f_x(\vartheta(t))}{\partial \vartheta(t)} \right)^2 + \left(\frac{\partial f_y(\vartheta(t))}{\partial \vartheta(t)} \right)^2 + \left(\frac{\partial f_z(\vartheta(t))}{\partial \vartheta(t)} \right)^2 \right)^{-\frac{1}{2}} dt. \quad (3.3)$$

By substituting $\vartheta(t)$, given in (3.3), into (3.1), the following desired signal is obtained:

$$\begin{aligned} P_{cd}(t) &= \left[\left(P_{P_{cd}}(t) \right)^T \quad \left(P_{O_{cd}}(t) \right)^T \right]^T, \\ P_{P_{cd}}(t) &= \left[f_x(\vartheta(t)) \quad f_y(\vartheta(t)) \quad f_z(\vartheta(t)) \right]^T, \\ P_{O_{cd}}(t) &= \left[\theta_{xd} \left(P_{P_{cd}}(t) \right) \quad \theta_{yd} \left(P_{P_{cd}}(t) \right) \quad \theta_{zd} \left(P_{P_{cd}}(t) \right) \right]^T, \end{aligned} \quad (3.4)$$

where $(\theta_{xd}, \theta_{yd}, \theta_{zd})$ is the orientation of the end-effector obtained when the end-effector is normal to the workpiece surface on the interaction position, i.e., $rot(P_{O_{cd}}(t)) = \frac{Q_n(t)}{\|Q_n(t)\|}$ where

$Q_n(t) = \left[\frac{\partial f_S(x,y,z)}{\partial x} \quad \frac{\partial f_S(x,y,z)}{\partial y} \quad \frac{\partial f_S(x,y,z)}{\partial z} \right]^T$ at $P_{P_{cd}}(t)$ and $rot(\cdot)$ is the rotation matrix of the end-effector.

3.3.1.2 Task Sequencing Problem

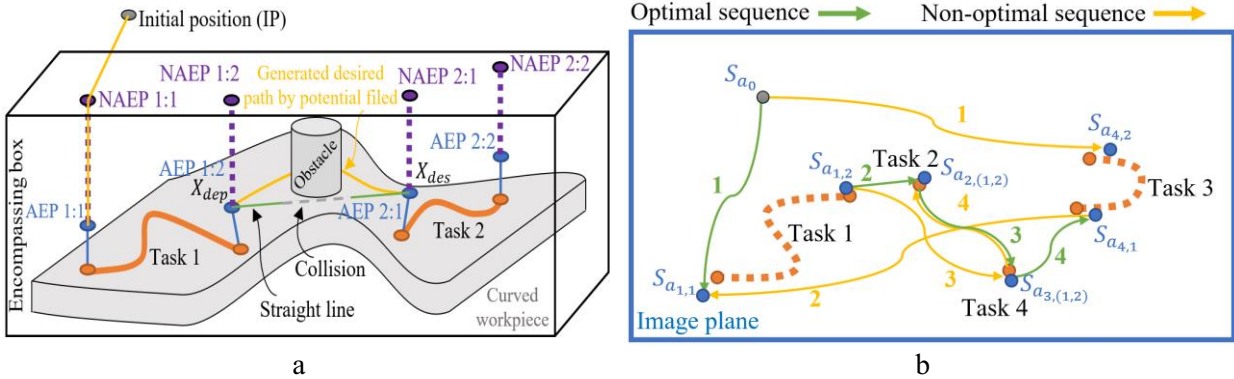


Figure 3.1: Task sequence planning: a) In the workspace, b) In the image plane.

For each path, two points are considered above its end-points with a specific distance d_A called auxiliary end-point (AEP). These AEPs are the departure and destination points when the robot performs free motion for switching between the tasks. When a task completes, the tool-tip detaches from the workpiece and stays on the corresponding AEP. Then, another task is selected, and the robot moves towards the AEP corresponding to the next task to move downwards to the surface and start the interaction. This procedure continues till all tasks are done and the whole operation completes. As mentioned before, since the control process is carried out in feature space, the initial position of the end-effector is unknown in Cartesian space. Thus, to prevent the collision with the workpiece or obstacle at the beginning of the operation, a hypothetical box that encompasses the workpiece and the obstacles can be considered. The height of this box is higher than the workpiece's maximum height and the initial position of the end effector, i.e., IP, is assumed to be higher than the height of the hypothetical box. Then AEPs are extended to the top surface of the box (in the normal direction to the surface of the workpiece) and their intersections with that surface generate some new AEPs called NAEPs. Therefore, to prevent the collision, the robot tracks the line that connects the IP to the selected NAEP. Finally, the robot tracks the connecting

line from the NAEP to the corresponding AEP and continues the operation by selecting the AEPs of the remaining tasks (Figure 3.1a).

The main objective of the task sequence planning, in this study, is to minimize the summation of path lengths between the AEPs of the tasks and the distance between the initial point of the tool-tip and the first AEP. Note that when a path is selected, only one of the AEPs corresponding to its end-points can be selected which is the main property of generalized TSP (GTSP). Furthermore, if the selected task is tracking a path, one of its corresponding AEPs must be selected as the destination point and thus the other corresponding AEP is the departure point of the next sequence. However, if the selected task is a point, its corresponding AEP is considered as both the destination and departure points for the current and next sequences. Therefore, this is a constraint for the end-point selection corresponding to the task. Accordingly, the overall task sequence planning problem can be defined as a constrained GTSP (CGTSP) (Figure 3.1b). The CGTSP is defined as follows,

$$\text{Min: } Cost_{\text{CGTSP}} = \sum_{j=1}^{n_T} \sum_{l=1}^2 (C_{i,j,l} d_{i,j,l}) + \sum_{i=1}^{n_T} \sum_{j=1}^{n_T} \sum_{k=1}^2 \sum_{l=1}^2 (C_{i,j,k,l} d_{i,j,k,l}), \quad (3.5)$$

$$\begin{aligned} \text{Constraints : } & \sum_{i=1}^{n_T} \sum_{k=1}^2 (C_{i,i,k}) = 1; \\ & \sum_{i=1}^{n_T} \sum_{k=1}^2 \sum_{l=1}^2 (C_{i,j,k,l}) = 0; \\ & \sum_{i=1}^{n_T} \sum_{j=1}^{n_T} \sum_{k=1}^2 \sum_{l=1}^2 (C_{i,j,k,l}) = n_T - 1; \\ & \sum_{k=1}^2 \sum_{l=1}^2 (C_{i,j,k,l}) \leq 1 \quad \forall i \in \{1, \dots, n_T\} \& j \in \{1, \dots, n_T\} \end{aligned}$$

where $d_{i,j,k,l}$ is the length of the path between the k^{th} AEP of the i^{th} task and l^{th} AEP of the j^{th} task which is calculated using MAPF explained in the next subsection; $d_{i,j,l} = \|IP - AEP_{j,l}\|$ is the distance between the IP and the l^{th} AEP of the j^{th} task; $C_{i,j,k,l} \in \{0,1\}$ is the binary variable that indicates the connection from k^{th} AEP of the i^{th} task to l^{th} AEP of the j^{th} task, and $C_{i,j,l} \in \{0,1\}$ is the binary variable that indicates the connection from IP to l^{th} AEP of the j^{th} task.

3.3.1.3 Path Planning Using MAPF

In the manufacturing industry, the robots normally perform the operations on the workpieces with complex geometries. Thus, the ability to interact with these kinds of surfaces has been regarded as an important part of the industries [69], [70], [71].

For such workpieces, the free movement from one point to another cannot be performed on a straight line, due to the potential collision. To avoid the collision, the free motion must be done on a path that connects those two points (Figure 3.1a).

For generating a collision-free path, APF method has been a prevailing method [72]. In APF, two kinds of potential fields are considered. a) attractive potential field towards the target destination AEP, i.e., $U_{att}(X)$; and b) repulsive potential fields from the surface of the object, i.e., $U_{rep}(X)$. Accordingly, the overall potential field $U(X)$ is obtained as:

$$U(X) = U_{att}(X) + U_{rep}(X), \quad (3.6)$$

where $X \in \mathbb{R}^3$ is the coordinate of a point in the Cartesian space in the workpiece frame; $U_{att}(X)$ and $U_{rep}(X)$ are as follows:

$$U_{att}(X) = \frac{C_{p1}}{2} \|X - X_{des}\|^2, \quad (3.7)$$
$$U_{rep}(X) = \begin{cases} \frac{C_{p2}}{2} \left(\frac{1}{d_s} - \frac{1}{d_m}\right)^2, & d_s < d_m \\ 0 & , d_s \geq d_m \end{cases},$$

where d_m is the thickness of the inadmissible layer on the surface and $C_{pi}, i = 1,2,3$, are positive constants, X_{des} is the coordinates of the destination point and $d_s = \|X - X_n\|$ is the normal distance to the surface of the workpiece. X_n is the point on the surface, which has the minimum

distance to X . Thus, X_n is the solution of $\begin{cases} f_s(x) = 0 \\ \frac{\partial f_a(x)}{\partial x} = 0 \end{cases}$ where $f_a(x) = \|X - x\|$. According to (3.6)

and (3.7), the overall potential force is calculated as follows,

$$F(X) = F_{att}(X) + F_{rep}(X), \quad (3.8)$$

where $F_{att}(X)$ and $F_{rep}(X)$ are the attractive and repulsive potential forces can be obtained as follows:

$$F_{att} = C_{p1}(X_{des} - X), \quad (3.9)$$

$$F_{rep} = \begin{cases} C_{p2} \frac{1}{d_s^2} \left(\frac{1}{d_s} - \frac{1}{d_m} \right) \nabla_{d_s}, & d_s < d_m \\ 0 & , d_s \geq d_m \end{cases}. \quad (3.10)$$

To generate the desired path from X_{dep} to X_{des} , the steepest decent method with a constant velocity v_m is adopted as follows:

$$X(t) = - \int_0^t \left(\frac{F(X)}{\|F(X)\|} v_m \right) dt + X_{dep}, \quad X(t_{des}) = X_{des}. \quad (3.11)$$

The main disadvantage of APF is its inability to escape from local minima. When repulsive force and attractive force has the same value but in the opposite direction, the equivalent force becomes zero and thus, it sticks in a local minimum point. One way to handle this issue is to use optimization algorithms to adjust the parameters, with the objective of reaching the destination point. However, due to the lack of flexibility, the solution for the optimization problem may not exist. To address this issue, in this paper, APF is modified by adding a rotational force in 3D space which leads to modified APF (MAPF). This rotational force contributes to escape from local minima by deviating the direction of the repulsive force and thus rounding the obstacle. Therefore, the overall potential force will not be zero in the points where the local minima occur and by adjusting the parameters

properly, the problem of local minima can be solved. The direction of the rotational force is normal to the repulsive force and can be calculated as follows:

$$F_{rot}(X) = \frac{\tan(\alpha_{rot}) \cdot F_{rep}(X) \cdot (F_{rep}(X) \times N_{rot})}{\|F_{rep}(X) \times N_{rot}\|}, \quad (3.12)$$

where N_{rot} is the vector normal to the plane that passes through the departure and destination points and is fixed with a specific angle β_{rot} . An example of the rotational force in 3D space is depicted in Figure 3.2. Therefore, the overall potential force can be rewritten as follows:

$$F(X) = F_{att}(X) + F_{rep}(X) + F_{rot}(X). \quad (3.13)$$

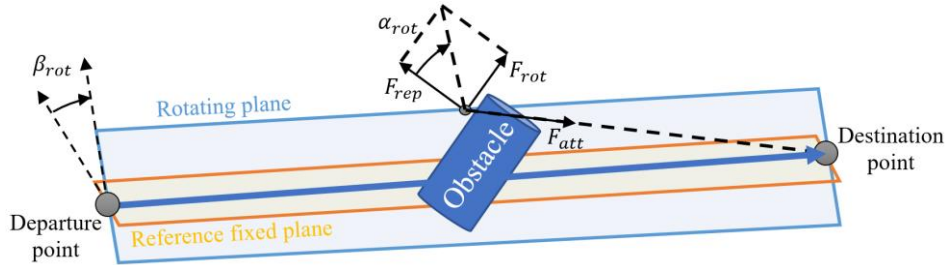


Figure 3.2: Rotational potential force.

3.3.1.4 CGTSP-MAPF

As mentioned before, to solve the CGTSP, the length of the paths between each task should be known. These paths, however, are generated using MAPF whose parameters should be adjusted properly by an optimization algorithm. It is advantageous to merge both CGSTP and MAPF optimization problems as one optimization problem. Note that since the parameters of CGSTP and MAPF are binary and continuous, the resultant optimization problem would be a mix-integer one. To this end, a mix-integer version of MTOA is developed and employed to solve this problem which is discussed in the following subsections.

a) CGTSP-MAPF Optimization Problem

Since the control process is carried out in the image feature space, the generated path by MAPF must be transformed into this space. Besides, the initial pose of the end-effector in the Cartesian space is unknown. Thus, without the loss of generality, the paths between the AEPs in cartesian space are replaced with the corresponding trajectories in the image feature space whose length can be calculated as follows,

$$\bar{d}_{ab} = \int_0^{T_{ab}} (S_{MAPF_{ab}}^T \mathbf{W}_p S_{MAPF_{ab}}) dt, \quad (3.14)$$

where $S_{MAPF_{ab}} \in \mathbb{R}^6$ is the normal image feature vector corresponding to a point on the path between point a and b ; and $\mathbf{W}_p \in \mathbb{R}^{6 \times 6}$ is the positive definite orthogonal matrix to be defined by the user. Note that S_{MAPF} is defined as follows:

$$S_{MAPF} = \begin{bmatrix} \frac{\bar{x}_c}{\sqrt{\bar{D}_c}} & \frac{\bar{y}_c}{\sqrt{\bar{D}_c}} & \frac{\sqrt{\bar{D}_c}}{c_z} & \bar{\theta}_{cx} & \bar{\theta}_{cy} & \bar{\theta}_{cz} \end{bmatrix}^T, \quad (3.15)$$

where c_z is the coefficient of the depth in the image plane which is calculated based on the size of the image object. To map the generated path in the cartesian space to the image plane an MLP neural network is developed, which will be described in detail. It is worth mentioning that \bar{d}_{ab} is a function of MAPF parameters, i.e.,

$\{C_{p1}, C_{p2_0}, \dots, C_{p2_{n_o}}, \alpha_{rot1}, \dots, \alpha_{rot_{n_o}}, \beta_{rot1}, \dots, \beta_{rot_{n_o}}, d_{m_0}, \dots, d_{m_{n_o}}\}$, which are adjusted by the

optimization algorithm. Accordingly, based on (3.5), the overall CGSTP-MAPF optimization problem is derived as follows,

$$\text{Min: } Cost_{CGTS-MAPF} = \sum_{j=1}^{n_T} \sum_{l=1}^2 (C_{i,j,l} \bar{d}_{i,j,l}) + \sum_{i=1}^{n_T} \sum_{j=1}^{n_T} \sum_{k=1}^2 \sum_{l=1}^2 (C_{i,j,k,l} \bar{d}_{i,j,k,l}), \quad (3.16)$$

$$\begin{aligned} \text{Constraints : } & \sum_{i=1}^{n_T} \sum_{k=1}^2 (C_{i,k}) = 1; \\ & \sum_{i=1}^{n_T} \sum_{k=1}^2 \sum_{l=1}^2 (C_{i,j,k,l}) = 0; \end{aligned}$$

$$\sum_{i=1}^{n_T} \sum_{j=1}^{n_T} \sum_{k=1}^2 \sum_{l=1}^2 (C_{i,j,k,l}) = n_T - 1;$$

$$\sum_{k=1}^2 \sum_{l=1}^2 (C_{i,j,k,l}) \leq 1 \quad \forall i \in \{1, \dots, n_T\} \& j \in \{1, \dots, n_T\},$$

Optimization Variables:

$$\text{MAPF variables: } \{C_{p_1}, C_{p_2}, \dots, C_{p_{2n_o}}, \alpha_{rot_1}, \dots, \alpha_{rot_{n_o}}, \beta_{rot_1}, \dots, \beta_{rot_{n_o}}, d_{m_0}, \dots, d_{m_{n_o}}\} \in \mathbb{R}^+$$

$$\text{CGSTP variables: } C_{i,k} \in \{0,1\}$$

b) Mix-integer MTOA

To solve the CGTSP-MAPF, the mix-integer version of MTOA is developed and employed. MTOA, which is a population-based optimization algorithm, was developed by Zakeri et al. in 2017 [66]. MTOA is composed of two types of trackers, global G_T and local L_T . During the search process, the global tracker, G_T s, using stochastic motion and information from L_T s, explore to find the global optimal point (GOP), (3.17), [66]. The number of the local trackers is predetermined; each of them explores in a neighborhood of the corresponding G_T with radius R_S , (3.18), to find the local optimal point, LP. The search radius around each G_T is determined by its rank, RK. The search process of this algorithm is described in detail in [66].

$$G_i = \beta(GOP - G_{T_i}) + (1 - \beta)(LP_i - G_{T_i}), 0 \leq \beta \leq 1 \quad (3.17)$$

$$R_{S_i} = \begin{cases} Rf_i, & Rf_i \geq Rd_i \\ Rd_i, & Rf_i < Rd_i \end{cases} \quad (3.18)$$

$$Rf = \frac{RK_i - 1}{nop - 1} \cdot (RM - Rm) + Rm,$$

$$Rd_i = \|G_{T_i} - GOP\|,$$

where Rm and RM are the predefined minimum and maximum search radii, respectively. Note that to make MTOA applicable for integer optimization variables, the following relation has been used:

$$X_{int} = \frac{[X_{con} \cdot (1 + X_{intMAX} - X_{intMin})]}{X_{conMAX} - X_{conMin}} + X_{intMin} , \quad (3.19)$$

where $[.]$ denotes the floor function, X_{con} and X_{int} are the continuous and integer variables for the optimization, respectively. X_{conMAX} , X_{conMin} , X_{intMAX} , and X_{intMin} are the maximum and minimum of the continuous and integer variables, respectively.

3.3.2 Mapping From Cartesian Space to Image Plane

In IBVS, $S(t)$ is the set of image features corresponding to the pose of the camera (or end-effector) with respect to the workpiece frame $\{F_f\}$ at the time instant t , i.e., $P_c(t)$. However, defining $S_d(t)$, which is the set of desired image features corresponding to the desired pose $P_{cd}(t)$, is a challenging task. To this end, two main approaches have been suggested [48]: a) extracting analytical relationship between $P_{cd}(t)$ and $S_d(t)$; and b) experimental derivation of $S_d(t)$ when the camera pose is adjusted to $P_{cd}(t)$ manually, i.e., image trajectory planning based on robot programming by demonstration [48].

However, the first method may not be precise in the practice due to existing uncertainties in the camera's intrinsic and extrinsic parameters and the second method involves a cumbersome procedure which makes it inappropriate for tracking the desired paths. In this study, to handle these problems, the combination of these two methods is considered. First, the analytical relationship between $\hat{S}_d(t)$ and $P_{cd}(t)$ is derived. Then, $\hat{S}_d(t)$ passes through a three-layer multi-layer perceptron (MLP) neural network [67] whose output, \bar{S}_d , is the estimation of S_d . Then, the NN is trained to minimizing $e_{sd} = \bar{S}_d - S_d$.

Let $\hat{f}_{sd}: \mathbb{R}^6 \rightarrow \mathbb{R}^6$ be the analytical function that takes the desired pose and returns the estimated corresponding desired feature, i.e., $\hat{S}_d(t) = \hat{f}_{sd}(P_{cd}(t))$. Using NN, \bar{S}_d is obtained as:

$$\bar{S}_d(t) = \text{NN}_{\text{sd}}(\hat{f}_{\text{sd}}(P_{\text{cd}}(t))) = \hat{f}_{\text{sd}}(P_{\text{cd}}(t)) + \mathbf{W}_3 f_{\text{sig}}(\mathbf{W}_2 f_{\text{sig}}(\mathbf{W}_1 \hat{S}_d + B_1) + B_2) + B_3 \quad (3.20)$$

where, $f_{\text{sig}}(\star) = \frac{1}{1+e^{-\star}}$ is the sigmoid activation function. $\mathbf{W}_1 \in \mathbb{R}^{n_1 \times 6}$, $\mathbf{W}_2 \in \mathbb{R}^{n_2 \times n_1}$, and $\mathbf{W}_3 \in \mathbb{R}^{6 \times n_2}$ are weight matrices and $B_1 \in \mathbb{R}^{n_1}$, $B_2 \in \mathbb{R}^{n_2}$, and $B_3 \in \mathbb{R}^6$ are the biases of the NN, all of which are tuned by training. n_1 and n_2 are the number of neurons in the first and second hidden layers. The topology of the adopted NN is illustrated in Figure 3.3a.

To train the NN, a set of desired poses, P_{SD} , which are selected randomly with a uniform probability distribution in the workspace, is determined as follows:

$$P_{\text{SD}} = \{P_{R_1} \quad P_{R_2} \quad \cdots \quad P_{R_{n_d}}\}, \quad (3.21)$$

where P_{R_1} to $P_{R_{n_d}}$ are the preselected desired poses, and n_d is the number of sampling data. Then, the sets of image features, S_{SD} , corresponding to P_{SD} are acquired as:

$$S_{\text{SD}} = \{S_{D_1} \quad S_{D_2} \quad \cdots \quad S_{D_{n_d}}\}, \quad (3.22)$$

where S_{D_i} is the real image feature corresponding to P_{R_i} acquired in experiment. The pair of S_{SD} and P_{SD} can be used to train the NN using Levenberg-Marquardt (LM) method to minimize the following cost function [73]:

$$\text{Cost} = \sum_{i=1}^{n_d} (S_{D_i} - \text{NN}_{\text{sd}}(P_{R_i}))^T \mathbf{C}_{\text{NN}} (S_{D_i} - \text{NN}_{\text{sd}}(P_{R_i})), \quad (3.23)$$

where Cost is the cost function, and $\mathbf{C}_{\text{NN}} \in \mathbb{R}^{6 \times 6}$ is the diagonal positive definite matrix of cost value weight.

Besides the mapping network, an approach is needed to manage detachment from and contact with the workpiece's surface. The main desired path is defined on the workpiece's surface. Then, consider two other desired paths: one is rendered by moving the main desired path above the

surface, called P_{dF} , and the other beneath it, called P_{dI} , with the margin shown in Figure 3.3b. The desired features corresponding to those paths are \bar{S}_{dF} and \bar{S}_{dI} , respectively. Accordingly, if the robot needs to detach from the surface, i.e., free motion, \bar{S}_{dF} is selected and if the robot needs to interact with the surface, \bar{S}_{dI} is chosen. Once the tool contacts with the surface, the binary switching variable $\psi \in \{0,1\}$ is set to 1 and hybrid control is conducted, provided that \bar{S}_{dI} is selected as the desired path. Otherwise, $\psi = 0$ and free motion is carried out. This is done by incorporating ψ into the sliding variable which will be described in the next section.

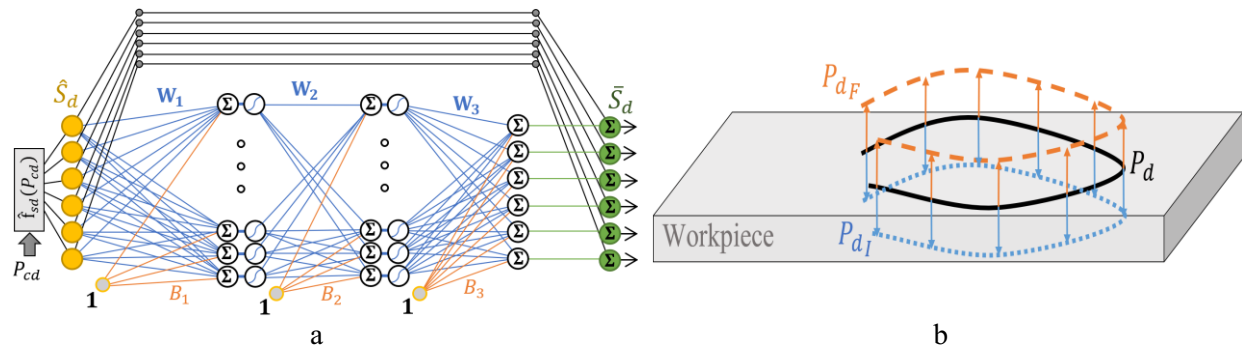


Figure 3.3: a) The three-layer NN, b) P_d , P_{dF} , and P_{dI} .

3.4 Hybrid Vision and Force Controller Design

In this section, FQSMC is designed to exploit a novel VGOSM for hybrid control of vision and force which leads to robustness against uncertainties and noises. It also can control the robot for both free-motion and hybrid vision and force tasks.

3.4.1 Variable-Gain Orthogonal Sliding Manifold

3.4.1.1 Orthogonal Sliding Manifold Design

Consider the suggested sliding manifold $\sigma \in \mathbb{R}^6$ as follows:

$$\sigma = \sigma_F + \sigma_S, \quad (3.24)$$

where $\sigma_F \in \mathbb{R}^6$ and $\sigma_S \in \mathbb{R}^6$ are orthogonal vectors associated with the force error and the image feature error, respectively, presented as follows:

$$\sigma_F = \mathbf{Q}e_F, \sigma_S = \mathbf{K}_c(\mathbf{I} - \mathbf{Q})e_P, \quad (3.25)$$

where $e_F \in \mathbb{R}^6, e_P \in \mathbb{R}^6$, and $\mathbf{Q} \in \mathbb{R}^{6 \times 6}$ are the vectors of force and robot pose errors and the compliance selection matrix, respectively, presented in (3.26); $\mathbf{K}_c \in \mathbb{R}^{6 \times 6}$ is a positive definite orthogonal matrix whose terms are variable, which will be discussed in the next subsection.

$$e_F = F - F_d, e_P = \hat{\mathbf{L}}_S^{-1} e_S, \mathbf{Q} = \psi D^T D, e_S = S - S_d, \quad (3.26)$$

where, $F_d \in \mathbb{R}^6$ is the vector of desired forces, and $e_S \in \mathbb{R}^6$ is the vector of image feature errors, $S_d \in \mathbb{R}^6$ is the vector of desired image features, $D \in \mathbb{R}^6$ is the selection vector whose entries are either zero or one, corresponding to directions where the exerted force must be controlled, ψ is zero when the robot has a free motion and one when the robot is interacting with the workpiece whose value is determined by the TM algorithm. In this research, the interaction force in the normal direction to the end-effector is controlled. Thus, D is defined as follows:

$$D = [0 \quad 0 \quad 1 \quad 0 \quad 0 \quad 0]. \quad (3.27)$$

In **Theorem 3.2**, it is proved that σ_F and σ_P are orthogonal. Hence, if $\lim_{t \rightarrow +\infty} \sigma = 0$, then $\lim_{t \rightarrow +\infty} \sigma_F =$

$\lim_{t \rightarrow +\infty} \sigma_S = 0$ i.e., the objective of the vision and force control is achieved.

Theorem 3.2. σ_F and σ_P vectors are orthogonal.

Proof. consider the following relation:

$$\sigma_{FS} = \sigma_F \cdot \sigma_S = \sigma_F^T \sigma_S, \quad (3.28)$$

where σ_{FP} is the results of dot-product of σ_F and σ_S . Substituting (3.25) into (3.28) yields:

$$\sigma_{FS} = (\mathbf{Q}e_F)^T(\mathbf{K}_c(\mathbf{I} - \mathbf{Q})e_P). \quad (3.29)$$

Since \mathbf{K}_c and \mathbf{Q} are diagonal, (3.29) can be rewritten as:

$$\sigma_{FS} = e_F^T \mathbf{Q}(\mathbf{I} - \mathbf{Q})\mathbf{K}_c e_P. \quad (3.30)$$

In (3.30), $\mathbf{Q}^T(\mathbf{I} - \mathbf{Q}) = \mathbf{0}$, thus $\sigma_{FS} = 0$. Referring to [74], if the dot product of two vectors is zero, they are orthogonal, i.e., σ_F and σ_S are orthogonal and the proof is completed.

3.4.1.2 Variable Gain of the Vision Term

One way to reduce the response time of IBVS is to increase the gain values in the control law. However, there is a limitation on this value because the high gain in IBVS controller tends to make the robotic system shaky and unstable. On the other hand, low gains may make the system very slow [75], [76]. To handle this issue, adaptive variable-gain IBVS and switch IBVS have been suggested, [75], [76], [77]. In the adaptive variable-gain method, the value of the control gain changes based on the norm of feature errors. When the norm is large, the gain sets to a large value to speed up the convergence rate. On the other hand, when the norm is small, the control gain is set to a small value to prevent unwanted oscillation and instability [76]. In the switch IBVS method, the visual motion is decomposed into translational and orientational motions of the camera, respectively. Then, each motion is controlled independently and with different feedback gains. However, due to the switching nature of this method, it is only applicable to vision control systems that are designed for regulation purposes [75]. Hence, it cannot be utilized in this study.

Based on the two mentioned methods, a novel variable gain using tangent hyperbolic function is developed for the vision term in the VGOSM. The continuous nature of the obtained method makes it possible to be adopted for vision systems with tracking trajectory purposes. In (3.25), \mathbf{K}_c is identical to the feedback control gain of switch IBVS in [75] which is defined as $\mathbf{K}_c =$

$\begin{bmatrix} \mathbf{K}_t & \mathbf{0}_{3 \times 3} \\ \mathbf{0}_{3 \times 3} & \mathbf{K}_a \end{bmatrix}$, where $\mathbf{K}_t \in \mathbb{R}^{3 \times 3}$ and $\mathbf{K}_a \in \mathbb{R}^{3 \times 3}$ are positive definite diagonal matrices of feedback

gains associated with the translational and orientational motions of the camera, respectively. Also, translational and orientation errors of the camera motion are $e_{Pt} \in \mathbb{R}^3$ and $e_{Pa} \in \mathbb{R}^3$, respectively, determined as $e_p = [e_{Pt}^T \quad e_{Pa}^T]^T$. Accordingly, the variable-gain relation is suggested as follows:

$$\begin{aligned} \mathbf{K}_t &= \left(\frac{\tanh(a_t \|e_{Pt}\| + b_t) + 1}{2} (\mathbf{c}_{H_t} - \mathbf{c}_{L_t}) + \mathbf{c}_{L_t} \right) \mathbf{I}_{3 \times 3}, \\ \mathbf{K}_a &= \left(\frac{\tanh(a_a \|e_{Pa}\| + b_a) + 1}{2} (\mathbf{c}_{H_a} - \mathbf{c}_{L_a}) + \mathbf{c}_{L_a} \right) \mathbf{I}_{3 \times 3}, \end{aligned} \quad (3.31)$$

where a_t , a_a , b_t , and b_a are adjustable parameters that determine the characteristics of the smooth switching function $\tanh(\cdot)$. \mathbf{c}_{H_t} , \mathbf{c}_{H_a} , \mathbf{c}_{L_t} , and \mathbf{c}_{L_a} are the lower and upper bounds of the feedback gains. The above equation aims to provide adjustable gains based on the errors. According to this equation, it can be seen that as the error decreases, the gain values of K_t and K_a changes from their high-level values \mathbf{c}_{H_t} , \mathbf{c}_{H_a} to their low-level values \mathbf{c}_{L_t} , and \mathbf{c}_{L_a} . As a result, the vision system converges fast when the error is high and avoids oscillation when the error is low.

3.4.2 Filtered Quasi Sliding Mode Controller

FQSMC not only is robust against uncertainties, but also filters out the noise in the feedback. It exploits a filter within its control law which is also considered in the procedure of its stability proof. Additionally, its continuous output leads to a chattering-free SMC. All of these features make FQSMC a candidate for the systems subject to large uncertainties and measurement noises such as the one in this study.

3.4.2.1 Control Law Design

To derive the FQSMC control law, the time derivative of σ is taken. It results in appearing the system input, i.e., $u = \dot{q}$. Thus, $\dot{\sigma}$ is obtained as follows:

$$\dot{\sigma} = \mathbf{Q}\dot{e}_F + (\text{diag}\{e_P\}(\mathbf{I} - \mathbf{Q})\mathbf{J}_K + \mathbf{K}_C(\mathbf{I} - \mathbf{Q}))\hat{\mathbf{L}}_s^{-1}\dot{e}_s, \quad (3.32)$$

where $\mathbf{J}_K = \frac{\partial \text{md}\{\mathbf{K}_C\}}{\partial e_P}$, in which $\text{md}\{\star\}$ is the function that takes a squared matrix \star and returns its main diagonal as a vector. Taking time derivatives of (3.26) and then, substituting (2.11) and (2.15) and into it, results in the following relations:

$$\dot{e}_F = \hat{K}_f \hat{\mathbf{J}}_q u + \bar{\delta}_F - \dot{F}_d, \quad \dot{e}_s = \hat{\mathbf{L}}_s \hat{\mathbf{J}}_q u + \bar{\delta}_s - \dot{S}_d. \quad (3.33)$$

Substituting (3.33) into (3.32) yields:

$$\dot{\sigma} = \mathbf{Q}(\hat{K}_f \hat{\mathbf{J}}_q u - \dot{F}_d) + (\text{diag}\{e_P\}(\mathbf{I} - \mathbf{Q})\mathbf{J}_K + \mathbf{K}_C(\mathbf{I} - \mathbf{Q}))\hat{\mathbf{L}}_s^{-1}(\hat{\mathbf{L}}_s \hat{\mathbf{J}}_q u - \dot{S}_d) + \delta_L, \quad (3.34)$$

where

$$\delta_L = \mathbf{Q}\bar{\delta}_F + (\text{diag}\{e_P\}(\mathbf{I} - \mathbf{Q})\mathbf{J}_K + \mathbf{K}_C(\mathbf{I} - \mathbf{Q}))\hat{\mathbf{L}}_s^{-1}\bar{\delta}_s, \quad (3.35)$$

Based on (3.34), the FQSMC law can be obtained as follows:

$$u = (\mathbf{Q}\hat{K}_f \hat{\mathbf{J}}_q + (\text{diag}\{e_P\}(\mathbf{I} - \mathbf{Q})\mathbf{J}_K + \mathbf{K}_C(\mathbf{I} - \mathbf{Q}))\hat{\mathbf{J}}_q)^{-1} \left(\eta + \mathbf{Q}\dot{F}_d + (\text{diag}\{e_P\}(\mathbf{I} - \mathbf{Q})\mathbf{J}_K + \mathbf{K}_C(\mathbf{I} - \mathbf{Q}))\hat{\mathbf{L}}_s^{-1}\dot{S}_d \right), \quad (3.36)$$

where

$$\begin{aligned} \eta &= -\mathbf{\Lambda}_1^{-1}\mathbf{\Lambda}_3\sigma_C - \mathbf{\Lambda}_1^{-1}\text{sat}(\boldsymbol{\Phi}^{-1}\sigma_C) \\ \dot{\sigma}_C &= -\mathbf{\Lambda}_2\sigma_C + \mathbf{\Lambda}_1\sigma \end{aligned}, \quad (3.37)$$

$$\text{sat}(\boldsymbol{\Phi}^{-1}\sigma_C) = \begin{cases} \boldsymbol{\Phi}^{-1}\sigma_C, & |\boldsymbol{\Phi}^{-1}\sigma_C| < \mathbf{K} \\ \mathbf{K} \text{sign}(\boldsymbol{\Phi}^{-1}\sigma_C), & |\boldsymbol{\Phi}^{-1}\sigma_C| \geq \mathbf{K} \end{cases} \quad (3.38)$$

In (3.37) and (3.38), $\eta \in \mathbb{R}^6$ is the reaching law and σ_C is the filtered value of σ ; $\boldsymbol{\Phi} \in \mathbb{R}^{6 \times 6}$ is the positive definite orthogonal matrix of the boundary layer thickness; $\mathbf{K} \in \mathbb{R}^6$ is the saturation threshold whose value is set based on the bounds of system uncertainties. The schematic of FGSMC is shown in Figure 3.4.

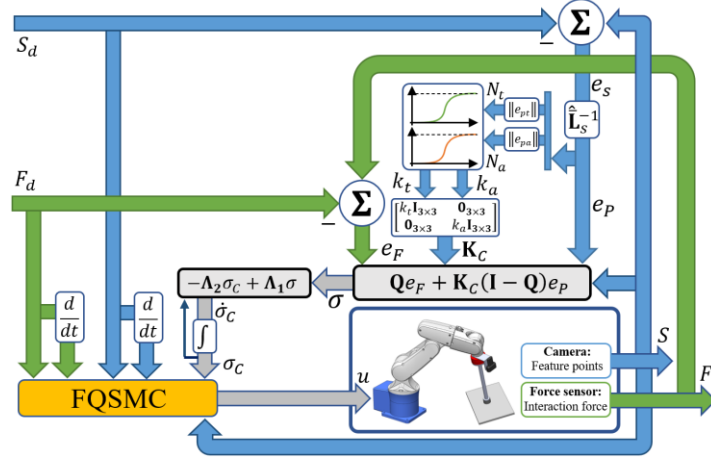


Figure 3.4: Schematic of the proposed robust hybrid controller.

3.4.2.2 Stability Analysis

The stability proof of FQSMC is presented in **Theorem 3.3**. A necessary assumption for this theory is considered as follows:

Assumption 3.1. The following relation holds for δ_L :

$$|\delta_L| \leq D_L \mid D_L \in \mathbb{R}^{6 \times 1}, D_L > 0. \quad (3.39)$$

Theorem 3.3. Under the condition of (3.40), applying the FQSMC law of (3.36) to the dynamic system of (3.34) leads to its stability with a Quasi-sliding motion, i.e., $|\sigma| < \delta_B$ for all $t \geq T_r$ where $\delta_B, \epsilon_\sigma > 0$ and $T_r > 0$ (3.23), provided that Assumption is satisfied.

$$\begin{aligned} \Lambda_1, \Lambda_2, \Lambda_3 > 0, \mathbf{K} > \Lambda_1 D_L, (\Lambda_2 - \omega \mathbf{I}) > \mathbf{0}, \\ \sqrt{2}(\Lambda_2 - \omega \mathbf{I})^{\frac{1}{2}} \sqrt{2\omega} \Lambda_3^{\frac{1}{2}} \geq |(\gamma \mathbf{I} - \omega \Lambda_2 - \Lambda_3)| + 2\Phi, \\ \Lambda_2^2 - 4(\Lambda_3 + \Phi^{-1}) \geq 0, 0 < \omega < 1, \gamma > 1. \end{aligned} \quad (3.40)$$

Proof. Substituting (3.36) into (3.34) yields:

$$\begin{cases} \dot{\sigma} = -\Lambda_1^{-1} \Lambda_3 \sigma_C - \Lambda_1^{-1} \text{sat}(\Phi^{-1} \sigma_C) + \delta_L \\ \dot{\sigma}_C = -\Lambda_2 \sigma_C + \Lambda_1 \sigma \end{cases}. \quad (3.41)$$

By taking the time derivative of the second row of (3.41) and substituting it into its first row, the following relation is obtained:

$$\ddot{\sigma}_c = -\mathbf{\Lambda}_2 \dot{\sigma}_c - \mathbf{\Lambda}_3 \sigma_c - \text{sat}(\boldsymbol{\Phi}^{-1} \sigma_c) + \mathbf{\Lambda}_1 \delta_L. \quad (3.42)$$

Consider the following candidate Lyapunov function:

$$V = \gamma \sigma_c^T \sigma_c + 2\omega \sigma_c^T \dot{\sigma}_c + \dot{\sigma}_c^T \dot{\sigma}_c. \quad (3.43)$$

Based on (3.40), it can be deduced that $\omega < \gamma^{1/2}$. This inequality results in the following relation:

$$|2\omega \sigma_c^T \dot{\sigma}_c| \leq \left| 2\gamma^{\frac{1}{2}} \sigma_c^T \dot{\sigma}_c \right|, |\gamma \sigma_c^T \sigma_c| \geq 0, |\dot{\sigma}_c^T \dot{\sigma}_c| \geq 0. \quad (3.44)$$

Additionally, the following relation holds:

$$(\gamma \sigma_c^T \sigma_c + \dot{\sigma}_c^T \dot{\sigma}_c) = \gamma \sigma_c^T \sigma_c + \dot{\sigma}_c^T \dot{\sigma}_c \geq 0. \quad (3.45)$$

By comparing (3.44) with (3.45), it can be deduced that $\gamma \sigma_c^T \sigma_c + 2\omega \sigma_c^T \dot{\sigma}_c + \dot{\sigma}_c^T \dot{\sigma}_c = V = 0$ when $(\sigma_c, \dot{\sigma}_c) = (0,0)$ and $V > 0$ when $(\sigma_c, \dot{\sigma}_c) \neq (0,0)$: the required condition of a Lyapunov function [78], \dot{V} is obtained as follows:

$$\dot{V} = 2\gamma \sigma_c^T \dot{\sigma}_c + 2\omega \dot{\sigma}_c^T \dot{\sigma}_c + 2\omega \sigma_c^T \ddot{\sigma}_c + 2\dot{\sigma}_c^T \ddot{\sigma}_c. \quad (3.46)$$

To prove the Quasi SMC under the proposed control law, the attraction towards the boundary layer should be illustrated, i.e., when $|\boldsymbol{\Phi}^{-1} \sigma_c| \geq \mathbf{K}$, $\dot{V} < 0$. Substituting (3.42) into (3.46) yields:

$$\begin{aligned} \dot{V} = & \dot{\sigma}_c^T (2(\gamma \mathbf{I} - \omega \mathbf{\Lambda}_2 - \mathbf{\Lambda}_3) \sigma_c - 2(\mathbf{K} \text{sign}(\sigma_c) - \mathbf{\Lambda}_1 \delta_L)) - 2\dot{\sigma}_c^T (\mathbf{\Lambda}_2 - \omega \mathbf{I}) \dot{\sigma}_c - \\ & 2\omega \sigma_c^T \mathbf{\Lambda}_3 \sigma_c - 2\omega \sigma_c^T (\mathbf{K} \text{sign}(\sigma_c) - \mathbf{\Lambda}_1 \delta_L). \end{aligned} \quad (3.47)$$

Based on Assumption 3.1 and (3.40), the following relations yield:

$$-2\omega \sigma_c^T (\mathbf{K} \text{sign}(\sigma_c) - \mathbf{\Lambda}_1 \delta_L) \leq 0, \quad (3.48)$$

$$\begin{aligned} \sqrt{2}(\mathbf{\Lambda}_2 - \omega \mathbf{I})^{\frac{1}{2}} \sqrt{2\omega} \mathbf{\Lambda}_3^{\frac{1}{2}} \geq & |(\gamma \mathbf{I} - \omega \mathbf{\Lambda}_2 - \mathbf{\Lambda}_3)| + 2\boldsymbol{\Phi} \geq \left| \left((\gamma \mathbf{I} - \omega \mathbf{\Lambda}_2 - \mathbf{\Lambda}_3) - \right. \right. \\ & \left. \left. \left(\frac{\mathbf{K}}{|\sigma_c|} - \frac{\mathbf{\Lambda}_1 \delta_L}{|\sigma_c|} \right) \right). \end{aligned} \quad (3.49)$$

Comparing (3.48) and (3.49) with (3.47) yields:

$$\dot{V} < -2 \left((\Lambda_2 - \omega \mathbf{I})^{\frac{1}{2}} \dot{\sigma}_c + \sqrt{\omega} \Lambda_3^{\frac{1}{2}} \sigma_c \right)^T \left((\Lambda_2 - \omega \mathbf{I})^{\frac{1}{2}} \dot{\sigma}_c + \sqrt{\omega} \Lambda_3^{\frac{1}{2}} \sigma_c \right). \quad (3.50)$$

Accordingly, when $|\Phi^{-1}\sigma_c| \geq \mathbf{K}$, one has $\dot{V} < 0$. When $|\Phi^{-1}\sigma_c| < \mathbf{K}$, (3.42) is obtained as:

$$\ddot{\sigma}_c = -\Lambda_2 \dot{\sigma}_c - (\Lambda_3 + \Phi^{-1})\sigma_c + \Lambda_1 \delta_L. \quad (3.51)$$

Since Λ_1 to Λ_3 and Φ are constants, the relation above can be transformed to the frequency domain using Laplace transformation as follows:

$$\Sigma_c p^2 + \Lambda_2 \Sigma_c p + (\Lambda_3 + \Phi^{-1})\Sigma_c = \Lambda_1 \Delta_L, \quad (3.52)$$

where p is Laplace operator, $\Sigma_c = \mathcal{L}\{\sigma_c\}$ and $\Delta_L = \mathcal{L}\{\delta_L\}$, where $\mathcal{L}\{\star\}$ is Laplace function. Thus, the transfer function $T_1(p) = \Sigma_c \Delta_L^{-1}$ is obtained as:

$$\begin{aligned} T_1(p) &= \Sigma_c \Delta_L^{-1} = \Lambda_1 \left((p\mathbf{I} + \mathbf{R}_1)(p\mathbf{I} + \mathbf{R}_2) \right)^{-1}, \\ \mathbf{R}_1 &= \frac{1}{2} \left(-\Lambda_2 + \left(\Lambda_2^2 - 4(\Lambda_3 + \Phi^{-1}) \right)^{1/2} \right), \\ \mathbf{R}_2 &= \frac{1}{2} \left(-\Lambda_2 - \left(\Lambda_2^2 - 4(\Lambda_3 + \Phi^{-1}) \right)^{1/2} \right). \end{aligned} \quad (3.53)$$

Based on (3.40), (3.53) has real poles. Also, taking Laplace of the second row of (3.41) results in the following transfer function:

$$T_2(p) = \Sigma_c \Sigma^{-1} = (p\mathbf{I} + \Lambda_2)^{-1} \Lambda_1, \quad (3.54)$$

where $\Sigma = \mathcal{L}\{\sigma\}$. Based on (3.40), (3.53) and (3.54), $T_3(p) = \Sigma \Delta_L^{-1}$ can be obtained as follows:

$$T_3(p) = T_1(p) T_2^{-1}(p) = \Lambda_1 \left((p\mathbf{I} + \Lambda_2)(p\mathbf{I} + \mathbf{R}_1)(p\mathbf{I} + \mathbf{R}_2) \right)^{-1}. \quad (3.55)$$

Based on (3.40), the nominator's coefficients of $T_3(p)$ are positive and real (there is not nay imaginary roots). Hence, it is stable. So, it can be seen that the response has its maximum magnitude in zero frequency [42]. It means that the response is bounded as $|\sigma| < \delta_B$ where $\delta_B = T_3(0) = (\mathbf{R}_1)^{-1}(\mathbf{R}_2)^{-1}\Lambda_1(\Lambda_2)^{-1} = \Lambda_1^2(\Lambda_3 + \Phi^{-1})^{-1}\Lambda_2^{-1}$. Thus, FQMC is a Quasi SMC and the theorem is proved.

Remark 3.1. $T_2(p)$ in (3.54) is a low-pass filter that exists in the reaching law in (3.37). Thus, it filters out the existing noises in the orthogonal sliding manifold σ emanated from force sensor and camera measurement noises. Also, FQSMC does not exploit a discontinuous switching function in the control law, it is free of chattering.

Remark 3.2. Typically, in Quasi SMC, there is a trade-off between the tracking error and chattering. Hence, if the control gains are set to large values, chattering increases due to the existing noises in the sensors' feedback. If they are set to small values, the tracking error may increase. However, in FQSMC, the intrinsic filter smooths the signals and thus the controller gains can be set to larger values. Consequently, the tracking precision will increase without generating adverse chattering.

3.5 Experimental Results and Discussion

In this section, several experiments have been conducted to investigate the performance and feasibility of the proposed method. Note that two workpieces with planar and curved surfaces are provided for the tests. The constraint relations of the workpieces' surfaces are as follows:

$$\begin{aligned} \text{Planar: } f_S(x, y, z) &= z, \\ \text{Curved: } f_S(x, y, z) &= (z - 0.15)^2 + x^2 - 0.15^2. \end{aligned} \tag{3.56}$$

3.5.1 Result of Training the Neural Network

To train the NN, n_d is set to 1000 and 20% of the sampling data is considered for the validation test. The maximum number of iterations for training is set to 1000. Figure 3.5 shows the results of training the NN for the planar workpiece. The cost value for training data has converged to zero after twenty iterations which means the NN is trained well. Additionally, the cost value for validation data shows a consistent decrement which means the NN is not over-trained.

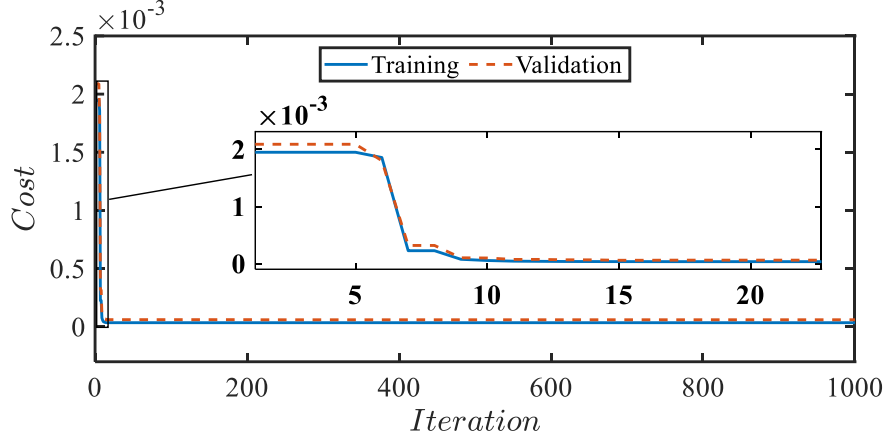


Figure 3.5: Training the NN.

3.5.2 Design of the Experimental Test

For the experiments, five experimental tests are designed. In the first four tests, the performance of the proposed MAPF-CGTSP method and switching between the free-motion and interacting with the workpiece, along with the proposed controller is investigated for the environments with obstacles. To this end, four operations labeled as Op.1, ..., Op.4 are considered with a different configuration of the number of tasks and the obstacle positions to analyze the performance and accuracy of the proposed task-sequence/path planning using MTOA in challenging situations. The environment configurations corresponding to each operation are depicted in the next subsection. The equations Obstacles and tasks of Op.1 to Op.4 are given in (3.57) to (3.60).

Task 1:	$\left\{ \begin{array}{l} \text{Type: 2} \\ P_{wd}(\vartheta) = \begin{bmatrix} 0.04\cos((\vartheta 1.6 - 0.3)\pi) \\ 0.02\sin((3.2\vartheta - 0.6)\pi) + .1 \\ 0 \end{bmatrix} \\ v_d = 0.001 \\ F_d(\vartheta) = 8 \end{array} \right\}, \text{Task 2: } \left\{ \begin{array}{l} \text{Type: 1} \\ P_{wd}(\vartheta) = \begin{bmatrix} .02 & .1 & 0 \end{bmatrix} \\ T_t = 50 \\ F_d(\vartheta) = 8 \end{array} \right.$	(3.57)
---------	---	--------

Task 3: $\begin{cases} \text{Type: 1} \\ P_{wd}(\vartheta) = [-.02 \quad .1 \quad 0]^T \\ T_t = 30 \\ F_d(\vartheta) = 8 \end{cases}$	Task 4: $\begin{cases} \text{Type: 2} \\ P_{wd}(\vartheta) = \begin{bmatrix} 0.08 \cos\left(\frac{1}{3}\vartheta\pi + \frac{\pi}{3}\right) \\ 0.08 \sin\left(\frac{1}{3}\vartheta\pi + \frac{\pi}{3}\right) + 0.1 \\ 0 \end{bmatrix} \\ v_d = 0.001 \\ F_d(\vartheta) = 8 \end{cases}$
---	--

$$\text{Task 1: } \begin{cases} \text{Type: 2} \\ P_{wd}(\vartheta) = \begin{bmatrix} 0.02\vartheta - .06 \\ 0.1 \\ 0 \end{bmatrix} \\ v_d = 0.0005 \\ F_d(\vartheta) = 8 \end{cases}, \text{Task 2: } \begin{cases} \text{Type: 1} \\ P_{wd}(\vartheta) = [0.07 \quad 0.12 \quad 0]^T \\ T_t = 30 \\ F_d(\vartheta) = 8 \end{cases}, \quad (3.58)$$

$$\text{Task 3: } \begin{cases} \text{Type: 2} \\ P_{wd}(\vartheta) = [0.07 \quad 0.14 \quad 0]^T \\ 0.01045 \\ v_d = 0.0005 \\ F_d(\vartheta) = 8 \end{cases},$$

$$\text{Task 1: } \begin{cases} \text{Type: 2} \\ P_{wd}(\vartheta) = \begin{bmatrix} 0.055 \\ 0.111 - .03\vartheta \\ -.01045 \end{bmatrix} \\ v_d = 0.0005 \\ F_d(\vartheta) = 8 \end{cases}, \text{Task 2: } \begin{cases} \text{Type: 1} \\ P_{wd}(\vartheta) = [-.055 \quad 0.111 \quad -.01045]^T \\ T_t = 30 \\ F_d(\vartheta) = 8 \end{cases}, \quad (3.59)$$

$$\text{Task 1: } \begin{cases} \text{Type: 2} \\ P_{wd}(\vartheta) = \begin{bmatrix} .02 \sin\left(\frac{1}{2}\vartheta\pi + \frac{\pi}{2}\right) + .03 \\ .02 \cos\left(\frac{1}{2}\vartheta\pi + \frac{\pi}{2}\right) + .125 \\ \left[(.15^2 - \left((.02 \sin\left(\frac{1}{2}\vartheta\pi + \frac{\pi}{2}\right) + .03 \right)^2)^{.5} - .15 \right] \end{bmatrix} \\ v_d = 0.001 \\ F_d(\vartheta) = 8 \end{cases}, \quad (3.60)$$

$$\text{Task 2: } \begin{cases} \text{Type: 1} \\ P_{wd}(\vartheta) = [-.055 \quad .111 \quad -0.01045]^T \\ T_t = 50 \\ F_d(\vartheta) = 8 \end{cases}.$$

The objective of the fifth test is to evaluate the performance of the proposed hybrid control method and compare the results with other aforementioned well-known schemes in terms of tracking error, convergence rate, control effort, and chattering level. An infinity-shaped path on the planar workpiece is defined as the desired path and a sinusoidal desired signal is defined as the desired interaction force as:

$$P_d(t) = [0.05 \cos(0.025t) + 0.02 \quad 0.025\sin(0.05t) \quad 0 \quad 0 \quad 0]^T, F_d(t) = 1.5 \sin(0.15t) + 6. \quad (3.61)$$

3.5.3 Results and Discussion of the Experimental Tests

3.5.3.1 Hybrid Task Sequence/Path Planning (Tests 1 to 4)

In these tests, a set of four operations is presented. The performance of the proposed optimal task sequence/path planning method using the MAPF strategy is compared to that of the traditional APF. Furthermore, a comparative study of solving the MAPF-CGTSP by the mix-integer MTOA against the PSO, GWO, membrane-inspired evolutionary algorithm (memE) is presented to compare the performance of the proposed optimization algorithm. Please note that the parameters of the optimization algorithms are set in a way that their overall populations are almost 10, 20, 20, and 20 for Op. 1 to Op.4, respectively.

As mentioned before, this problem is composed of two various problems including finding the optimal task sequence and also the parameters of the proposed MAPF method to have an optimal collision-free path between the tasks. In the first row of Table 3.1, the result of solving the task sequence part of the optimization problem for each operation, using the MTOA, and the direction

of Type 2 tasks is listed in two different subsets. For each case, MTOA is executed thirty times (30 independent runs) to reach the solution. The first subset defines the sequence of the tasks for each operation and the second subset shows the direction of entering to a Type 2 task and exiting from it. Note that, in the second subset, 0 is corresponding to the endpoint A for a Type 2 task and 1 is corresponding to the endpoint B. The other parameters listed in Table 3.1 are obtained by MTOA for the MAPF to reach an optimized collision-free path between the tasks while the sequence of the starting and ending points of each path has already been obtained.

Table 3.1: The optimized parameters for MAPF-CGTSP using MTOA.

Optimization Parameters	Op. 1	Op. 2	Op. 3	Op. 4
Task seq.	{2 1 3 4} {01}	{2 3 1} {1}	{1 2} {0}	{1 2} {0}
k_a	N/A	0.8234	0.2079	0.4241
k_r	N/A	0.3735	0.9341	0.0603
α_p	N/A	0.7738	0.4106	0.7269
α_{rot}	N/A	0.000002638	0.00000941	0
ρ_0	N/A	0.5163	0.3707	0.9486
k_{r_1}	N/A	0.008908	0.1567	0.8594
α_{p_1}	N/A	0.9204	0.5168	0.002304
α_{rot_1}	N/A	0.3504	0.00001312	0.4614
ρ_{0_1}	N/A	0.9654	0.8814	0.3977
k_{r_2}	N/A	0.2847	N/A	0.4181
α_{p_2}	N/A	0.5363	N/A	0.8311
α_{rot_2}	N/A	0.000008907	N/A	0.5818
ρ_{0_2}	N/A	0.3105	N/A	0.01136

Based on this table, in the first operation, four different tasks, two Type 2 tasks and two Type 1 tasks, are defined on a planar workpiece. Based on the optimal task sequences of the first operation, it can be observed that this operation starts with the second task (T2) which is a Type 1 task or a point and moves towards the first task (T1) which is a Type 2 task or a path. The direction of Type 2 tasks affects achieving an optimal general path for the operations. Based on the obtained direction for the Type 2 tasks in this table, the first Type 2 task (T1) starts from the end-point A (T1A) and exits from the endpoint B (T1B). Then, the robot moves to

the third task (T3) which is the other Type 1 task. Finally, the robot moves towards the last one which is the fourth task (T4). This task is also a Type 2 task with two endpoints which based on the second element of the second subset, the robot will enter from its endpoint B (T4B). The desired tasks and the paths between each two tasks are depicted in Figure 3.6. From this figure, it can be seen that the first operation is free of obstacles. Therefore, the path between the tasks can be considered as a straight line. Hence, this operation does not require to use MAPF for obtaining the path between the tasks. The robot carrying out the tasks for the first operation is shown in Figure 3.7. The results of the vision and force control system in performing the first operation are presented in Figure 3.8a and b. According to Figure 3.8a, which shows the trajectory tracking of Op. 1 on the image plane, it can be seen that the robot tracks the two paths and regulates on each point of the tasks one-by-one until the entire operation is done. Referring to Figure 3.8b, the effectiveness of the force control process for each task and also the feasibility of the proposed method for switching between the free motion and interaction with the workpiece is demonstrated.

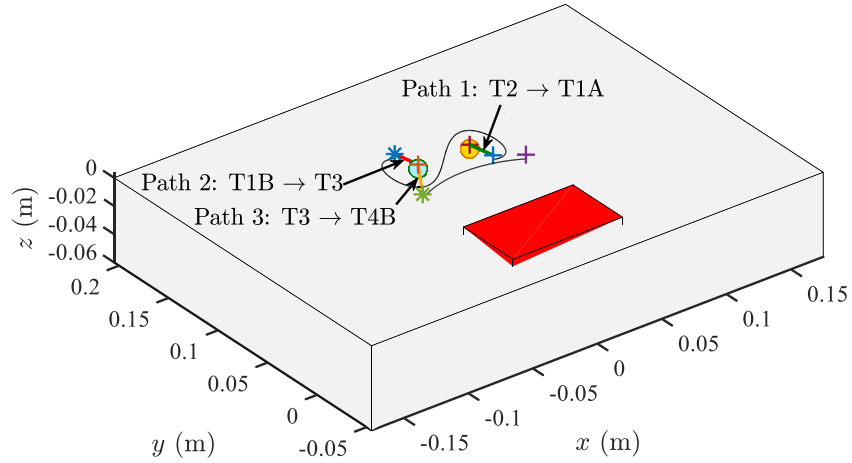


Figure 3.6: Op. 1-Desired paths and points of four tasks on the workpiece

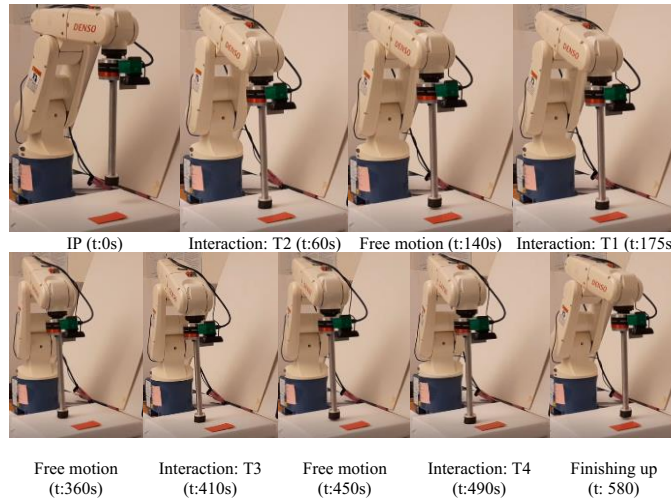


Figure 3.7: The robot operating Op. 1.

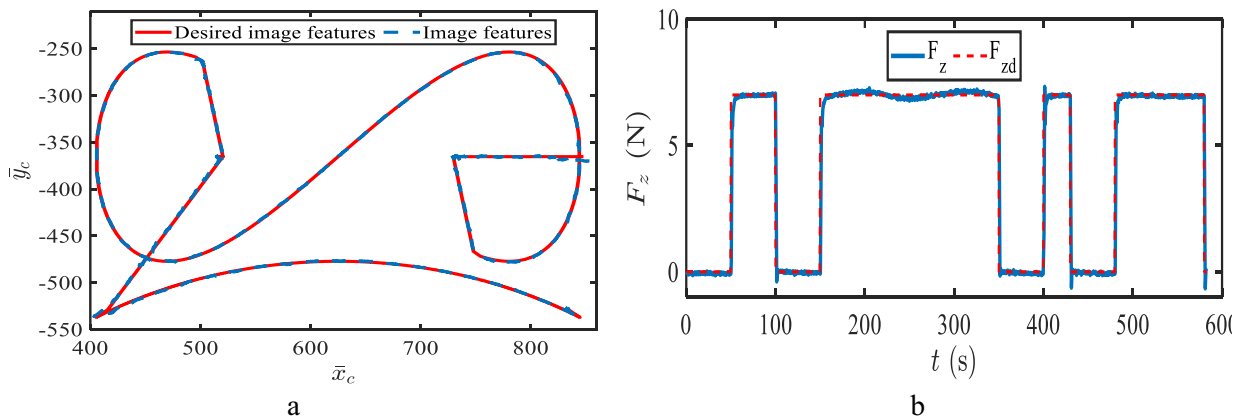


Figure 3.8: Path tracking in the image space and force control of all the tasks of OP. 1: a) Tracking the paths and points in the image space of Op. 1, b) Controlling the force of Op. 1.

In the second operation, three different tasks, a Type 2 task and two Type 1 tasks, are defined on a planar workpiece. Based on the optimal task sequences of the second operation, the robot

performs the whole operation. The desired tasks and the paths between each two tasks which are obtained by APF and MAPF methods are depicted in Figure 3.9a and b, respectively. From these figures, it can be observed that two obstacles are placed between three defined tasks. In Figure 3.9a, using the APF method, the robot moves from the NAEP towards the AEP of the first task sequence selected by MTOA (T2) through Path 1. Then, using APF method, the robot moves from T2 to T3 (the second task sequence selected by MTOA) through Path 2 which is depicted in Figure 3.9a. However, the APF method does not work properly in reaching the third task sequence (T1). Hence, the robot will be trapped and could not continue its trajectory to reach the target. Figure 3.9b shows that when using the MAPF method, the robot successfully reaches the target. So, the proposed method outperforms the traditional APF method, since it gives a minimum collision-free traveled distance in performing this multi-task operation in presence of obstacles. The robot carrying out the tasks for the second operation using MAPF is shown in Figure 3.10. The results of the vision and force control system in performing the second operation are presented in Figure 3.11a and b. According to Figure 3.11a, which shows the trajectory tracking of Op. 2 on the image plane, it can be seen that the robot tracks the defined path and regulates on each point of the tasks one-by-one until the entire operation is done. Referring to Figure 3.11b, the effectiveness of the force control process for each task and also the feasibility of the proposed method for switching between the free motion and interaction with the workpiece is demonstrated.

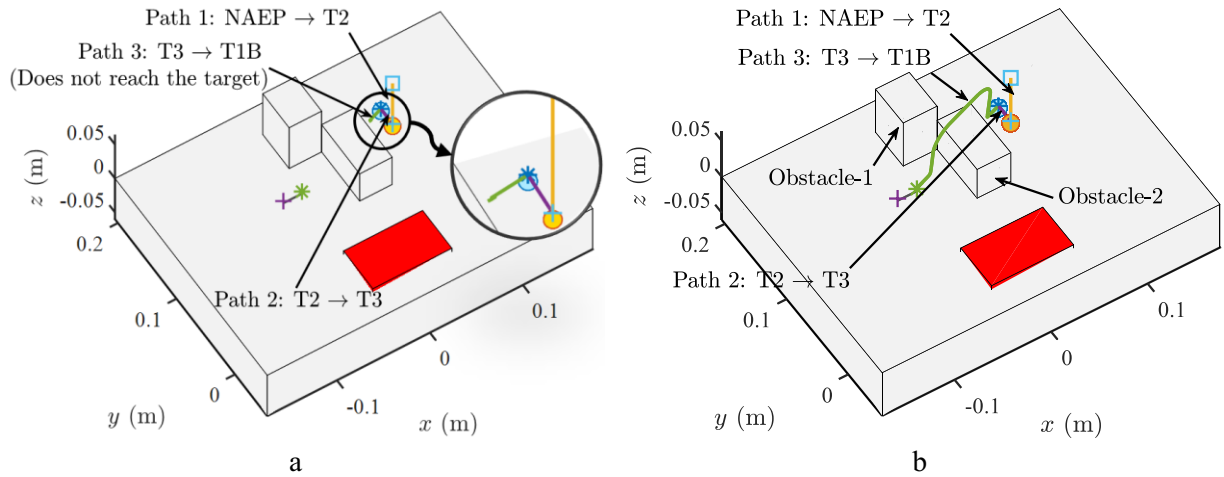


Figure 3.9: Op. 2: a) Desired paths and points of three tasks on the workpiece using APF method, b) Desired paths and points of three tasks on the workpiece using MAPF method.

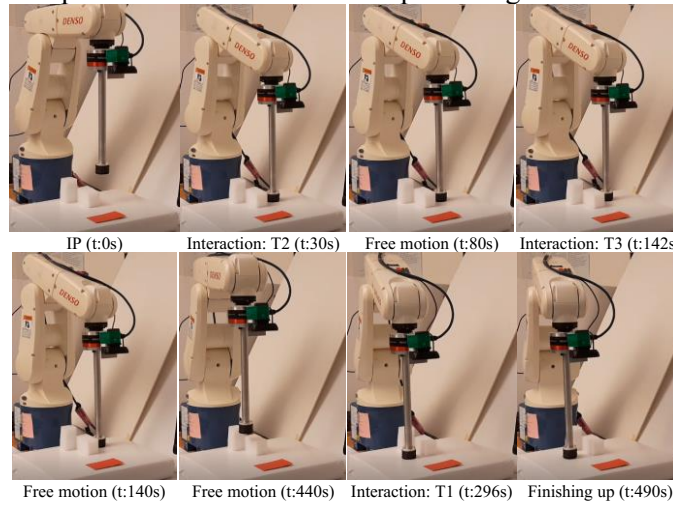


Figure 3.10: The robot operating Op. 2.

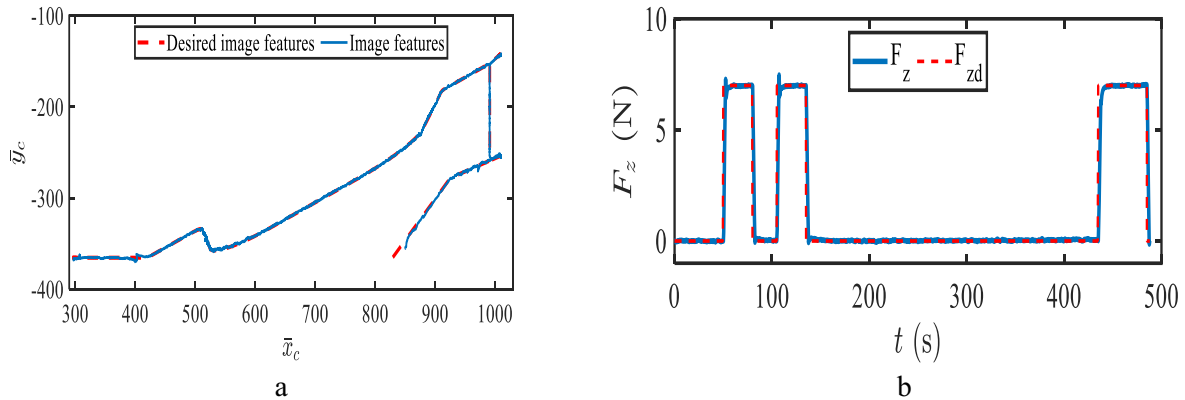


Figure 3.11: Path tracking in the image space and force control of all the tasks of OP. 2: a) Tracking the paths and points in the image space of Op. 2, b) Controlling the force of Op. 2.

In the third operation, two different tasks, a Type 2 task and two Type 1 tasks, are defined on a curved workpiece to show the effectiveness of the proposed method in performing the multi-task operation on more complicated workpieces. Based on the optimal task sequences of the third operation, the robot performs the whole operation. The desired tasks and the paths between each two tasks which are obtained by APF and MAPF methods are depicted in Figure 3.14. From these figures, it can be observed that one obstacle is placed between two defined tasks. In Figure 3.14a, using the APF method, the robot moves from the NAEP towards the AEP of the first task sequence selected by MTOA (T1) through Path 1. After completing T1, the robot is required to move towards the other task (T2) from the other endpoint of the first task (T1B).

However, the APF method does not work properly in reaching T2. Hence, the robot will be trapped and could not continue its trajectory to reach the target. Figure 3.14b shows that when using the MAPF method, the robot successfully reached the target. So, the proposed method outperforms the traditional APF method, since it gives a minimum collision-free traveled distance in performing this multi-task operation in presence of obstacles. The robot carrying out the tasks for the third operation is shown in Figure 3.12. The results of the vision and force control system in performing the third operation are presented in Figure 3.13. According to Figure 3.13a, which shows the trajectory tracking of Op. 3 on the image plane, it can be seen that the robot tracks the defined path and regulates the desired point of the task until the entire operation is done. Referring to Figure 3.13b, the effectiveness of the force control process for each task and also the feasibility of the proposed method for switching between the free motion and interaction with the workpiece is demonstrated.

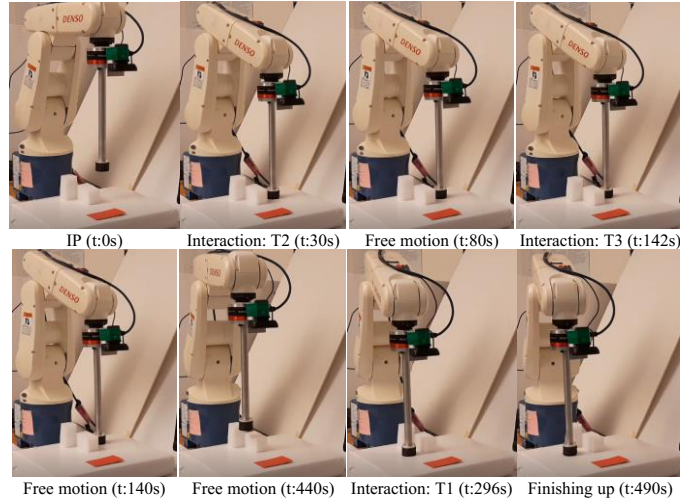


Figure 3.12: The robot operating Op. 3.

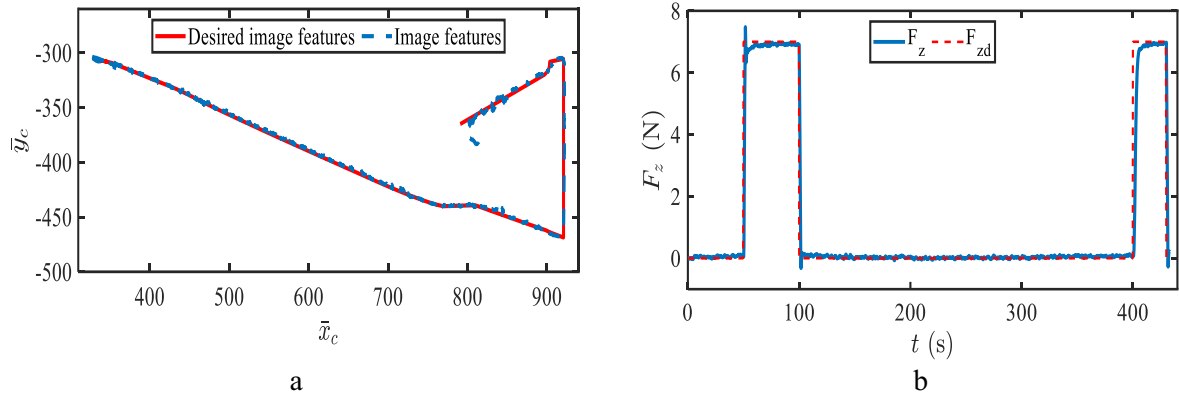


Figure 3.13: Path tracking in the image space and force control of all the tasks of OP. 3, a) Tracking the paths and points in the image space of Op. 3, b) Controlling the force of Op. 3.

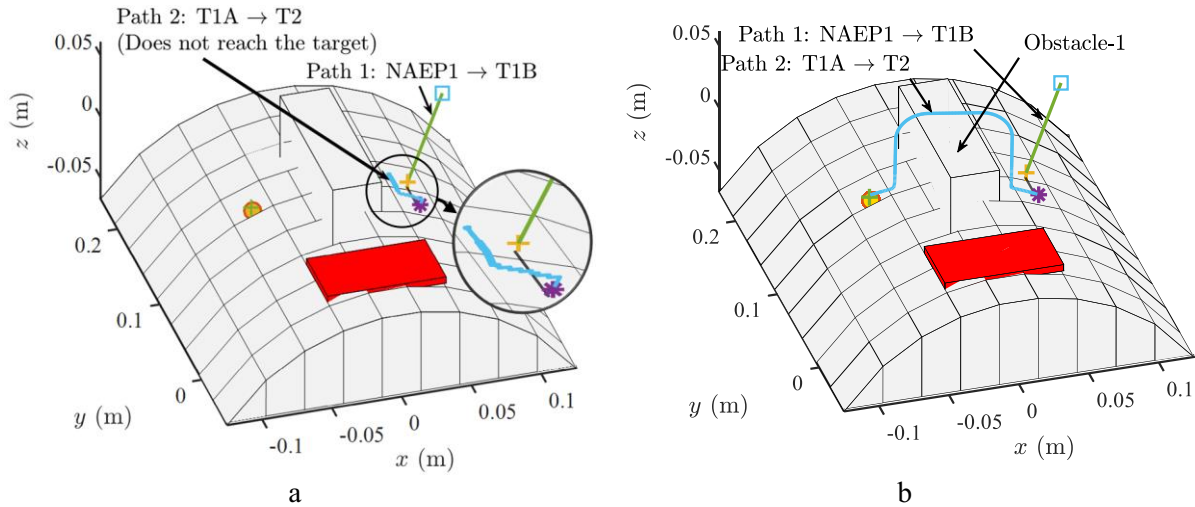


Figure 3.14: Op. 3 (a) Desired paths and points of three tasks on the workpiece using APF method, b) Desired paths and points of three tasks on the workpiece using MAPF method.

The fourth operation is also accomplished on a curved surface with a different obstacle configuration. Two different tasks are defined for this operation. The results obtained in Figure 3.15a and b, show that the APF method cannot finish the operation successfully. However, using the MAPF method, the operation is performed properly. The robot carrying out the tasks for the fourth operation is shown in Figure 3.16.

The results of the control process for the intended tasks are presented in Figure 3.17. According to Figure 3.17a, the robot has tracked the desired features for each task when interacting with the workpiece and between the tasks by free-motion properly to complete the operation. Referring to Figure 3.17b, it can be seen that the interacting force is controlled properly as well. These results show not only the effectiveness of the proposed path/task sequence planning, but also the feasibility of the proposed hybrid control method for different workpieces.

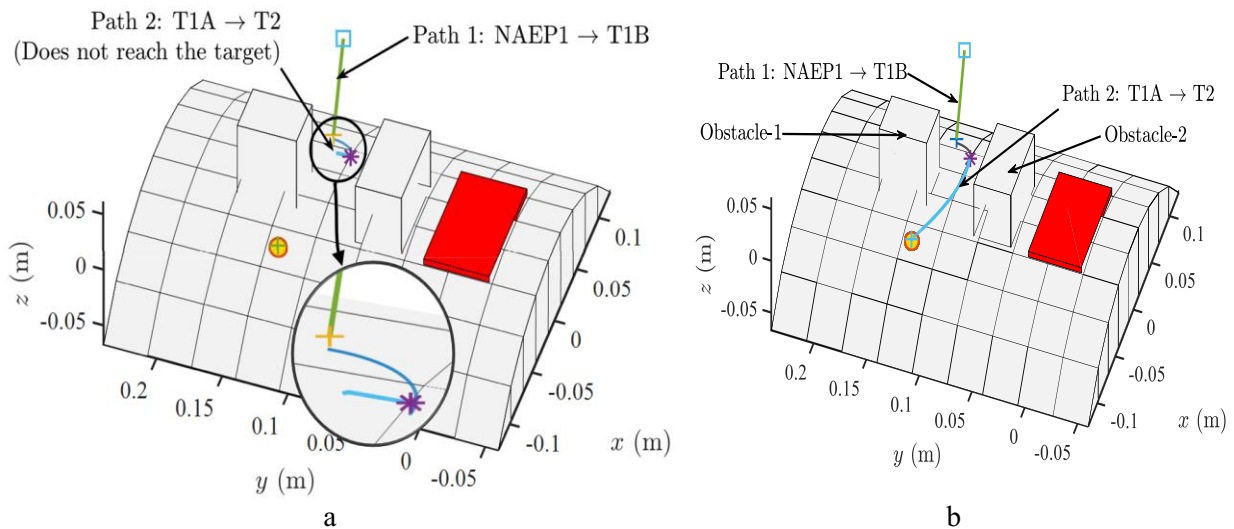


Figure 3.15: Op. 4: a) Desired paths and points of two tasks on the workpiece using APF method, b) Desired paths and points of three tasks on the workpiece using MAPF method.

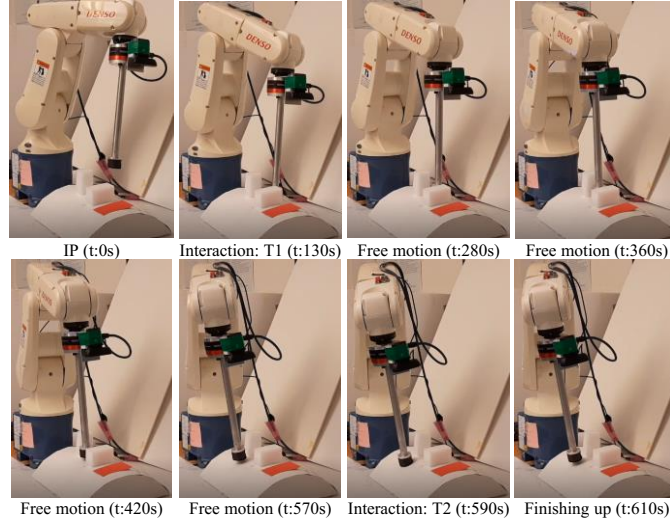


Figure 3.16: The robot operating Op. 4.

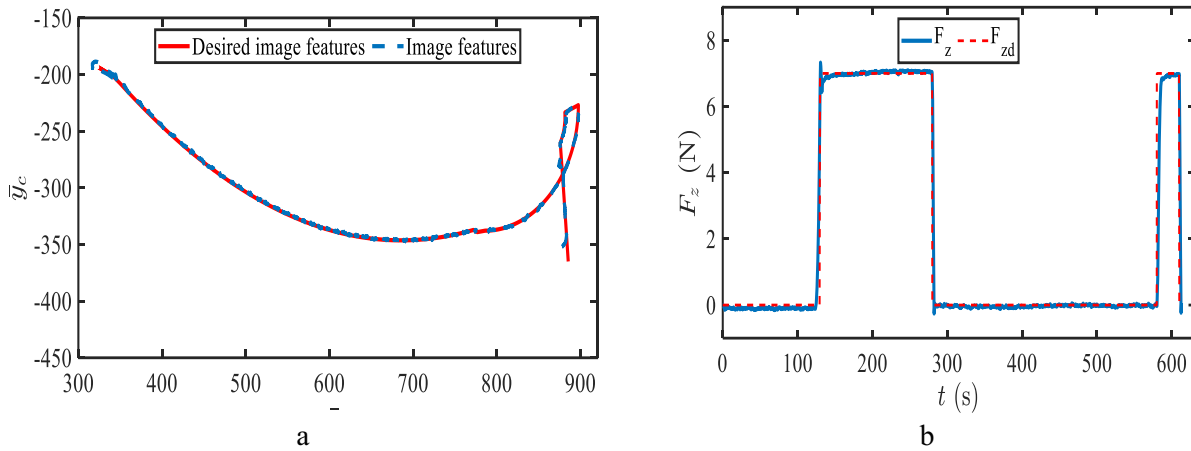


Figure 3.17: Path tracking in the image space and force control of all the tasks of OP. 4: a) Tracking the paths and points in the image space of Op. 4, b) Controlling the force of Op. 4.

Each test was independently executed 30 times for each operation. The results provided in Table 3.2, show the arithmetic best, mean, worst, and standard deviation of the path length in the image plane for the 30 individual tests on each operation. From this table, it can be concluded that the MTOA method outperforms the other optimization algorithms. The best path obtained using the MTOA for the first operation is the same as the other methods, since the environment is free of obstacles which leads to a simple CGTSP problem. Therefore, in this operation, the optimization problem converts to a simple problem of finding the integer sequence of the tasks which is obvious that all provided algorithms have successfully reached the desired sequence to minimize the path

length. For the other operations, it can be observed that the MTOA method overcomes the drawback of PSO and GWO which are easy to be trapped into local optimum on average. The result also tells that MTOA has a better performance than memE in dealing with environments with obstacles.

Table 3.2: Results of the different optimization algorithms for all operations expressed in meters (m).

Operation	Statistics	PSO	GWO	memE	MTOA
Op. 1	Best	0.4803	0.4803	0.4803	0.4803
	Mean	0.5415	0.4843	0.4803	0.4803
	Worst	0.7406	0.5492	0.4803	0.4803
	Std.	0.07183	0.01533	0	0
Op. 2	Best	1.1909	1.1733	1.172	1.169
	Mean	20176.93	11000.733	1.2107	1.2015
	Worst	73333.70	36667.033	1.4710	1.396
	Std.	22182.96	17238.83	0.07289	00.05903
Op. 3	Best	1.175	1.172	1.171	1.167
	Mean	1834.8	1.174	1.175	1.172
	Worst	36667.03	1.213	1.209	1.201
	Std.	8198.66	0.01155	0.01068	9.9476e-3
Op. 4	Best	0.6985	0.6974	0.6948	0.6937
	Mean	5501.1	3667.76	0.6959	0.6941
	Worst	36667.03	36666.6	0.6974	0.6974
	Std.	13432.1	11285.26	0.014751	1.1282e-03

Figure 3.18 provides a graphical summary of the improvement percentage of the task sequence/path planning results in terms of path length for the methods GWO, MemE, and MTOA compared to the PSO. The result in this figure shows that solving the MAPF-CGTSP using MTOA method provides the highest improvement percentage compared to the other methods.

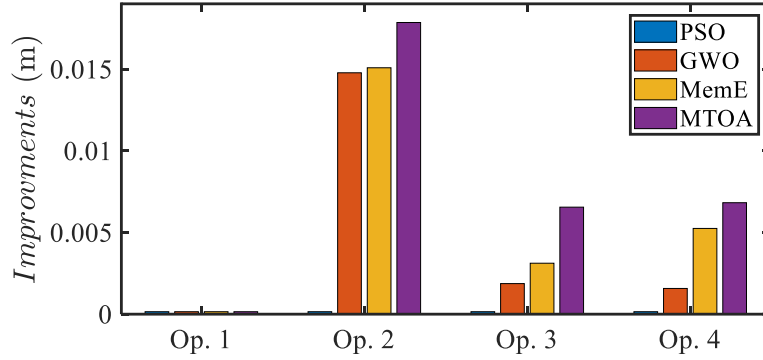


Figure 3.18:Op. 1-Desired paths and points of four tasks on the workpiece

3.5.3.2 Test 5: COMPARISON OF THE PERFORMANCE OF THE PROPOSED HYBRID CONTROLLER TO OTHER WELL-KNOWN METHODS

Using NN_{sd} in (3.20), the desired image feature signal of the second test (Figure 3.19a) can be extracted as illustrated in Figure 3.19b. The results of tracking the image feature and interaction force and joint velocities are demonstrated in Figure 3.20-Figure 3.22, respectively. In Figure 3.20, the FQSMC tracks the desired image feature signals with higher precision, lower chattering, oscillation, and faster convergence speed compared with SMC and even P/PI. SMC tracks the signals with higher precision relative to P/PI. However, the chattering level of the P/PI is much lower. Figure 3.21 shows the superiority of the FQSMC to P/PI and SMC in terms of chattering level, tracking precision, and convergence speed. The chattering issue is highlighted in the controller output, i.e., joint velocities, presented in Figure 3.22. SMC suffers from a high level of chattering, while the P/PI produces less chattering, and FQSMC's output is rather smooth. Note that, for SMC, the chattering is emanated from the switching function in the control law and the existing noise of the sensors' feedbacks. Whereas the chattering in the P/PI's output is only due to the noises. The reason is the level of chattering in P/PI is lower compared with that in SMC. FQSMC, on the other hand, has an intrinsic filter and does not employ any switching function in its control law. Consequently, it generates a smooth control command. In addition to the plots, several numerical indicators such as integral absolute error (IAE), integral time absolute error

(ITAE), standard deviation (STD), and root mean square error (RMSE) indicators are selected for quantitative comparison in terms of vision and force errors [56]. On the other hand, STD and integral square controller output (ISCO) indicators are evaluated for the joint velocities (controller output). These indicators are computed for the third test and tabulated in Table 3.4 and Table 3.3. Note that since the dimension of the vision and joint velocity results is higher than one (it is six), the weighted norms of the vision and joint velocity are used to compute those indicators. Referring to Table 3.3, for the vision control, FQSMC has decreased the values of IAE, ITAE, STD, and RMSE by 51.29%, 40.79%, 69.09%, and 66.96% compared to SMC, respectively. Compared to P/PI, these values are over 68.10%, 81.23%, 88.67%, and 93.67%. For the force control, FQSMC has decreased the values of IAE, ITAE, STD, and RMSE by 59.91%, 58.41%, 39.44%, and 40.58% compared to SMC, respectively. Compared to P/PI, these values are over 68.43%, 71.36%, 30.88%, and 32.45%. The results show that the proposed hybrid controller results in improvement of the control performance in terms of chattering, precision, and convergence rate to a significant extent.

Furthermore, according to

Table 3.4, the values of STD and ISCO for FSMC are 81.1% and 73.19% lower in comparison with SMC, and 69.85% and 45.02% lower than those of the P/PI. These results show that FQSMC outperforms both SMC and P/PI in terms of chattering level and control effort.

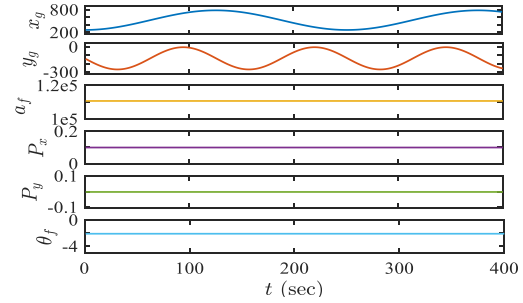
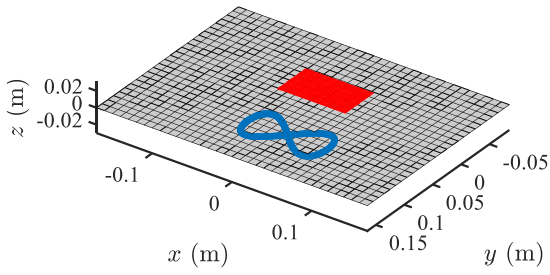


Figure 3.19: Test 5: a) Desired path on the workpiece, b) Corresponding feature.

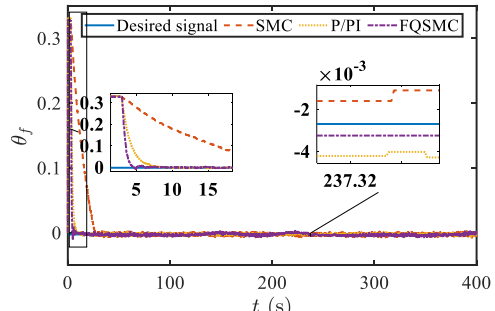
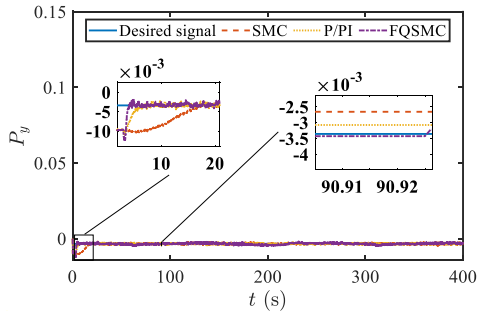
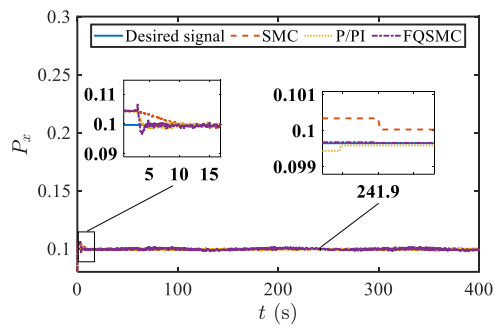
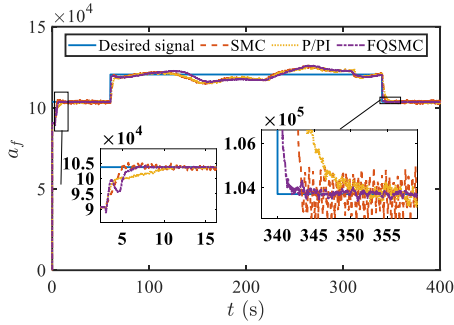
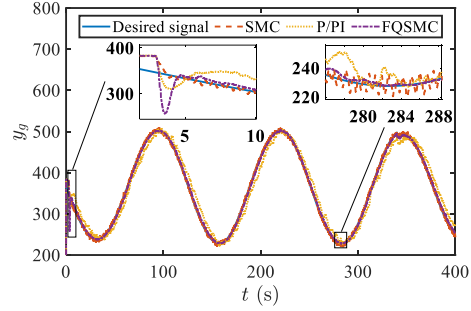
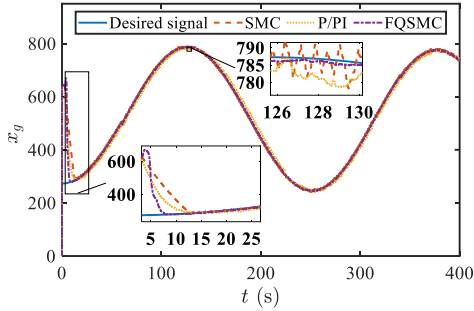


Figure 3.20: Tracking image features of the third test: a) \bar{x} , b) \bar{y} , c) a_f , d) S_x , e) S_y f) θ_f .

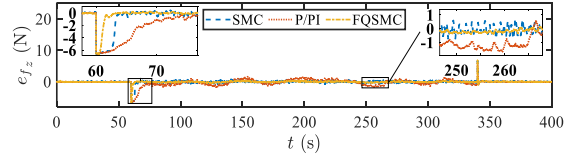
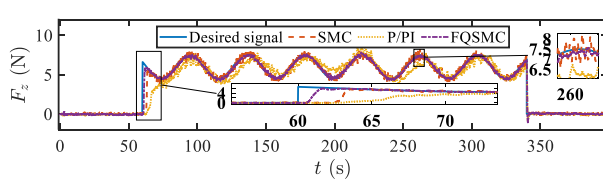


Figure 3.21: Force control of the third test.

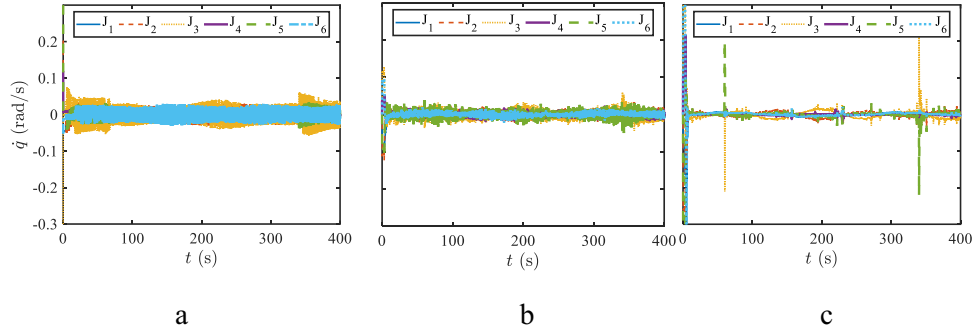


Figure 3.22: Robot joint velocities (test 3): a) SMC, b) P/PI, c) FQSMC.

Table 3.3: The computed values of the indicators for the norms of system errors of the third test.

	Comp.	Indicator			
		IAE	ITAE	STD	RMSE
Vision	P	0.2069	39.0753	0.0003	0.0006
	SMC	0.1355	12.386	1.10e-4	1.15e-4
	FQSMC	0.0660	7.334	3.4e-5	3.8e-5
Force	PI	201.85	36239.4	0.7643	0.7898
	SMC	158.95	24956.4	0.8724	0.8979
	FQSMC	63.731	10379.4	0.5283	0.5335

Table 3.4: The computed values of the indicators for the controller output of the third test.

Indicator	Compensator		
	P/PI	SMC	FQSMC
STD	0.018499	0.029509	0.005577
ISCO	0.700458	1.436190	0.385108

3.6 Summary

In this chapter, a novel image-based task-sequence/path planning method (MAPF-CGTSP) along with a robust vision and force control method is presented for industrial robots to perform

multi-task operations while interacting with a workpiece. The proposed MAPF-CGTSP algorithm combines a novel modified artificial potential field and a constrained generalized traveling salesman problem to achieve an optimal sequence of performing the tasks while generating a feasible and safe path between tasks for a multi-task operation. A mix-integer MTOA is developed to solve the proposed MAPF-CGTSP problem to achieve the integer sequence of performing the tasks and the continuous parameters of the MAPF method. Different test scenarios are employed to evaluate the MAPF-CGTSP algorithm combined with the vision and force control method. The results obtained in the different environments demonstrate that the proposed method can perform the multi-task operations using vision and force control method in different environments which makes it a suitable algorithm to be employed in industrial applications dealing with complex and real scenarios. The experimental results demonstrate that the MTOA algorithm yields better solutions in all the test environments compared to the other optimization methods. Also, the path planning results of the MAPF method are improved compared to the traditional APF. Another advantage of the proposed method is developing the FQSMC for vision and force control of industrial robots exploiting an intrinsic low-pass filter which leads to filtering out the measurement noises associated with the camera and force sensor. Also, the proposed controller results in Quasi-motion and elimination of chattering compared to the other provided methods which make it reliable in real-world scenarios. The experimental results show the benefits of the proposed MAPF-CGTSP algorithm for task sequence/path planning combined with the vision and force control in multi-task operations. The performance of the proposed MAPF-CGTSP method has been assessed in the first test using the test environments composed of different configurations and several obstacles. Also, the performance of the proposed vision and force control approach is compared with those of the other control methods to show its effectiveness. The results show the

effectiveness of the proposed MAPF-CGTSP method in terms of collision avoidance and provide a safe and feasible path compared to the other methods. Also, the superiority of the proposed vision and force method to other well-known methods is evaluated in terms of precision, convergence rate, robustness, control effort, and chattering.

CHAPTER 4 **Multi-Stage Vision and Force Control**

4.1 Introduction

As it was discussed in the last sections, for EIH configuration, there is still a lack of research work on a stable fast response method of vision and force to be used in industrial applications with the capability to deal with uncertainties. To address this issue, a new robust hybrid multi-stage vision and force control approach for industrial robots is proposed.

In this method, the vision and force control is carried out in three sequential stages: in the first stage, the orientation of the tool is controlled. When the angular errors of the tool reach the determined desired values, the control process is switched to the second stage, in which the position of the tool in xy -plane is controlled. Once the second stage is accomplished, the third stage will begin. This stage is divided into two substages: before and after contact with the workpiece. In the first substage, the image features are controlled in all six degrees-of-freedom (DOF). Since the orientation and the position of the end-effector in xy -plane are previously controlled, the tool moves in a normal direction towards the workpiece until it touches the surface and the second substage initiates. In this substage, the hybrid controller is activated to control the force and vision corresponding to the position of the tool on the surface, simultaneously. With this multi-stage strategy, the tool is perpendicular to the surface when it touches the surface. Besides, it improves the performance of the overall control process in terms of, precision, singularity avoidance, and stability [79], [80]. Additionally, super-twisting sliding mode controller (STSMC) is employed for vision and force control in each stage. This method can handle the uncertainties

of the system. Also, using this method, the chattering issue of the standard SMCs, is reduced without affecting the tracking accuracy and robustness [56]. The stability proof of the proposed controller has been provided by using Lyapunov theorem. A variable gain sliding surface is also designed to improve the performance of the traditional switch IBVS [79], [80].

4.2 Multi-Stage Vision and Force Control Design

Inspired by the switch IBVS method in [79], a multi-stage switching strategy is proposed to design the hybrid vision and force control for industrial robots. Applying this method leads the end-effector to the desired pose, perpendicular to the surface and in a desired position on the workpiece, before touching the surface. To design the proposed method, first, the vision motion is decomposed into several movements in different degrees of freedom which are utilized in each control stage.

4.2.1 Vision Motion Decomposition

To design the proposed multi-stage strategy, the vision motion of (2.11) is decomposed into three movements corresponding to a) pure rotational movement of the camera, b) pure linear movement of the camera on the xy -plane, and c) constrained movement of the camera in all DOFs except the z direction. The decomposed vision motion is obtained as:

$$\omega = \mathbf{J}_{sa}\dot{S} + \delta_a, v_{xy} = \mathbf{J}_{sxy}\dot{S} + \delta_{xy}, v_{xya} = \mathbf{J}_{sxya}\dot{S} + \delta_{xya}, \quad (4.1)$$

where $v_{xy} = [v_x \ v_y]^T$ and $v_{xya} = [v_{xy}^T \ \omega^T]^T$, $\mathbf{J}_{sa} \in \mathbb{R}^{3 \times 8}$, $\mathbf{J}_{sxy} \in \mathbb{R}^{2 \times 8}$ are interaction matrix which map the image features' velocities in image space to angular velocities and linear velocities on the xy -plane in the Cartesian space, respectively, $\mathbf{J}_{sxya} = [\mathbf{J}_{sxy}^T \ \mathbf{J}_{sa}^T]^T$ is the interaction matrix which maps the image features' velocities in the image space to the angular and linear velocities in all DOFs in Cartesian space except the z direction. These interaction matrices are derived as:

$$[\mathbf{J}_{sxy}^T \quad \mathbf{J}_{sz}^T \quad \mathbf{J}_{sa}^T]^T = \mathbf{J}_s = \mathbf{L}_s^+, \quad (4.2)$$

where operator $(\star)^+$ denotes the pseudo-inverse of the non-square matrix \star [19], $\mathbf{J}_{sz}^T \in \mathbb{R}^{1 \times 8}$ is the Jacobian matrix which maps the image features' velocities to the camera's linear velocity in z direction. In (4.1), $\delta_a \in \mathbb{R}^3$, $\delta_{xy} \in \mathbb{R}^2$, and $\delta_{axy} = [\delta_{xy} \quad \delta_a]^T$ are the uncertainties which can be obtained as:

$$[\delta_{xy}^T \quad \delta_z \quad \delta_a^T]^T = -\mathbf{L}_s^+ \delta_s V, \quad (4.3)$$

where $\delta_z \in \mathbb{R}$ is the uncertainty in the z direction. Based on (4.1), the pose error in Cartesian space corresponding to the image feature error in the image space can be defined as:

$$e_p = \mathbf{J}_s e_s, \quad e_a = \mathbf{J}_{sa} e_s, \quad e_{xy} = \mathbf{J}_{sxy} e_s, \quad e_{xya} = [e_{xy}^T \quad e_a^T]^T = \mathbf{J}_{sxya} e_s, \quad (4.4)$$

where e_p , e_{xy} , and e_{axy} are pose errors in all six DOFs, in xy -plane, and in all DOFs except z direction, respectively, e_a is the orientation error of camera in Cartesian space, e_s is the vector of image feature error in the image space defined as:

$$e_s = S - S_d, \quad (4.5)$$

where $S_d \in \mathbb{R}^8$ is the vector of desired image features.

4.2.2 Stages of the Proposed Method

The multi-stage switching strategy is determined as follows:

Stage 1. In the first stage, the orientation of the camera is controlled so that $\lim_{t \rightarrow +\infty} e_a = 0$. Note that orientation of the camera corresponding to S_d must be normal to the surface of the workpiece (Figure 4.1a). Based on (4.4), taking time derivative of e_a , yields:

$$\dot{e}_a = \dot{\mathbf{J}}_{sa} e_s + \mathbf{J}_{sa} \left((\mathbf{L}_s + \delta_s) V - \dot{S}_d \right). \quad (4.6)$$

The input of the industrial robots is the vector of joint velocities $u = \dot{q} \in \mathbb{R}^6$ which satisfies the following kinematic relations:

$$V = (\mathbf{J}_q + \boldsymbol{\delta}_q)u, \quad (4.7)$$

where, $\mathbf{J}_q, \boldsymbol{\delta}_q \in \mathbb{R}^{6 \times 6}$ are the robot Jacobian and its uncertain part, respectively [20]. Substituting (4.7) into (4.6) yields:

$$\dot{e}_a = \mathbf{J}_{sa}e_s + \mathbf{J}_{sa} \left((\mathbf{L}_s + \boldsymbol{\delta}_s)(\mathbf{J}_q + \boldsymbol{\delta}_q)u - \dot{S}_d \right). \quad (4.8)$$

Since the desired image features are fixed, then $\dot{S}_d = 0$. Accordingly, (4.6) can be simplified as:

$$\dot{e}_a = \mathbf{J}_{sa}\mathbf{L}_s\mathbf{J}_qu + \delta_{La}, \quad (4.9)$$

where $\delta_{La} = \mathbf{J}_{sa}(\mathbf{L}_s\boldsymbol{\delta}_q + \boldsymbol{\delta}_s\mathbf{J}_q + \boldsymbol{\delta}_s\boldsymbol{\delta}_q)u + \mathbf{J}_{sa}e_s$. The system input is defined as $u = u_1$ where u_1 is the controller output in Stage-1 which is obtained utilizing STSMC, the procedure of which will be discussed in the next section.

Stage 2. In the second stage, the end-effector's position in the xy -plane is controlled to reduce the tracking error in xy -plane, i.e., $\lim_{t \rightarrow +\infty} e_{xy} = 0$, (Figure 4.1b). To this end, the same procedure as Stage-1 is performed which eventually leads to the following relation:

$$\dot{e}_{xy} = \mathbf{J}_{sxy}\mathbf{L}_s\mathbf{J}_qu + \delta_{Lxy}, \quad (4.10)$$

where $\delta_{Lxy} = \mathbf{J}_{sxy}(\mathbf{L}_s\boldsymbol{\delta}_q + \boldsymbol{\delta}_s\mathbf{J}_q + \boldsymbol{\delta}_s\boldsymbol{\delta}_q)u + \mathbf{J}_{sxy}e_s$. Like Stage 1, in (4.10), $u = u_2$ where u_2 is the obtained controller output utilizing STSMC.

Stage 3. This stage comprises two substages: moving the tool in z -direction towards the surface before touching the surface, and after touching the surface and starting the interaction.

In the first substage, the feature errors corresponding to the pose error in all six DOFs are controlled, i.e., $\lim_{t \rightarrow +\infty} e_p = 0$. However, since the orientation and position of the robot are previously controlled in the preceding stages, the tool tip starts moving in z direction (Figure 4.1c).

Performing the same procedure as in the previous stages, the following relation yields:

$$\dot{e}_P = \mathbf{J}_q u + \delta_{Lq}, \quad (4.11)$$

where $\delta_{Lq} = \boldsymbol{\delta}_q u + \mathbf{L}_s^+ (\boldsymbol{\delta}_s \mathbf{J}_q + \boldsymbol{\delta}_s \boldsymbol{\delta}_q) + \frac{d(\mathbf{L}_s^+)}{dt} e_s$ and $u = u_{31}$ where u_{31} is the controller output in Stage-3-Substage-1 obtained using STSMC.

The second substage begins once the end-effector touches the surface of the workpiece. Thus, in addition to the vision control, the normal exerted force to the tool must be controlled, i.e., a hybrid vision and force control. To this end, the vision system controls all corresponding DOFs of the camera except the z direction in Cartesian space. Also, the exerted force in z direction is controlled independently and simultaneously (Figure 4.1d). i.e., $\lim_{t \rightarrow +\infty} e_{axy} = 0$ and $\lim_{t \rightarrow +\infty} e_F = 0$ where e_F is the force error in z direction defined as $e_F = F - F_d$ and F_d is the desired force reference. To this end, an orthogonal manifold e_{PF} is defined as follows:

$$e_{PF} = (\mathbf{I} - H^T H) e_{axy} + H e_F, \quad (4.12)$$

where $H = [0 \ 0 \ 0 \ 0 \ 0 \ 1]$. Thus, due to the orthogonality of the manifold's terms, if $\lim_{t \rightarrow +\infty} e_{PF} = 0$, then $\lim_{t \rightarrow +\infty} e_{axy} = 0$ and $\lim_{t \rightarrow +\infty} e_F = 0$. Substituting (2.15), (4.9) and (4.10), into \dot{e}_{PF} yields:

$$\dot{e}_{PF} = \left((\mathbf{I} - H^T H) \mathbf{J}_{saxy} \mathbf{L}_s \mathbf{J}_q + H K_f D \mathbf{J}_q \right) u + (H \delta_{Fn} + (\mathbf{I} - H^T H) \delta_{Laxy}) - H \dot{F}_d, \quad (4.13)$$

where $\delta_{Lxya} = [\delta_{La}^T \ \delta_{Lxy}^T]^T$ and $\delta_{Fn} = K_f D \boldsymbol{\delta}_q u_F + \delta_F$. Also, $u = u_{32}$ where u_{32} is the controller output for Stage-3-Substage-2 derived using STSMC.

4.2.3 Switching stage supervisor

To switch between the stages, a robust switching stage supervisor (SSS) is developed. Using SSS, the proposed multi-stage control strategy will be performed in a sequence from Stage-1 to

Stage-4. Some predefined thresholds, such as T_{Na} , T_{xy} , and T_F are defined for switching to the next stage. The SSS procedure is presented in below.

```

Initialize  $T_{Na}, T_{Nxy}, T_F; inx = 1; inx2 = 1; //inx$ 
and  $inx2$  are global variables.
Input:  $e_a, e_{xy}, F;$ 
If ( $inx == 1$ )
   $I_S = 1;$ 
End If
If ( $inx == 2$  or ( $inx == 1$  and  $\|e_a\| \leq T_{Na}$ ))
   $I_S = 2; inx = 2;$ 
End If
If ( $inx == 3$  or ( $inx == 2$  and  $\|e_{xy}\| \leq T_{Nxy}$ ))
   $I_S = 3; inx = 3;$ 
  If ( $inx2 == 1$ )
     $I_{SS} = 1;$ 
  End If
  If ( $inx2 == 2$  or ( $inx2 == 1$  and  $\|F\| \geq T_F$ ))
     $I_{SS} = 2; inx2 = 2;$ 
  End If
End If
Return  $I_S, I_{SS}; // I_S$  and  $I_{SS}$  are indexes of stages
and substages, respectively.

```

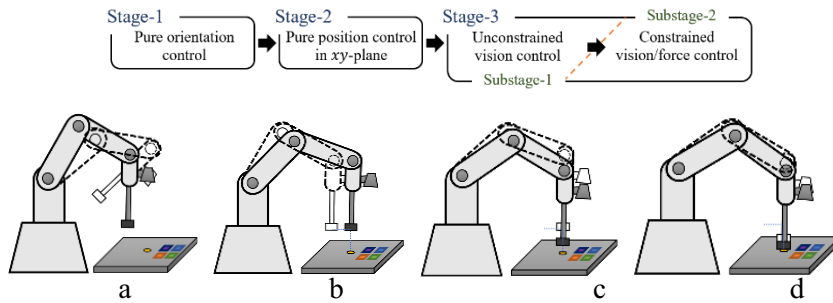


Figure 4.1: Different stages of the proposed strategy.

4.3 Super-Twisting Sliding Mode Controller

In this section, STSMC with a variable-gain sliding surface is designed for controlling each stage of the proposed method.

4.3.1 Variable-gain Sliding Surface

It has been observed that adopting a constant control gain in IBVS deteriorates the performance of the visual servoing process and may lead to extreme oscillations, instability, and low convergence speed. e.g., when the gain is set to a large value, instability and unwanted oscillations occur. On the other hand, when it sets to a small value, the convergence speed decreases. In this research, to handle this issue, a variable-gain sliding surface is defined as follows:

$$\sigma_i = \mathbf{C}_i \bar{e}_i, \quad (4.14)$$

where $\sigma_i \in \mathbb{R}^n$ is the sliding variable, $\mathbf{C}_i \in \mathbb{R}^{n \times n}$ is the variable-gain orthogonal matrix determined as (4.15), and \bar{e}_i is the system error defined as (4.16). According to (4.15), it can be seen that as the error decreases, the value of \mathbf{C}_i changes from a high-level value $\mathbf{c}_{Hi} \in \mathbb{R}^{n \times n}$ to a low-level value $\mathbf{c}_{Li} \in \mathbb{R}^{n \times n}$, where \mathbf{c}_{Hi} and \mathbf{c}_{Li} are orthogonal positive definite matrices. As a result, the vision system converges fast when the error is high and avoids oscillation when the error is low. In (4.15), a_i and b_i are adjustable parameters that determine the characteristics of the smooth switching function $\tanh(\star)$.

$$\mathbf{C}_i = \frac{\tanh(a_i|\bar{e}_i|+b_i)+1}{2} (\mathbf{c}_{Hi} - \mathbf{c}_{Li}) + \mathbf{c}_{Li}, \quad (4.15)$$

$$\bar{e}_1 = e_a, \bar{e}_2 = e_{xy}, \bar{e}_3 = e_p, \bar{e}_4 = e_{PF}. \quad (4.16)$$

Based on (4.9) to (4.11) and (4.13), \bar{e}_i is obtained:

$$\dot{\bar{e}}_i = f_i + \mathbf{g}_i \bar{u}_i + \bar{\delta}_i, \quad (4.17)$$

where

$$\begin{aligned} \bar{u}_1 &= u_1, \bar{u}_2 = u_2, \bar{u}_3 = u_{31}, \bar{u}_4 = u_{32}, \\ f_1 &= 0, f_2 = 0, f_3 = 0, f_4 = -H\dot{F}_d, \\ \mathbf{g}_1 &= \mathbf{J}_{sa} \mathbf{L}_s \mathbf{J}_q, \mathbf{g}_2 = \mathbf{J}_{sxy} \mathbf{L}_s \mathbf{J}_q, \mathbf{g}_3 = \mathbf{J}_q, \\ \mathbf{g}_4 &= (\mathbf{I} - H^T H) \mathbf{J}_{saxy} \mathbf{L}_s \mathbf{J}_q + H K_f D \mathbf{J}_q, \\ \bar{\delta}_1 &= \delta_{La}, \bar{\delta}_2 = \delta_{Lxy}, \bar{\delta}_3 = \delta_{Lq}, \bar{\delta}_4 = H \delta_{Fn} + (\mathbf{I} - H^T H) \delta_{Laxy}. \end{aligned} \quad (4.18)$$

4.3.2 Deriving STSMC Law

Substituting time derivative of (4.14) into (4.17) yields:

$$\dot{\sigma}_i = \mathbf{C}_i \mathbf{g}_i \bar{u}_i + \frac{d(\mathbf{C}_i)}{dt} \bar{e}_i + \mathbf{C}_i f_i + \mathbf{C}_i \bar{\delta}_i. \quad (4.19)$$

Employing the STSMC law of (4.20) for (4.19) results in finite-time convergence of σ_i . The stability proof of the closed-loop system is investigated in Theorem 4. Figure 4.2 shows the block diagram of the proposed control method using STSMC.

$$\begin{aligned} \bar{u}_i &= (\mathbf{C}_i \mathbf{g}_i)^+ \left(\left(-\mathbf{K}_1 |\sigma_i|^{\frac{1}{2}} \text{sign}(\sigma_i) + \eta \right) - \frac{d(\mathbf{C}_i)}{dt} \bar{e}_i - \mathbf{C}_i f_i \right), \\ \dot{\eta} &= -\mathbf{K}_2 \text{sign}(\sigma_i), \end{aligned} \quad (4.20)$$

where $\mathbf{K}_1, \mathbf{K}_2 \in \mathbb{R}^{n \times n}$ are orthogonal matrices.

Assumption 4.1. The following relation holds for δ_i and $\dot{\delta}_i$.

$$\left| (d(\mathbf{C}_i)/dt) \bar{\delta}_i + \mathbf{C}_i \dot{\delta}_i \right| \leq \Delta_i \mid \Delta_i \in \mathbb{R}^n, \Delta_i > 0. \quad (4.21)$$

Assumption 4.2. the following inequalities hold.

$$\mathbf{K}_1 > 0, \mathbf{K}_2 > 3\Delta_i + 2(\Delta_i \Delta_i^T) \mathbf{K}_1. \quad (4.22)$$

Theorem 4.1 (STSMC). Under the control law of (4.20), the closed-loop system of (4.19) is stable as a 2-SM, provided that Assumption 4.1 and Assumption 4.2 are satisfied.

Proof. Substituting (4.20) into (4.19) yields:

$$\begin{aligned} \dot{\sigma}_i &= \mathbf{C}_i \mathbf{g}_i \left((\mathbf{C}_i \mathbf{g}_i)^+ \left(\left(-\mathbf{K}_1 |\sigma_i|^{\frac{1}{2}} \text{sign}(\sigma_i) + \eta \right) - \frac{d(\mathbf{C}_i)}{dt} \bar{e}_i - \mathbf{C}_i f_i \right) \right) + \frac{d(\mathbf{C}_i)}{dt} \bar{e}_i + \mathbf{C}_i f_i + \\ &\quad \mathbf{C}_i \bar{\delta}_i, \quad \dot{\eta} = -\mathbf{K}_2 \text{sign}(\sigma_i). \end{aligned} \quad (4.23)$$

Considering $\zeta = \eta + \mathbf{C}_i \bar{\delta}_i$, (4.23) can be rewritten as:

$$\begin{cases} \dot{\sigma}_i = -\mathbf{K}_1 |\sigma_i|^{\frac{1}{2}} \text{sign}(\sigma_i) + \zeta_i \\ \dot{\zeta}_i = -\mathbf{K}_2 \text{sign}(\sigma_i) + \frac{d(\mathbf{C}_i)}{dt} \bar{\delta}_i + \mathbf{C}_i \dot{\delta}_i \end{cases}. \quad (4.24)$$

Let the Lyapunov function V and its derivative \dot{V} be as [61]:

$$V = v^T Q v, \quad v = \left[\left(|\sigma_i|^{1/2} \text{sign}(\sigma_i) \right)^T \quad \zeta_i^T \right]^T, \quad Q = \frac{1}{2} \begin{bmatrix} 4K_2 + K_1^2 & -K_1 \\ -K_1 & 2I_{n \times n} \end{bmatrix}, \quad (4.25)$$

$$\dot{V} = v^T \text{diag} \left(|\sigma_i|^{-\frac{1}{2}} \right) Q v + \left(\frac{d(c_i)}{dt} \bar{\delta}_i + c_i \dot{\bar{\delta}}_i \right)^T \beta^T v, \quad (4.26)$$

where $\beta^T = [-K_1 \quad 2I_{n \times n}]^T$. Based on Assumption , the following relation yields:

$$\dot{V} \leq -v^T \text{diag} \left(\begin{bmatrix} |\sigma_i|^{-1/2} \\ |\sigma_i|^{-1/2} \end{bmatrix} \right) \bar{Q} v, \quad (4.27)$$

where:

$$\bar{Q} = \frac{1}{2} \begin{bmatrix} 2K_2 + K_1^2 - 2\text{diag}(\Delta_i) & \star \\ - (K_1 + 2\text{diag}(\Delta_i) K_1^{-1}) & I_{n \times n} \end{bmatrix}. \quad (4.28)$$

Considering Assumption , $\bar{Q} > 0$. Hence, the right side of (4.27) is negative. Therefore, based on [59], inequality (4.27) guarantees the finite-time convergence of σ_i and ζ_i towards the origin, at most after the time instant $T_C = \frac{2V_0^{1/2}}{\gamma}$, where $\gamma = \frac{\lambda_{\min}^{1/2}\{Q\} \lambda_{\max}\{\bar{Q}\}}{\lambda_{\max}\{Q\}}$. Based on (4.24), the convergence of σ_i and ζ_i leads to the finite-time convergence of $\dot{\sigma}_i$. Therefore, based on [81], the closed-loop system is a 2-SM.

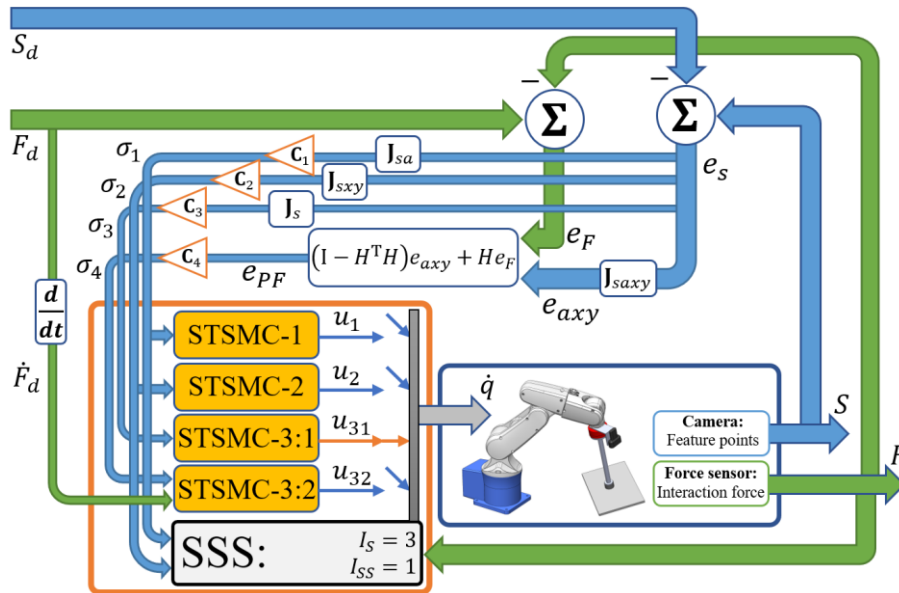


Figure 4.2: Schematic of the proposed hybrid vision and force control method.

4.4 Experimental Results

In this test, the performance of the proposed method in terms of precision, chattering and robustness is compared to those of P/PI controller. The robot starts to move from the initial point S_i to the desired point S_d in the image space, as given in (4.29). S_d is equivalent to the pose of the tool tip in the desired position perpendicular to the surface on the workpiece. When the tool tip touches the surface, the exerted force must track the sinusoidal desired signal F_d (4.29).

$$\begin{aligned} S_i &= [199.3 \quad 75.4 \quad 228.4 \quad 60.3 \quad 240.4 \quad 87.2 \quad 210.4 \quad 100.0]^T, \\ S_d &= [136.9 \quad 92.9 \quad 192.5 \quad 92.5 \quad 192.6 \quad 143.2 \quad 137.5 \quad 143.6]^T, \\ F_d &= 2 \sin(0.2t) + 4. \end{aligned} \quad (4.29)$$

To perform a comparative study, the performance of the proposed method is compared with that of a traditional switch-based hybrid vision force controller. In this method, the vision part is the switch-based IBVS using a P compensator and PI controller for controlling the force signal. Figure 4.3 shows the hybrid vision and force control stages using the proposed controller. According to this figure, during the first and second stages, the orientation of the tool has changed from an angled pose to a perpendicular one above the desired position on the workpiece's surface. This process took 12.3s. In the third stage, the tool starts to move downward, and at the time moment 62.3s, it touches the surface. The results of the hybrid vision and force control using the mentioned methods are plotted in Figure 4.3. According to Figure 4.3a and Figure 4.3b, using the proposed method, the image features are matched precisely with the desired signals when the tool comes into contact with the workpiece at the end of the experiment. Besides, the norms of e_p in Figure 4.3c and Figure 4.3d reveal that compared to P/PI, STSMC has a higher convergence speed in each stage with a higher precision. The e_z graph illustrates that using STSMC, the tool touches the surface after 62.3s. However, using P/PI the time of contact is at the time 99.3s. This superiority is also obvious in Figure 4.3e and Figure 4.3f, which show the process of controlling the force

signal. Accordingly, controlling the force with STSMC is more accurate than that with the P/PI. Additionally, to have a quantitative comparison, several indicators such as IAE, IATE, STD, and RMSE are selected and their values for the obtained experimental results are computed and tabulated in Table 4.1. Referring to this table, STSMC outperforms P/PI in terms of all indicators. Compared to P/PI, STSMC has improved the performance of the vision control by 43.3%, 82.1%, 42.4%, and 75.0% in terms of IAE, IATE, STD, and RMSE, respectively. From the force control aspect, these improvements have been over 84.7%, 67.9%, 87.2%, and 87.4% in terms of IAE, IATE, STD, and RMSE, respectively.

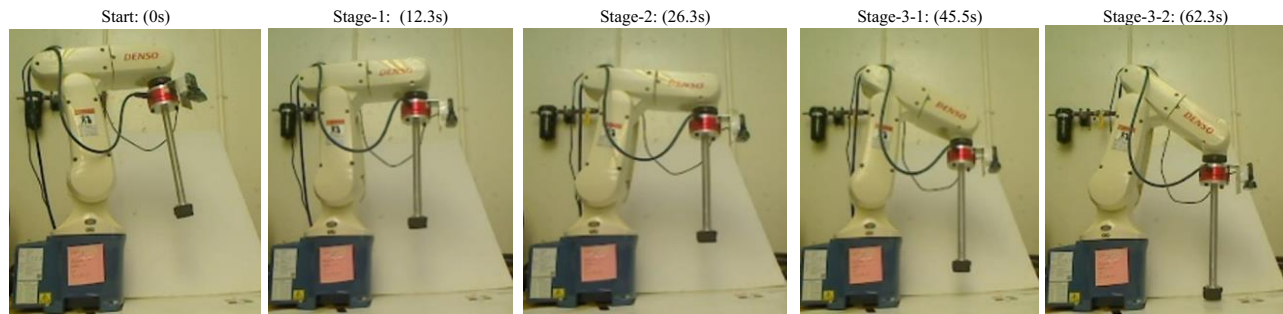


Figure 4.3: The control process of the experiment using the proposed method.

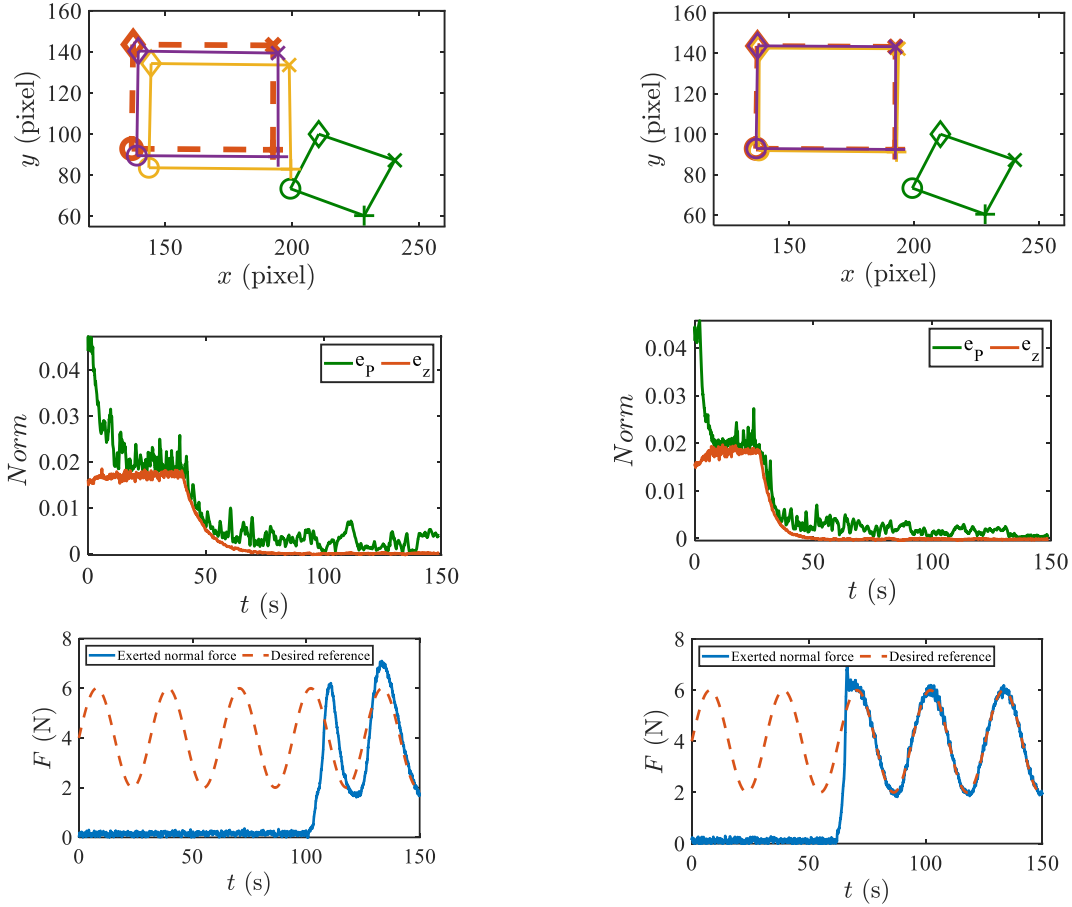


Figure 4.4: Results of the experiment: image features: a) P/PI, b) STSMC, Norms: c) P/PI, d) STSMC, Interacting force: e) P/PI, f) STSMC.

Table 4.1: The indicators' values for the experimental test.

Compensator	System	Indicator			
		IAE	ITAE	STD	RMSE
P/PI	Vision	1.415	53.41	0.01299	0.0196
	Force	69.13	917.18	2.016	2.059
STSMC	Vision	0.987	29.33	0.00912	0.0112
	Force	10.58	293.89	0.258	0.259

4.5 Summary

In this chapter, a new multi-stage hybrid vision and force control approach for industrial robots has been developed. Performing vision control in several sequential stages enables the tool tip to move towards the workpiece and start interacting with the workpiece while it touches the surface

at the desired pose. The designed STSMC method with a variable-gain sliding surface allows the system to reject the uncertainties and increase the control precision while alleviates the chattering. Also, the presented approach, enables the robot to achieve greater flexibility in performing the hybrid vision force tasks successfully. The proposed method has been implemented on an industrial robot performing a touching operation on a planar workpiece. The extensive experimental tests show the effectiveness of the proposed method and its superiority to other well-known methods.

CHAPTER 5 Expansion of IBVS Workspace

5.1 Introduction

As it was discussed in previous chapters, many studies have been conducted to overcome the weaknesses of vision and force control and improve its efficiency. However, the performance of most reported vision and force controllers is not sufficiently high to meet the requirements of industrial applications. An efficient vision and force method feasible for practical robotic operations requires a fast response with strong robustness to feature loss. In the previous chapters, vision and force control methods were proposed and demonstrated that the controller were able to improve the speed and tracking performance of vision and force control methods. However, feature loss caused by the camera's limited FOV still prevents the method from being fully efficient and being applicable to real industrial robots.

In this chapter, a novel approach to address the FOV limitation issue of hybrid vision and force control by EIH industrial robots interacting with planar workspaces is introduced. To this end, instead of considering only one image object on the workpiece, an array of objects is provided in such a way that at least one feature object is in the FOV. So, if an object is going out of FOV, at least another object still exists in the FOV to be used by IBVS. However, conventional IBVS methods (methods that use single feature object) are designed for controlling only one object in the FOV, thus they cannot be employed to carry out this task.

To cope with this issue, a novel hierarchical sliding surface comprising two levels of sliding surfaces is suggested. The 1st level sliding surface comprises the weighted sum of feature errors

corresponding to all objects. Note that these weights are adjusted based on the distance of the objects to the center of image plane and also their complete existence in the FOV. One way of adjusting those value could be using a binary decision-making method, i.e., the distance between the center of each object to the center of image plane is checked. If it is the shortest compared to other, i.e., the condition is satisfied, its corresponding coefficient is set to one, otherwise it is set to zero. However, since objects are moving in the image plane the distance of the objects to the center of the image plane would change and thus, the true value may switch from one object to another. This switching between the objects may lead to deteriorating the control performance, since the desired signal will be discontinuous. To address this issue, fuzzy decision-making method (or fuzzy inference system (FIS)) is adopted [82]. Using FIS, adjusting the surface coefficients will be continuous and also the decision making will be robust and more flexible than the binary counterpart. In [56], the fuzzy decision-making technique is used to adjust the confection of the hieratical sliding surface of a second-order SMC. The results show the effectiveness of the proposed technique over other control methods in terms of chattering, control, effort, and tracking error.

The inputs of the FIS are some indicators that denote the states of the objects in the FOV. Based on the defined fuzzy rules, each coefficient associated with each object takes a value between zero and one, e.g., the coefficient associated with an object that is out of FOV takes zero, and the ones that are close to the center of image plane takes values near one. Accordingly, sliding on this surface results in controlling all objects and smooth transition between the ones that entirely exist in FOV and those that are out of it. The 2nd level sliding surface comprises two orthogonal terms of the 1st level sliding surface and error of the interacting force. Therefore, when sliding state occurs, i.e., when the 2nd level sliding variable equals zero, both orthogonal terms converge to zero

which leads to the hybrid control of vision and force. To bring about the sliding phase, the continuous integral control sliding controller (CISMC) is designed. CISMC exploits a terminal control law as its nominal controller part and adopts supertwist algorithm (STA) as the uncertainty and disturbance rejection part. Therefore, CISMC is robust against uncertainties and leads to high tracking accuracy with a continuous output, which mitigates the chattering problem. The advantage of the proposed control scheme is that it not only can be applied to the vision system with multiple objects, but also eliminates the necessity of designing two individual controllers for vision and interacting force systems. The stability proof of the proposed controller is also included.

5.2 Problem Statement

The main objective of this paper is to develop a robust hybrid control method that enables an eye-in-hand (EIH) industrial robot to perform the interaction task with extended workspace. To this end, instead of using only one object feature, an array of objects (containing n_o objects) is provided on the workpiece in a way that always at least one object is entirely in the FOV. Thus, the limitation of the FOV can be addressed (The schematic of the robotic system and the workpiece is demonstrated in Figure 5.1).

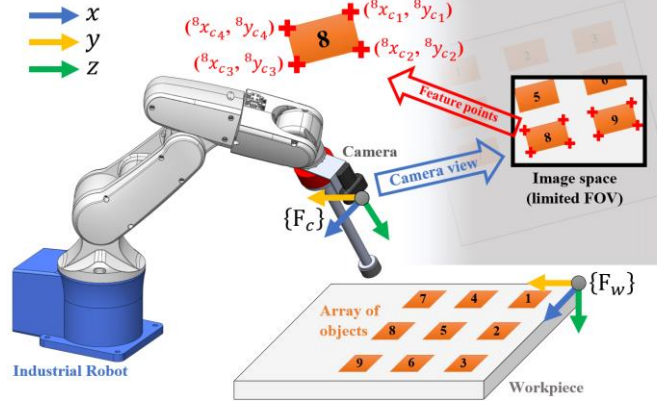


Figure 5.1: Six-DOF industrial robot equipped with a force sensor and camera with EIH configuration interacting with a planar workpiece containing an array of image objects.

5.2.1 Modeling of the Vision System

The kinematic relationship between the set of image features of the i^{th} object and the camera frame $\{F_c\}$ is derived as follows [20], [54], [83]:

$${}^i\dot{s} = {}^iL_s V \quad (5.1)$$

where ${}^i s \in \mathbb{R}^{n_f}$ is the vector of image features of the i^{th} object and n_f is its length, $V \in \mathbb{R}^6$ is the relative velocity screw between the camera and the workpiece, and ${}^iL_s \in \mathbb{R}^{n_f \times 6}$ is the interaction matrix related to the i^{th} object. As stated in [54], [83], [20], employing advanced IBVS control strategies is not possible by adopting the traditional features, since the global stability of the closed-loop system is not ensured due to the fact that their interaction matrices are not invertible. Employing a set of modified image features [46] makes it possible to design advanced robust controllers for IBVS, since the corresponding interaction matrix will be invertible. Accordingly, the modified image features of the i^{th} object, i.e., ${}^i s$, is considered as follows:

$${}^i s = [{}^i\bar{x}_c \quad {}^i\bar{y}_c \quad {}^i\bar{D}_c \quad {}^i\bar{\theta}_{cx} \quad {}^i\bar{\theta}_{cy} \quad {}^i\bar{\theta}_{cz}]^T, \quad (5.2)$$

where

$${}^i\bar{x}_c = \frac{\sum_{j=1}^4 {}^i x_{cj}}{4}, \quad {}^i\bar{y}_c = \frac{\sum_{j=1}^4 {}^i y_{cj}}{4}, \quad (5.3)$$

$$\begin{aligned}
{}^i\bar{D}_c &= \sum_{j=1}^3 \sqrt{\left({}^ix_{c_{j+1}} - {}^ix_{c_j} \right)^2 + \left({}^iy_{c_{j+1}} - {}^iy_{c_j} \right)^2} + \\
&\quad \sqrt{\left({}^ix_{c_1} - {}^ix_{c_4} \right)^2 + \left({}^iy_{c_1} - {}^iy_{c_4} \right)^2}, \\
{}^i\bar{\theta}_{cx} &= \frac{1}{2} \left(\text{atan} \left(\frac{{}^ix_{c_2} - {}^ix_{c_1}}{{}^iy_{c_1} - {}^iy_{c_2}} \right) - \text{atan} \left(\frac{{}^ix_{c_3} - {}^ix_{c_4}}{{}^iy_{c_4} - {}^iy_{c_3}} \right) \right), \\
{}^i\bar{\theta}_{cy} &= \frac{1}{2} \left(\text{atan} \left(\frac{{}^iy_{c_3} - {}^iy_{c_2}}{{}^ix_{c_3} - {}^ix_{c_2}} \right) - \text{atan} \left(\frac{{}^iy_{c_4} - {}^iy_{c_1}}{{}^ix_{c_4} - {}^ix_{c_1}} \right) \right), \\
{}^i\bar{\theta}_{cz} &= \frac{1}{2} \left(\text{atan} \left(\frac{{}^iy_{c_1} - {}^iy_{c_4}}{{}^ix_{c_4} - {}^ix_{c_1}} \right) + \text{atan} \left(\frac{{}^iy_{c_2} - {}^iy_{c_3}}{{}^ix_{c_3} - {}^ix_{c_2}} \right) \right).
\end{aligned}$$

In the relation above, pairs $\left({}^ix_{c_j}, {}^iy_{c_j} \right)$ for $j = 1, \dots, 4$, are the coordinates of the vertices i^{th} object (Figure 5.1). ${}^i\bar{x}_c$ and ${}^i\bar{y}_c$ are the centers of the j^{th} feature points of the i^{th} object and ${}^i\bar{D}_c$ is the perimeter of the rectangular object that is shaped by lines connecting each consecutive corners of the j^{th} feature points of the i^{th} object. The entries of ${}^i\mathbf{L}_s$ are available in [46]. The camera velocity screw is mapped to the joint space using the following relation:

$$V = \mathbf{J}\dot{q}, \quad (5.4)$$

where $\mathbf{J}_q \in \mathbb{R}^{6 \times 6}$ and $\dot{q} \in \mathbb{R}^{6 \times 1}$ are the robot Jacobian and vector of joint velocities, respectively.

Substituting (5.4) into (5.1) yields ${}^i\dot{s} = {}^i\mathbf{L}_s\mathbf{J}\dot{q}$. In real applications, uncertainties always exist in the interaction matrix and Jacobian, i.e., ${}^i\mathbf{L}_s\mathbf{J} = {}^i\hat{\mathbf{L}}_s\hat{\mathbf{J}} + \boldsymbol{\delta}_s$. Accordingly, the following relation yields:

$${}^i\dot{s} = {}^i\hat{\mathbf{L}}_s\hat{\mathbf{J}}\dot{q} + \bar{\boldsymbol{\delta}}_s, \quad (5.5)$$

where, $\bar{\boldsymbol{\delta}}_s = \boldsymbol{\delta}_s\dot{q}$ is the uncertain part of the visual model, and notation $\hat{}$ denotes the nominal part.

5.2.2 Modeling of Interaction Force

To design a force controller, the model of interaction between the tool and the workpiece should be derived. To this end, the stiffness model is exploited [84]. Accordingly, the mathematical

formulation of the interacting force when the tool tip is in contact with the workpiece's surface is modeled as:

$$F = K_f P_f, \quad (5.6)$$

where $K_f \in \mathbb{R}^{6 \times 6}$ is the nominal diagonal stiffness matrix, P_f is the displacement vector, and F is the vector of forces and torques exerted to the tool. Taking time derivative of (5.6) yields:

$$\dot{F} = K_f V. \quad (5.7)$$

Substituting (5.4) into (5.7) yields $\dot{F} = K_f \mathbf{J} \dot{q}$. Considering uncertainties in the kinematic relations and stiffness coefficient, i.e., $K_f \mathbf{J} = \widehat{K}_f \widehat{\mathbf{J}} + \delta_F$, which leads to the following relation:

$$\dot{F} = \widehat{K}_f \widehat{\mathbf{J}} \dot{q} + \bar{\delta}_f, \quad (5.8)$$

where, $\bar{\delta}_f = \delta_F \dot{q}$ is the uncertain part of the interaction force model, and notation $\widehat{\quad}$ denotes the nominal part.

5.3 Extracting the Desired Image Features Trajectories Using Learning-From-Demonstration Method

To perform IBVS by the robot, the desired trajectories in the image space corresponding to the desired path of the end-effector in the Cartesian space (on the workpiece's surface) is required. To this end, a feasible technique based on the learning-from-demonstration method is suggested in [47]. In this method, first the robot's end-effector passes through the desired path on the workpiece manually. In the meantime, the feature points captured by the camera are acquired. Then, using SP-line interpolation technique, the desired image features signals are obtained. So, when this desired image features are tracked by the EIH camera, the end-effector tracks the desired path on the workpiece's surface. This method is designed for a single object which has a very

limited workspace. Thus, multiple objects are used to expand the workspace and a novel learning-from-demonstration is employed to generate the desired trajectory in the image plane.

Accordingly, the robot's end-effector will be passed through the desired path on the workpiece, and at the same time, the feature points of the objects that are entirely in the FOV will be acquired as follows:

$$\begin{aligned} {}^iS_d &= \{ {}^i\bar{s}_{d_1} \quad \cdots \quad {}^i\bar{s}_{d_k} \quad \cdots \quad {}^i\bar{s}_{d_{N_s}} \}, \\ T_d &= \{ t_1 \quad \cdots \quad t_k \quad \cdots \quad t_{N_s} \}, \end{aligned} \quad (5.9)$$

where iS_d is the set of collected image features of the i^{th} object, ${}^i\bar{s}_{d_k}$ is the sample of image features of the i^{th} object at time instant t_k . N_s is the number of samples, and T_d is the set of sampling times.

Note that controlling the sets of the image features of all objects cannot be performed at the same time, since some of them may not be in the FOV. Besides, while the desired features of an object in the FOV is being tracked in part of the path, the object may go out of the FOV and its features can be lost in the rest of the path. Thus, one simple way is to switch to the desired features of the object that has just entered the FOV as the previous object is going out of FOV. However, two main concerns exist: a) In the applications where the robot is interacting with the workpiece, high accuracy of trajectory tracking is required. Nonetheless, switching between different objects may lead to intense oscillation and thus damaging the workpiece, and b) a mechanism should be devised to decide when and to which object the switching should be done, since there might be more than one object in the FOV at the same time. To cope with these issues, it is necessary to generate a smooth and continuous desired image feature signal. To this end, the intensity of the effect of each desired image feature related to each object on the final desired signal can be acquired using a FIS.

Using FIS, the acquired image features of all objects are converted to a single variable \bar{S}_{d_k} as follows:

$$\bar{S}_{d_k} = \sum_{i=1}^{n_o} {}^i\bar{S}_{d_k} \cdot \zeta_i, \quad (5.10)$$

where ζ_i , which is the coefficient of ${}^i\bar{S}_{d_k}$, is evaluated as the i^{th} output of the FIS as follows:

$$\zeta_i = \frac{\sum_{j=1}^{25} \eta_{i,j} \times O_{i,j}}{\sum_{j=1}^{25} \eta_{i,j}}. \quad (5.11)$$

In (5.11), $O_{i,j}$ is the output of the consequent part of the j^{th} fuzzy rule associated with the i^{th} object; $\eta_{i,j}$ is the firing strength of the j^{th} rule of the i^{th} object which is computed using multiplication operation as t-norm operation as follows:

$$\eta_{i,j+5(k-1)} = \mu_{{}^i\tilde{A}_k}(I_{c_j}) \times \mu_{{}^i\tilde{B}_j}(I_{d_i}); j = 1, \dots, 5; k = 1, \dots, 5, \quad (5.12)$$

where $\mu_{{}^i\tilde{A}_k}(\cdot)$ and $\mu_{{}^i\tilde{B}_j}(\cdot)$ are the k^{th} and j^{th} membership functions of the first and the second input associated with the i^{th} object. The inputs of the proposed FIS are I_{c_i} and I_{d_i} which indicate the states of the objects in the FOV and are calculated as follows:

$$I_{c_i} = \|\ {}^i\bar{O}_{od} - \bar{O}_l \|\,, \quad (5.13)$$

$$I_{d_i} = \min_{j \in \{1,2,3,4\}} \left(\left| {}^i x_{cdj} - L_t \right|, \left| {}^i x_{cdj} - L_b \right|, \left| {}^i y_{cdj} - H_r \right|, \left| {}^i y_{cdj} - H_l \right| \right),$$

where ${}^i\bar{O}_{od} = [{}^i\bar{x}_{cd} \quad {}^i\bar{y}_{cd}]^T$ is the coordinate of the center of the i^{th} object in the image plane and \bar{O}_l is the coordinate of the origin of the image plane. L_t , L_b , H_r , and H_l are bounds of the image plane. The schematic of the proposed FIS is illustrated in Figure 5.2a. The fuzzy rules are defined as follows:

$$\begin{aligned} &{}^iR_{j+5(k-1)}: \text{if } (I_{c_i} \text{ is } {}^i\tilde{A}_k) \text{ and } (I_{c_i} \text{ is } {}^i\tilde{B}_j) \\ &\text{then } (\eta_{i,j+5(k-1)} = {}^iC_{j+5(k-1)}), \end{aligned} \quad (5.14)$$

where ${}^i R_{j+5(k-1)}$ is the $(j+k)^{th}$ fuzzy rule of the i^{th} object. For each input five membership functional are considered as shown in Figure 5.2b. ${}^i \tilde{A}_k$ and ${}^i \tilde{B}_j$ are fuzzy linguistic variables of the first and the second inputs related to the i^{th} object, and ${}^i C_{j+5(k-1)}$ is the output of the $(j+5(k-1))^{th}$ rule, all of which are defined as follows:

$$\begin{aligned}
 {}^i \tilde{A}_k &= \left\{ \left(x, \mu_{{}^i \tilde{A}_k}(x) \right) \mid x \in \mathbb{R}, \mu_{{}^i \tilde{A}_k}(x) = \right. \\
 & \left. \begin{cases} \text{trap}(a_{m_k}, b_{m_k}, c_{m_k}, d_{m_k}), & k = 2, \dots, 4 \\ \text{LF}(a_{m_k}, b_{m_k}), & k = 1 \\ \text{RF}(c_{m_k}, d_{m_k}), & k = 5 \end{cases} \right\}, \\
 {}^i \tilde{B}_k &= \left\{ \left(x, \mu_{{}^i \tilde{B}_k}(x) \right) \mid x \in \mathbb{R}, \mu_{{}^i \tilde{B}_k}(x) = \right. \\
 & \left. \begin{cases} \text{trap}(e_{m_k}, f_{m_k}, g_{m_k}, h_{m_k}), & k = 2, \dots, 4 \\ \text{LF}(e_{m_k}, f_{m_k}), & k = 1 \\ \text{RF}(g_{m_k}, h_{m_k}), & k = 5 \end{cases} \right\},
 \end{aligned} \tag{5.15}$$

where, $\text{trap}(\dots)$, $\text{LF}(\dots)$, and $\text{RF}(\dots)$ are trapezoidal, left and right membership functions [84], and $a_{m_k}, b_{m_k}, c_{m_k}, d_{m_k}, e_{m_k}, f_{m_k}, g_{m_k},$ and h_{m_k} are the membership parameters.

The fuzzy rules are defined in a way that when an object, e.g., i^{th} object, is out of the FOV its corresponding ζ_i equals zero. Also, if the object is in the FOV it takes a value between 0 and 1. The closer the object is to the center of image plane and further from the image plane's bounds, the value of ζ_i is larger. After collecting the samples and generating the new variable (5.17), SP-line method is used to generate the overall signal

$$\hat{S}_d(t) = \text{SPL}(\bar{S}_d, T_d, t). \tag{5.16}$$

SP-line function that takes the sample data sets, i.e., \bar{S}_d and T_d , and time instant t and returns the desired signal at the time instant t (More details are available in [47]). Note that $\hat{S}_d(t)$ is defined as desired generalized image feature signal. By tracking $\hat{S}_d(t)$ using an appropriate controller in the image space, the end-effector tracks the desired trajectory in the cartesian space as it was when collecting the data (learning phase). To this end, a novel controller for robust IBVS is developed and presented in the next section.

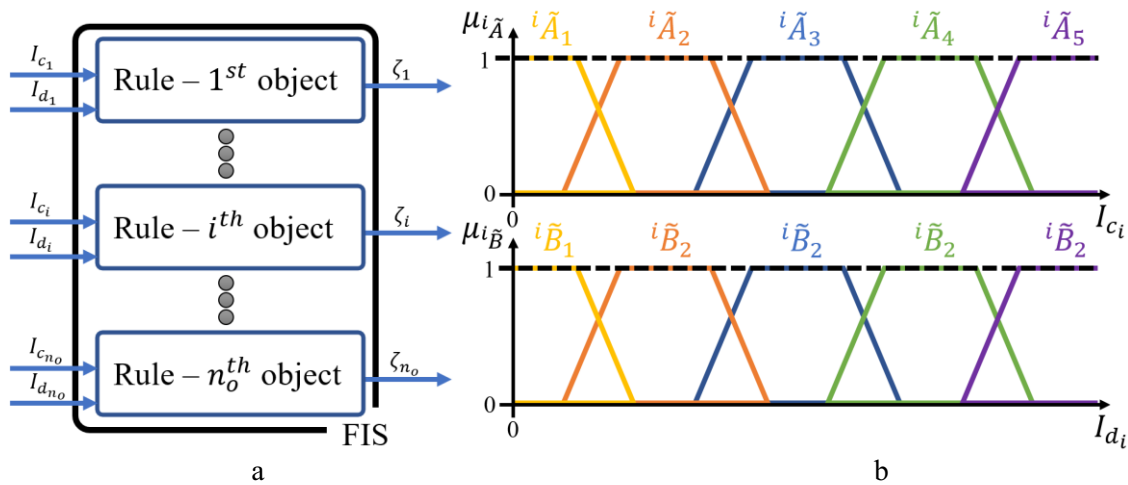


Figure 5.2: a) The schematic of the proposed FIS, b) Membership functions.

5.4 Designing Hybrid Vision and Force Control Using Hierarchical Sliding Mode Control Method

As mentioned before, IBVS with EIH configuration cannot be performed utilizing conventional methods when multiple feature objects are in FOV. Besides, in this study, the objective is to hybrid control of vision and interacting force. Thus, a novel hierarchical sliding surface (HSS) is suggested that could address the existing issues. To constitute the HSS, FIS and orthogonality principle are used for each level, respectively. Additionally, continuous integral sliding mode control method, which shows a superior performance for hybrid vision and force control, is designed for hybrid vision and force control in this study.

5.4.1 Hierarchical Sliding Surface

HSS consists of two level. The first layer is obtained for handling the problem of having multiple image objects and the second one is for addressing the issue of hybrid control of vision and force simultaneously.

5.4.1.1 First Level Sliding Surface

The first level of the HSS includes the error of the generalized image feature e_{σ_1} which is utilized as the following relation:

$$\sigma_1 = \hat{\mathbf{L}}_s^{-1} e_s, \quad e_s = \hat{S} - \hat{S}_d \quad (5.17)$$

where σ_1 is the first level sliding surface, e_s is error of the generalized image feature, and \hat{S} is the generalized image feature that can be evaluated using FIS with the same process as formulated in section III as follows:

$$\hat{S} = \sum_{i=1}^{n_o} i_s \cdot \zeta_i \quad (5.18)$$

where ζ_i is obtained by (5.11).

5.4.1.2 Second Level Sliding Surface: Hybridization of Vision and Force

To control the force and vision simultaneously, the orthogonal sliding variable is given as follows:

$$\sigma_2 = \mathbf{K}_c(\mathbf{Q} - \mathbf{I}_{6 \times 6})\sigma_1 + \lambda \mathbf{Q} e_f \quad (5.19)$$

where $e_f \in \mathbb{R}^6$ and $\mathbf{Q} \in \mathbb{R}^{6 \times 6}$ are the vector of interaction force errors and the compliance selection matrix, respectively, presented in (5.20) and (5.21); $\mathbf{K}_c \in \mathbb{R}^{6 \times 6}$ and λ are positive definite orthogonal matrix and scalars that their values should be set properly.

$$e_f = F - F_d \quad (5.20)$$

$$\mathbf{Q} = \gamma D^T D \quad (5.21)$$

In the relations above, $F_d \in \mathbb{R}^6$ is the vector of desired forces $D \in \mathbb{R}^6$ is the selection vector. Its entries are either zero or one, corresponding to directions where the exerted force must be controlled. $\psi \in \{0,1\}$ is a binary variable which takes zero when the robot has a free motion and takes one when the robot is interacting with the workpiece. In this research, the interaction force in the normal direction to the end-effector is controlled. Thus, D is defined as follows:

$$D = [0 \quad 0 \quad 1 \quad 0 \quad 0 \quad 0] \quad (5.22)$$

Note that the dot product of the first and the second terms of σ_2 are orotogonal. Therefore, $\sigma_2 = 0$, which is the 2nd level sliding surface, leads to $(\mathbf{Q} - \mathbf{I}_{6 \times 6})\sigma_1 = 0$ and $\mathbf{Q}e_f = 0$, which is the main objective of the hybrid vision and force control. In the next subsection, CISMV control will be developed to reach the mentioned objective, i.e., $\sigma_2 = 0$.

Remark 5.1. At the start time control process, i.e., when the robot is not fully converged towards the desired potions, the objects that their desired signals are available may not be in the FOV, i.e., feature loss before the convergence. Therefore, the control process cannot be conducted. To handle this issue, a trajectory planning method is suggested in the next subsection.

5.4.1.3 Trajectory Planning for Free-Motion Task before Interaction

At the beginning of the control process, the robot is not convergent and should perform a free motion to reach the start point of the desired path on the workpiece's surface. However, the related objects to the available desired image features may not be in FOV. Thus, the IBVS cannot be performed. Besides, since the robot is not convergence, it might be in the wrong position when it touches the surface and starts interaction, which may damage the workpiece. To cope with these issues, a trajectory planning algorithm in the image space is devised for free-motion, i.e., pure IBVS, before starting the interaction. Assume that the shape and the location of objects on the workpiece's surface are known. Also, assume that the desired set of image feature corresponding

to the i^{th} object when the camera is above that object with a specific distance from the surface is obtained as follows:

$${}^i s_{td} = [{}^i \bar{x}_{td} \quad {}^i \bar{y}_{td} \quad \bar{D}_{td} \quad 0 \quad 0 \quad 0]^T \quad (5.23)$$

Consider that at the beginning of the control process, the \bar{k}^{th} object is in the FOV while the \hat{k}^{th} object needs to be in the FOV since the desired image features corresponding to this object are available and extracted using learning by demonstration method (Figure 5.3). Also, consider that the image features corresponding to the initial point and end point of the desired path on the workpiece in order to move from \bar{k}^{th} object towards \hat{k}^{th} object are ${}^i s_A$ and ${}^i s_B$ for $i = 1, \dots, n_o$ respectively, given as:

$$\begin{aligned} {}^i s_A &= [{}^i \bar{x}_a \quad {}^i \bar{y}_a \quad {}^i \bar{D}_a \quad {}^i \bar{\theta}_{ax} \quad {}^i \bar{\theta}_{ay} \quad {}^i \bar{\theta}_{az}]^T, \\ {}^i s_B &= [{}^i \bar{x}_b \quad {}^i \bar{y}_b \quad {}^i \bar{D}_b \quad {}^i \bar{\theta}_{bx} \quad {}^i \bar{\theta}_{by} \quad {}^i \bar{\theta}_{bz}]^T \end{aligned} \quad (5.24)$$

Accordingly, the suggested trajectory planning comprises the following steps:

- First, the robot performs IBVS and regulation on $\bar{k} s_{td}$.
- Then, using the proposed control method, the robot performs IBVS and tracks the generated desired trajectory given in (5.25), to reach the point above the desired path initial point on the

$$\text{workpiece } \hat{k} s_{\hat{A}} = [\hat{k} \bar{x}_a \quad \hat{k} \bar{y}_a \quad \bar{D}_{td} \quad 0 \quad 0 \quad 0]^T.$$

$$\begin{aligned} \bullet \quad {}^i \hat{s}_d &= \hat{k} s_{td} + [m_{u_i} \quad m_{v_i} \quad 0 \quad 0 \quad 0 \quad 0]^T, \\ \bullet \quad i &= 1, \dots, n_o \end{aligned} \quad (5.25)$$

The variables of the relation above are defined as follows:

$$\begin{aligned} m_{u_i} &= l_{u_i} + a_u t + b_u, \quad m_{v_i} = h_{v_i} + a_v t + b_v, \\ a_u &= \frac{\hat{k} \bar{x}_a + l_{u_{\hat{k}}} - l_{u_{\bar{k}}}}{T_I}, \quad a_v = \frac{\hat{k} \bar{y}_a + h_{v_{\hat{k}}} - h_{v_{\bar{k}}}}{T_I}, \\ b_u &= -l_{u_{\bar{k}}}, \quad b_v = -h_{v_{\bar{k}}}, \quad i = 1, \dots, n_o \end{aligned} \quad (5.26)$$

where T_i is expected duration of the path tracking and (l_{u_i}, h_{v_i}) for $i = 1, \dots, n_o$ are the coordinates of the objects relative to the 1st object in image plane when ${}^i\bar{D}_c = \bar{D}_{td}$ (Figure 5.3).

- Finally, the robot touches the desired path on the workpiece and the interaction starts.

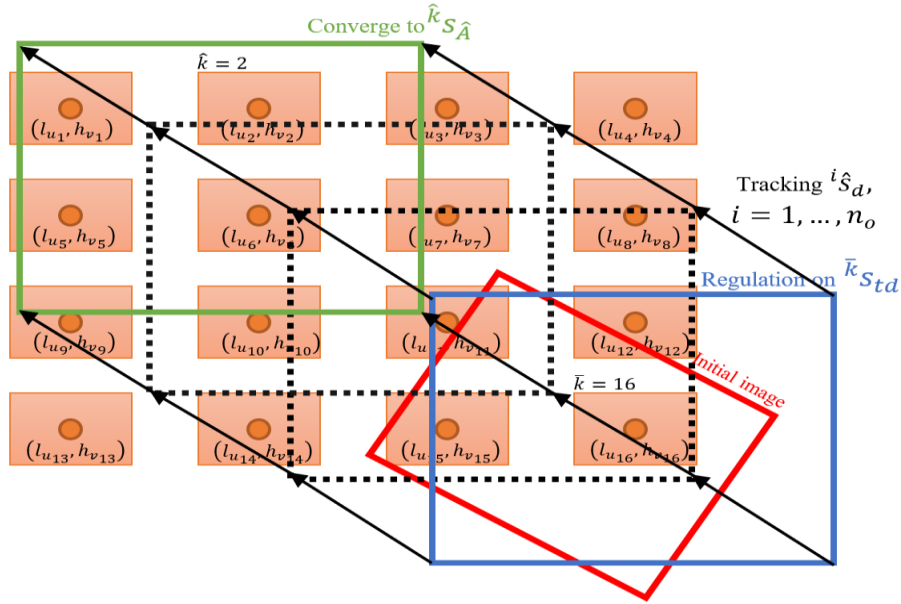


Figure 5.3: Desired feature loss at the beginning of IBVS and trajectory tracking by free motion to converge to $\hat{k} S_{\hat{A}}$.

5.4.2 Continuous Integral Sliding Mode Control

To achieve the mentioned objective in the previous subsection, i.e., $\sigma_2 = 0$, CISMCM is suggested. CISMCM is basically an ISMC which exploits a terminal control law as its nominal control law, which results in gaining a high tracking accuracy, and also uses STA as a substitution to its discontinuous part for rejecting the existing uncertainties, which leads to a continuous output and thus mitigating the chattering.

5.4.2.1 Control Law Design

As an ISMC, the overall control law of the CISMCM comprises two parts as follows:

$$u = u_n + u_c \quad (5.27)$$

where u_n is the nominal control law which is obtained based on the terminal control law, and u_c is the contiguous control law for disturbance and uncertainties rejection which is utilized by adopting STA as follows:

$$u_n = -\hat{\mathbf{J}}^{-1}(\mathbf{K}_c(\mathbf{Q} - \mathbf{I}_{6 \times 6})(\sum_{i=1}^{n_o} \zeta_i) + \lambda \mathbf{Q} \hat{K}_f)^{-1} \left(-u_t - (\mathbf{K}_c(\mathbf{Q} - \mathbf{I}_{6 \times 6}) \hat{\mathbf{L}}_s^{-1} \hat{S}_d + \lambda \mathbf{Q} \dot{F}_d) \right) \quad (5.28)$$

$$u_c = -\hat{\mathbf{J}}^{-1}(\mathbf{K}_c(\mathbf{Q} - \mathbf{I}_{6 \times 6})(\sum_{i=1}^{n_o} \zeta_i) + \lambda \mathbf{Q} \hat{K}_f)^{-1} (-u_{STA}) \quad (5.29)$$

In the relations above, u_t and u_{STA} are the terminal control law and super twisting algorithm given as follows:

$$u_t = -\mathbf{K}_1 \sigma_2 - \mathbf{K}_2 \text{sig}^{\frac{1}{2}}(\sigma_2) \quad (5.30)$$

$$u_{STA} = -\mathbf{D}_1 \text{sig}^{\frac{1}{2}}(\sigma_I) + \dot{\beta} \quad (5.31)$$

$$\beta = -\mathbf{D}_2 \text{sign}(\sigma_I)$$

where \mathbf{K}_1 and \mathbf{K}_2 are positive definite diagonal matrices of the feedback control coefficients and \mathbf{D}_1 to \mathbf{D}_4 are positive definite diagonal matrices of the STA algorithm; $\text{sig}^{\frac{1}{2}}(\cdot) = |\cdot| \text{sign}(\cdot)$, and σ_I is the integral sliding variable given as follows:

$$\sigma_I = \sigma_2 - \sigma_{2_0} - \int_0^t \left(\mathbf{K}_c(\mathbf{Q} - \mathbf{I}_{6 \times 6}) \sum_{i=1}^{n_o} \zeta_i (\hat{\mathbf{J}} u_n - \hat{S}_d) + \lambda \mathbf{Q} (\hat{K}_f \hat{\mathbf{J}} u_n - \dot{F}_d) \right) dt \quad (5.32)$$

where σ_{2_0} is the initial value of σ_2 , i.e., when $t = 0$. The block diagram of the proposed control method is depicted in Figure 5.4.

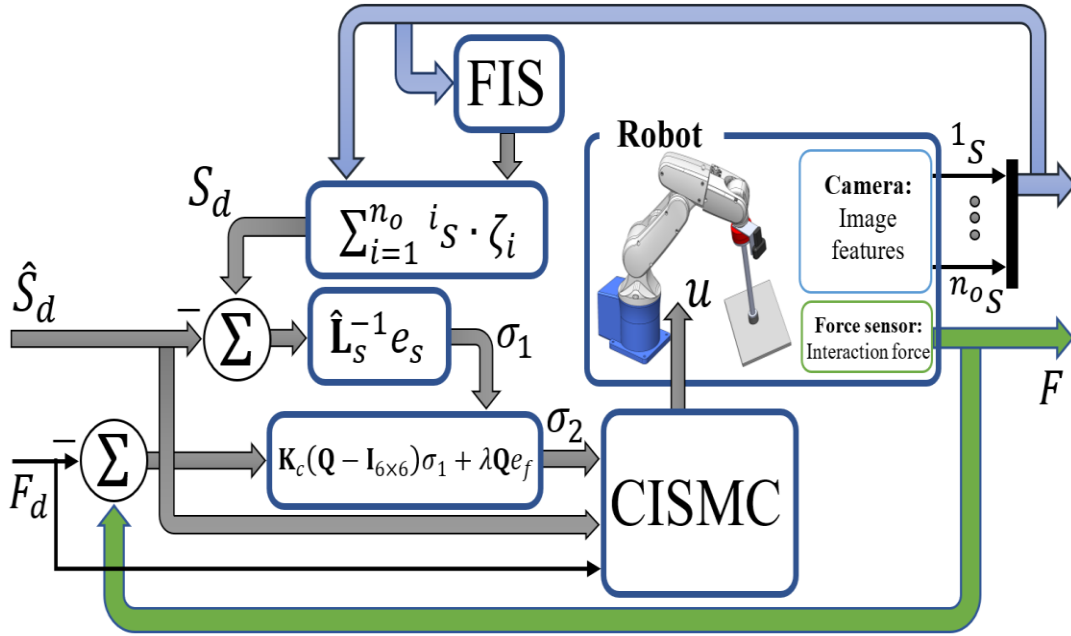


Figure 5.4: Schematic of the proposed robust hybrid controller.

5.4.2.2 Stability and Performance Analysis

The stability proof of CISM C is presented in Theorem 5.1. A necessary assumption for this theory is considered as follows:

Assumption 5.1. The following relation holds STA parameters:

$$\mathbf{D}_1 > 0, \text{diag}(\mathbf{D}_2) > 3\Delta_L + 2(\Delta_L \Delta_L^T)\mathbf{D}_1 \quad (5.33)$$

Assumption 5.2. The following relation holds for δ_L :

$$|\dot{\delta}_L| \leq \Delta_L \mid \Delta_L \in \mathbb{R}^{6 \times 1}, \Delta_L > 0 \quad (5.34)$$

where,

$$\delta_L = \delta_d + \mathbf{K}_c(\mathbf{Q} - \mathbf{I}_{6 \times 6})\hat{\mathbf{L}}_s^{-1} \sum_{i=1}^{n_o} (\zeta_i \bar{\delta}_s) + \lambda \mathbf{Q}(\bar{\delta}_f) \quad (5.35)$$

Theorem 5.1. Applying the CISM C law of (5.27) to an eye-in-hand (EIH) industrial robot with multiple image objects leads to finite-time convergence of σ_2 , provided that Assumption and Assumption are satisfied.

Proof. By taking time derivative of σ_2 (5.19) and substituting (5.27) into it, the following relation yields:

$$\dot{\sigma}_2 = \mathbf{K}_c(\mathbf{Q} - \mathbf{I}_{6 \times 6}) \left(\sum_{i=1}^{n_o} \zeta_i \hat{\mathbf{L}}_s^{-1} ({}^i \hat{\mathbf{L}}_s \hat{\mathbf{J}}(u_n + u_c) - {}^i s_d) \right) + \lambda \mathbf{Q}(\hat{K}_f \hat{\mathbf{J}}(u_n + u_c) - \dot{F}_d) + \delta_L \quad (5.36)$$

By substituting (5.36) into time derivative of σ_I in (5.32), the following relation is obtained:

$$\dot{\sigma}_I = (\mathbf{K}_c(\mathbf{Q} - \mathbf{I}_{6 \times 6}) \sum_{i=1}^{n_o} \zeta_i) + \lambda \mathbf{Q} \hat{K}_f \hat{\mathbf{J}} u_c + \delta_L \quad (5.37)$$

Substituting (5.29) and (5.31) into (5.37), and considering $\omega = \beta + \delta_L$, results in the following closed-loop system:

$$\begin{aligned} \dot{\sigma}_I &= -\mathbf{D}_1 \text{sig}^{\frac{1}{2}}(\sigma_I) + \omega \\ \dot{\omega} &= -\mathbf{D}_2 \text{sign}(\sigma_I) + \dot{\delta}_L \end{aligned} \quad (5.38)$$

Let the candidate Lyapunov function V_1 and its derivative be as follows:

$$V_1 = \mathbf{v}^T \mathbf{\Gamma} \mathbf{v}, \quad \mathbf{v} = \left[\left(\text{sig}^{\frac{1}{2}}(\sigma_I) \right)^T \quad \omega^T \right]^T, \quad \mathbf{\Gamma} = \frac{1}{2} \begin{bmatrix} 4\mathbf{D}_2 + \mathbf{D}_1^2 & -\mathbf{D}_1 \\ -\mathbf{D}_1 & 2\mathbf{I}_{6 \times 6} \end{bmatrix} \quad (5.39)$$

$$\dot{V}_1 = \mathbf{v}^T \text{diag} \left(|\sigma_I|^{-\frac{1}{2}} \right) \mathbf{\Gamma} \mathbf{v} + (\dot{\delta}_L)^T \mathbf{\beta}^T \mathbf{v} \quad (5.40)$$

where $\mathbf{\beta}^T = [-\mathbf{D}_1 \quad 2\mathbf{I}_{6 \times 6}]^T$. Based on Assumption, the following relation yields:

$$\dot{V}_1 \leq -\mathbf{v}^T \text{diag} \left(\begin{bmatrix} |\sigma_i|^{-1/2} \\ |\sigma_i|^{-1/2} \end{bmatrix} \right) \bar{\mathbf{\Gamma}} \mathbf{v} \quad (5.41)$$

where,

$$\bar{\mathbf{\Gamma}} = \frac{1}{2} \begin{bmatrix} 2\mathbf{D}_2 + \mathbf{D}_1^2 - 2\text{diag}(\Delta_L) & \star \\ -(\mathbf{D}_1 + 2\text{diag}(\Delta_L)\mathbf{D}_1^{-1}) & \mathbf{I}_{n \times n} \end{bmatrix} \quad (5.42)$$

Considering Assumption , $\bar{\mathbf{\Gamma}} > 0$. Hence, the right side of (5.41) is negative. Therefore, based on [59], inequality (5.41) guarantees the finite-time convergence of σ_i and ζ_i towards origin, at most

after the time instant $T_1 = \frac{2V_1^{1/2}}{\bar{\gamma}} \Big|_{t=0}$, where $\bar{\gamma} = \frac{\lambda_{\min}^{1/2}\{\bar{\mathbf{\Gamma}}\}\lambda_{\max}\{\bar{\mathbf{\Gamma}}\}}{\lambda_{\max}\{\bar{\mathbf{\Gamma}}\}}$.

Based on (5.38), convergence of σ_i and ζ_i leads to the finite-time convergence of $\dot{\sigma}_i$. Therefore, after T_1 , the left-hand side of (5.37) is zero, which yields the following relation:

$$(\mathbf{K}_c(\mathbf{Q} - \mathbf{I}_{6 \times 6})(\sum_{i=1}^{n_o} \zeta_i) + \lambda \mathbf{Q} \widehat{\mathbf{K}}_f) \hat{\mathbf{J}} u_c = -\delta_L \quad (5.43)$$

Let the candidate Lyapunov function V_2 and its derivative 2nd sliding variable σ_2 be as follows:

$$V_2 = (1/2) \sigma_2^T \sigma_2, \gamma_2 > 0 \quad (5.44)$$

$$\dot{V}_2 = \sigma_2^T \dot{\sigma}_2 \quad (5.45)$$

Substituting (5.36) into (5.45) yields:

$$\begin{aligned} \dot{V}_2 = \sigma_2^T \left(\mathbf{K}_c(\mathbf{Q} - \mathbf{I}_{6 \times 6}) \left(\sum_{i=1}^{n_o} \zeta_i \hat{\mathbf{L}}_s^{-1} \left({}^i \hat{\mathbf{L}}_s \hat{\mathbf{J}}(u_n + u_c) - {}^i s_d \right) \right) + \lambda \mathbf{Q}(\widehat{\mathbf{K}}_f \hat{\mathbf{J}}(u_n + u_c) - \right. \\ \left. \dot{F}_d) + \delta_L \right) \end{aligned} \quad (5.46)$$

Substituting (5.43) into the relation above results in the following relation:

$$\dot{V}_2 = \sigma_2^T \left(\mathbf{K}_c(\mathbf{Q} - \mathbf{I}_{6 \times 6}) \left(\sum_{i=1}^{n_o} \zeta_i \hat{\mathbf{L}}_s^{-1} \left({}^i \hat{\mathbf{L}}_s \hat{\mathbf{J}} u_n - {}^i s_d \right) \right) + \lambda \mathbf{Q}(\widehat{\mathbf{K}}_f \hat{\mathbf{J}} u_n - \dot{F}_d) \right) \quad (5.47)$$

Also, by substituting (5.28) and (5.30) into (5.47), the following relation yields:

$$\dot{V}_2 = -\sigma_2^T \left(\mathbf{K}_1 \sigma_2 + \mathbf{K}_2 \text{sig}^{\frac{1}{2}}(\sigma_2) \right) \quad (5.48)$$

Hence, $\dot{V}_2 \leq 0$ and therefore, system of (5.36) is stable. According to (5.44) one has $\sigma_2^T \sigma_2 = 2V_2$.

Thus, the following conditions are satisfied.

$$-\sigma_2^T \mathbf{K}_1 \sigma_2 \leq -k_{1m} (2V_2), -\sigma_2^T \mathbf{K}_2 \text{sig}^{\frac{1}{2}}(\sigma_2) \leq -k_{2m} (2V_2)^{3/4} \quad (5.49)$$

where k_{1m} and k_{2m} are the minimum eigenvalues of \mathbf{K}_1 and \mathbf{K}_2 respectively. Comparing (5.49)

with (5.48), the following inequality is obtained.

$$\dot{V}_2 \leq -k_{1m} 2V_k - k_{2m} (2V_2)^{3/4} \quad (5.50)$$

Considering $\alpha_T = \frac{3}{4}$ and $K_T = 2^{\alpha_T} k_{2m}$, the inequality above results in $\dot{V}_2 \leq -K_T V_2^{\alpha_T}$. Since $K_T > 0$ and $0 < \alpha_T < 1$, based on finite-time theory in [59], V_2 converges to zero in finite time $T_2 \leq \frac{V_2^{1-\alpha_T}}{K_T(1-\alpha_T)}$. Hence, after T_2 , one has $\sigma_2 = 0$ and Theorem 5.1 is proved.

5.5 Experimental Results

5.5.1 First Experiment

Since the expansion of the workspace depends on the distance of the camera to the workpiece and the number of the image objects, in this experiment, the extent of the expansion of the workspace are examined when the robot is interacting with the planar workpiece (distance of the camera to the workpiece's surface is 0.275m) for different number of image objects (for 1, 2, 4, 6, 12, 18 objects). The size of the workspace for all cases are demonstrated in Figure 5.5. According to this figure, the expansion is at least 54.89%, 136.02%, 239.07% and 363.89% for two, four, six and twelve objects, respectively. Interestingly, the expansion has not improved when the number of objects is more than twelve. This is due to the fact that existing too many objects may occupy the workpiece surface which prevents the end-effector to interact with the workpiece by blocking the objects by the tool-tip.

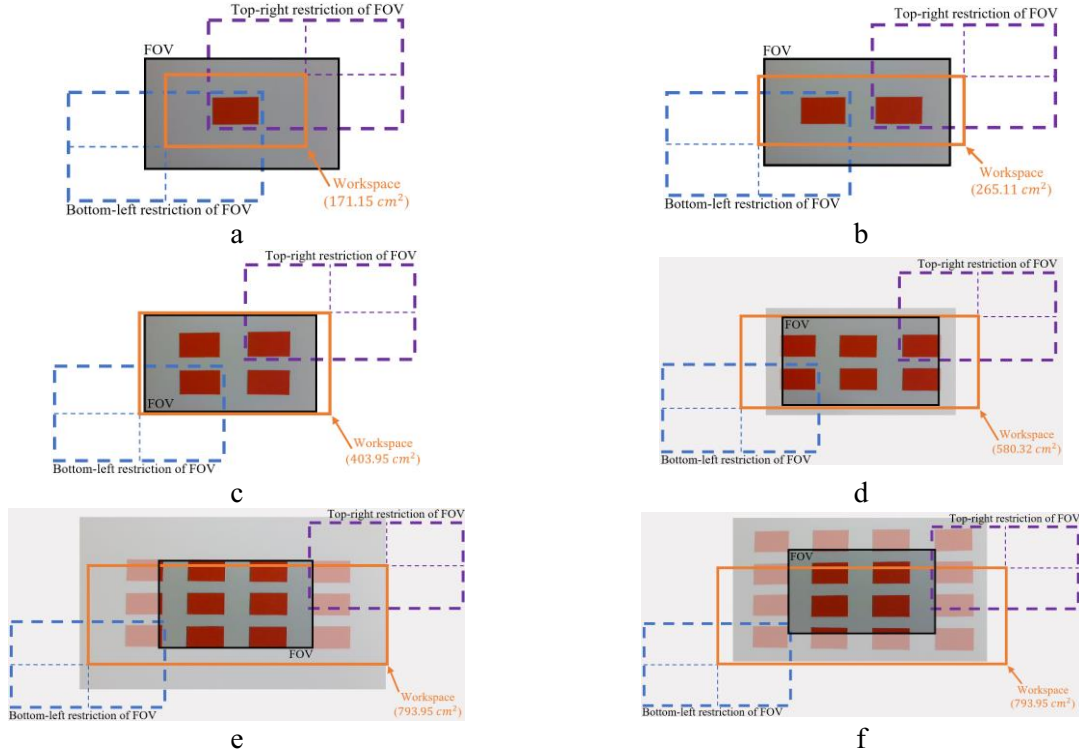


Figure 5.5: a) Workspace for one image object, b) Workspace for two image object, c) Workspace for four image object, d) Workspace for six image object, e) Workspace for twelve image object, f) Workspace for eighteen image object

Furthermore, an infinity-shape path on the workpiece with single and multiple image object (six objects) is tracked by the robotic arm. The size of the path is set in a way that it covers the whole workspace to show the effect of proposed method in such scenarios. Using learning-by-demonstration method (presented in section III), the data accusation process and the desired signals are obtained and shown in Figure 5.6. The desired signal for interacting force is determined as follows:

$$F_d(t) = 6 + 1.5 \sin(0.15t) \quad (5.51)$$

The series images of the robot tracking the desired paths are presented in Figure 5.7a. Also, the results of controlling the interacting force are plotted in Figure 5.7b. According to this figure, it can be seen that the robot can interact with the workpiece in a larger area.

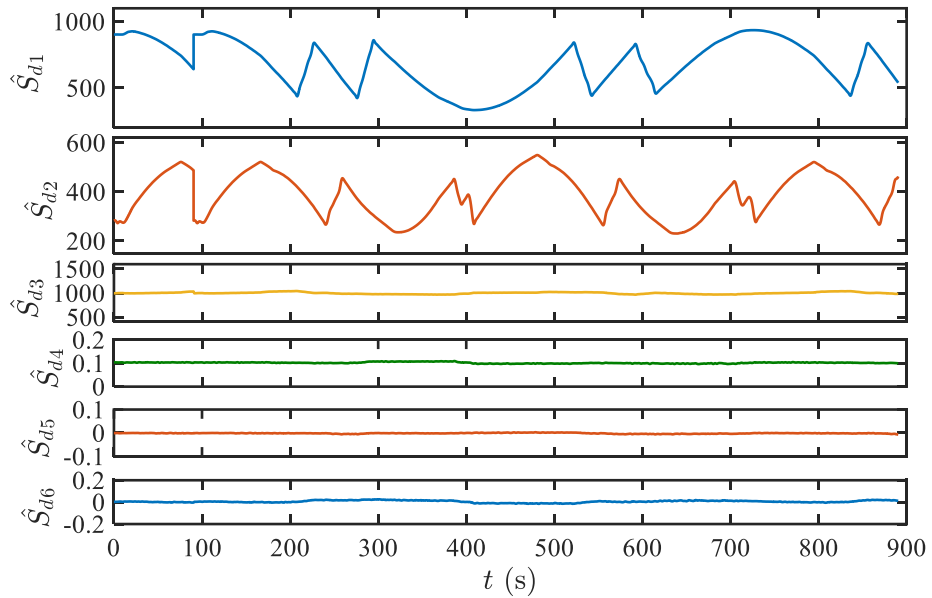
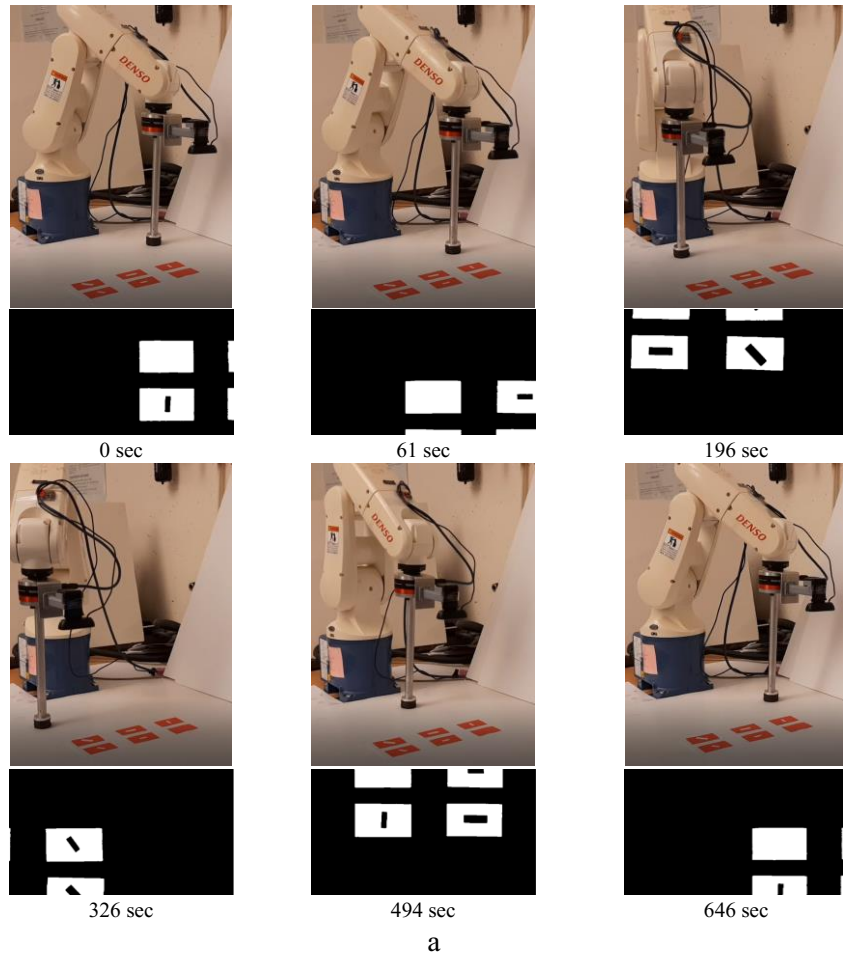


Figure 5.6: a) Data collecting process by the robot for generating the desired image signal; b) Desired obtained signals

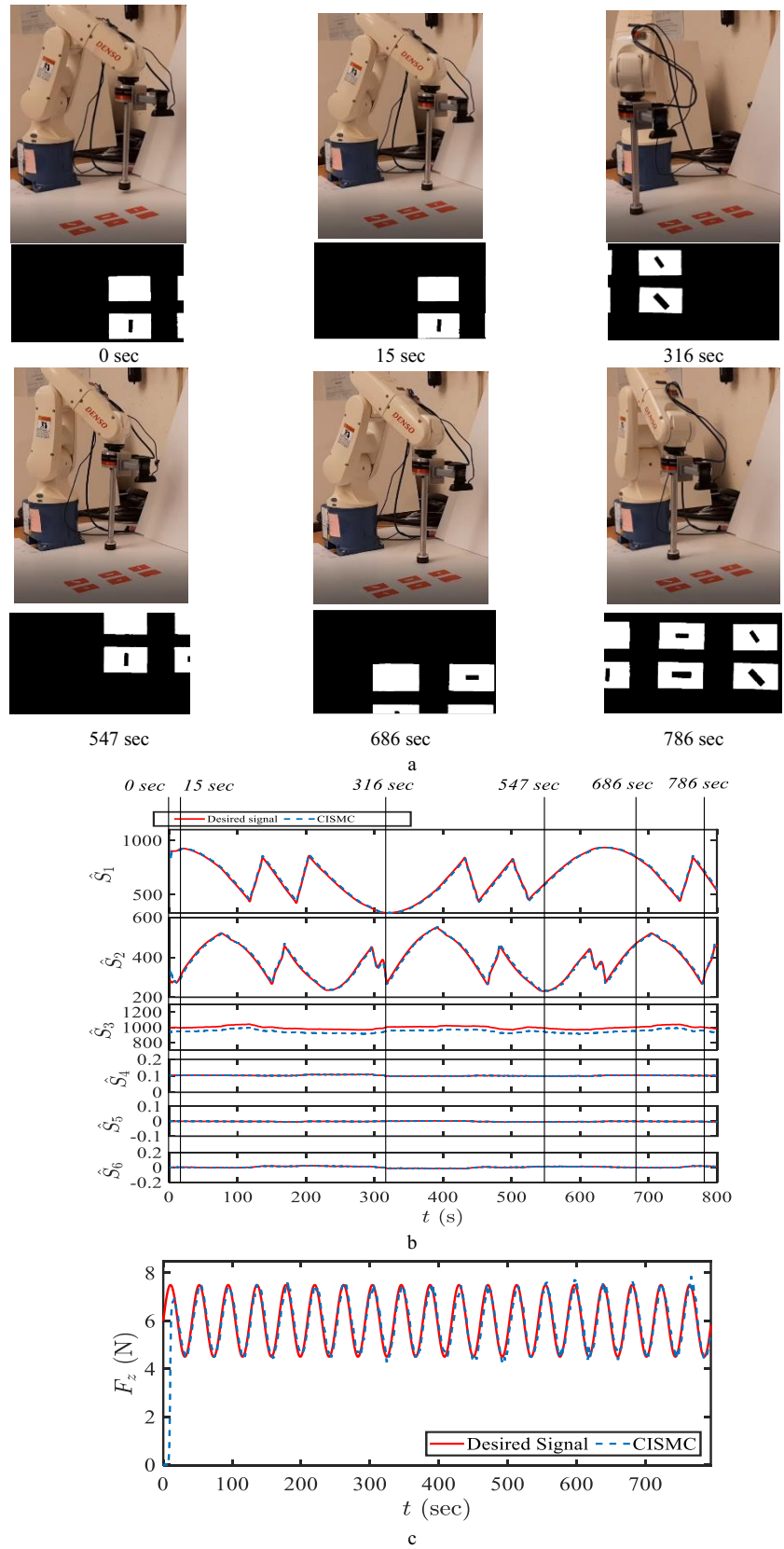


Figure 5.7: a) Robot operating the first test along with the captured image features in real time, b) Tracking the desired path and tracking the desired force signal.

5.5.2 Second Experiment

In the second experiment, the focus is on the proposed controller performance and path planning technique for handling feature loss at the beginning of the operation. To this end, the robot starts far away from the departure point of the defined path. Also, a traditional hybrid vision and force controller (P/PI controller) and traditional SMC are applied to the system to compare their control results with the proposed method. The number of image objects are considered to be six and the desired path considered to be an infinity-shaped path.

The desired signal for this test is the same as desired signals for the first experiment. However, the desired signal for the interacting force signal is a constant of 5N. In Figure 5.8, a series of images of the robot and features objects is provided which shows the performance of the proposed method when the desired object is not in the FOV. In this case, the operation is achieved in three phases. In the first phase, the object which is completely in the FOV and closest to the center, i.e., feature object #2, is detected by the camera and the robot starts regulating on it which takes from 0 to 7s. In the second phase, the robot moves from this object towards the start point of the desired path. At the beginning of the desired path, the first feature object is located close to the center of the image. Thus, in this phase the robot moves from the second feature object towards the first feature object which takes from 7 to 82s. Finally, in the third phase, after reaching the first object, the robot moves towards the surface at 87s and tracks the desired path while interacts with the surface. The control results using the proposed and the other selected methods are presented in Figure 5.9. Referring to Figure 5.9, the proposed method tracks the desired signals with higher precision, lower chattering, and faster convergence rate both for vision and interacting force. In addition to the plots, to perform a comparative study, several numerical indicators such as integral absolute error (IAE), integral time absolute error (ITAE), standard deviation (STD), and root mean square

error (RMSE) indicators are computed for this test and tabulated in Table 5.1. Referring to this table, for the vision control, CISMV has decreased the values of IAE, ITAE, STD, and RMSE by 0.609%, 1.068%, 0.67%, and 0.95% compared to SMC, respectively. Compared to P/PI, these values are over 15.36%, 7.07%, 33.08%, and 8.38%. For the force control, CISMV has decreased the values of IAE, ITAE, STD, and RMSE by 22.15%, 43.3%, 1.13%, and 4.7% compared to P/PI, respectively. Compared to SMC, these values are over 32.7%, 63.73%, 9.82%, and 6.74%. The results show that the proposed hybrid controller results in improvement of the control performance in terms of chattering, precision, and convergence rate to a significant extent.

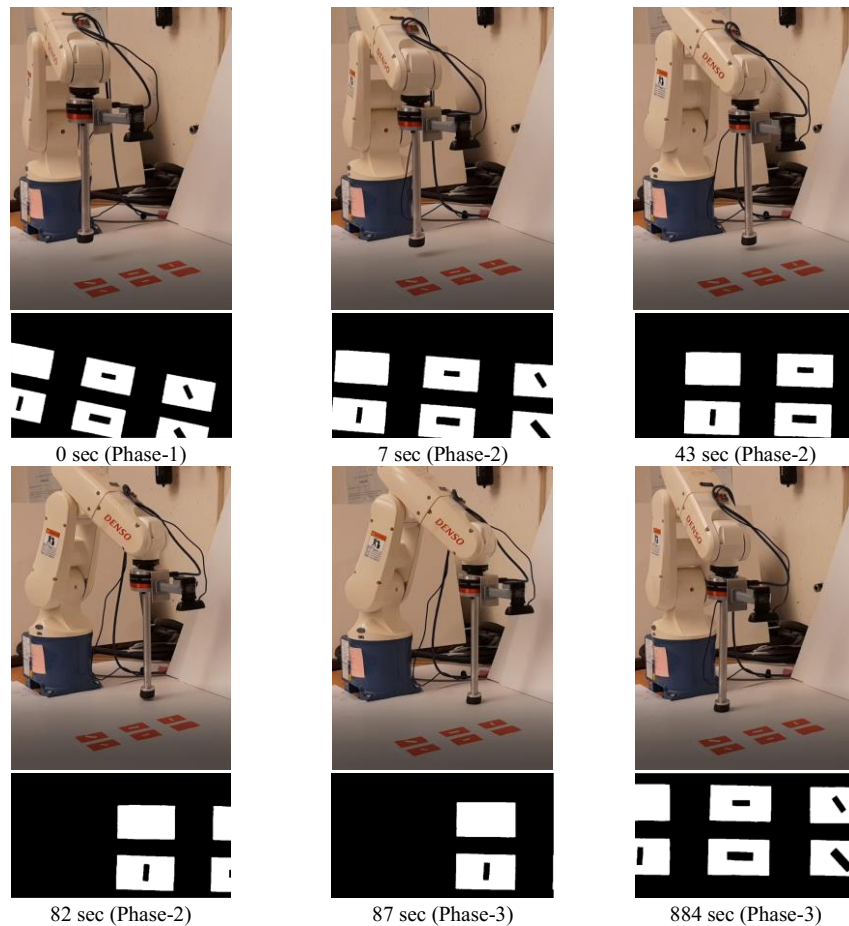


Figure 5.8: Robot operating the second test along with the captured image features in real time when the desired feature is not available in the FOV.

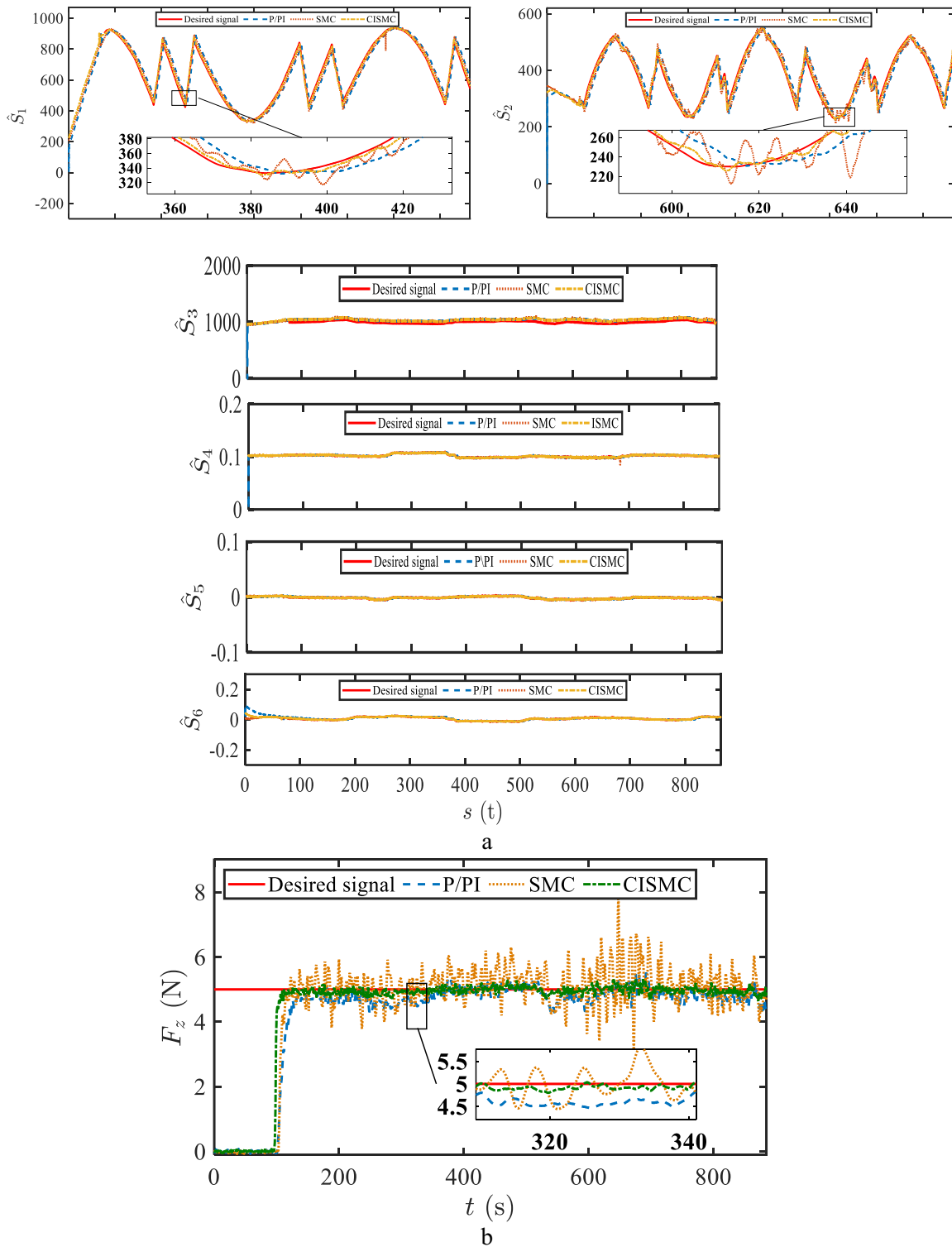


Figure 5.9: a) Tracking the desired vision signal using CISM compared with the P/PI and SMC b) Tracking the desired force signal using the P/PI, SMC and CISM.

Table 5.1: The computed values of the indicators for the norms of system errors of the third test.

	Comp.	Indicator			
		IAE	ITAE	STD	RMSE
Vision	P	2.8300E05	9.2646E07	346.56	398.54
	SMC	2.410E05	8.7023E07	233.47	368.65
	CISMC	2.3953E05	8.6093E07	231.89	365.14
Force	PI	676.58	1.1004E05	1.5865	1.7757
	SMC	782.87	1.7204E05	1.7393	1.8146
	CISMC	526.72	6.2389E04	1.5685	1.6923

5.6 Summary

In this chapter, a novel hybrid vision and force approach based on expanding the workspace is proposed for eye-in-hand industrial robots to address the FOV limitation of the interaction tasks on the workpiece. In the proposed method, a single object is replaced by an array of objects to expand the workspace for hybrid vision and force control using a novel hierarchical sliding surface with two levels of sliding surfaces. The first level contains the weighted sum of feature errors of all objects generated by the FIS and the second level contains the orthogonal terms of the first level and the error of the interaction force. Then, a CISMC is designed to lead the sliding surfaces towards zero and control the motion of the end-effector and the interaction force with the workpiece at the same time. To prove the effectiveness of the proposed method, two experimental tests are designed. In the first experiment, the effect of increasing the number of feature objects on the workspace enlargement is investigated. The result of obtained FOV using different number of objects demonstrate that the proposed method can expand the FOV which makes it a suitable method to be employed in industrial applications, where the robot needs to track a trajectory while

interacting with the workpiece. Then the performance of the proposed method is investigated in tracking a specified desired path in larger area. In the second test, the performance of the proposed method is investigated when the robot is located in a position far from the start point of the desired path. Also, the proposed controller is compared with the other well-known control systems to show its effectiveness in terms of precision, convergence rate, robustness, control effort, and chattering.

CHAPTER 6 Conclusion and Future Works

6.1 Summary of the Thesis

Integration of vision and force control systems has increased the dexterity and intelligence of industrial robots. This thesis focuses on vision and force control of the industrial robots using an image-based visual servoing (IBVS) which the features are taken by the vision system as a feedback in a robotic system to guide the robot to the desired pose. Researchers have introduced various methods in vision and force control to improve its performance. In this thesis, a series of new methods are proposed to overcome the current shortcomings. The proposed methods aim to increase the robustness of the vision and force control method to uncertainties and camera limitations and also overcome some of its drawbacks. In the following, the proposed methods are summarized:

1. Cascade Vision and Force Control

A robust cascade vision and force approach is suggested to control industrial robots interacting with unknown workpieces considering model uncertainties. This cascade structure, consisting of an inner vision loop and an outer force loop, avoids the conflict between the force and vision control in traditional hybrid methods without decoupling force and vision systems. To apply an advanced image-based visual servoing (IBVS) compensator, some newly modified image features are used which render an invertible image interaction matrix. A practical task-based method is proposed to extract the features corresponding to the desired path in 3D space. A robust continuous integral sliding mode control method (CISMC) is developed for both IBVS and force

compensators. CISMC exploits advantages of the modified super twisting algorithm (MSTA) to reduce the chattering. The stability of the proposed cascade controller is proved. Additionally, a contact detector algorithm (CDA) is developed to manage the robot's free motion and its interaction with the workpiece. To evaluate the performance of the proposed method, several experimental tests are performed and compared with other well-known methods.

2. Optimal Image-Based Task-Sequence/Path Planning

A novel image-based task-sequence/path planning scheme coupled with a robust vision and force control method for solving the multi-task operation problem of an eye-in-hand (EIH) industrial robot interacting with a workpiece is suggested. Each task is defined as tracking a predefined path or positioning to a single point on the workpiece's surface with a desired interacting force signal, i.e., Interaction with the workpiece. The proposed method suggests an optimal task sequence planning scheme to carry out all the tasks and an optimal path planning method to generate a collision-free path between the tasks, i.e., when the robot performs free-motion (pure vision control). To this end, a new method is presented which solve both optimal task sequence planning and collision-free path planning simultaneously. A novel modified artificial potential field (MAPF) is employed for generating the collision-free path between each two tasks in the three-dimensional (3D) environment. Rotational repulsive force on a parallel plan assigned to each object is considered which results in escaping from local minima. The parameters of the MAPF and the sequence of the tasks and their direction are found by an optimization algorithm at the same time. The overall optimization problem can be considered as a new modified artificial potential field-constrained generalized traveling salesman problem (MAPF-CGTSP), which is a mix-integer optimization problem. The mix-integer version of multi-tracker optimization algorithm (MTOA) is developed to solve the problem. Note that, since visual servoing is used for

robot motion control, the planning should be done in the image feature space which is the main challenge of the problem. Integrated with the proposed task/path planning, a novel chattering-free filtered quasi sliding mode control (FQSMC) method is specially designed for robust hybrid vision and force control of the EIH robot. FQSMC exploits a novel variable-gain orthogonal sliding manifold (VGOSM) for controlling vision and force to accomplish the tasks. FQSMC not only overcomes large uncertainties, but also filters out the existing noises by exploiting an intrinsic low-pass filter within its control law. It also enables the robot to switch between free-motion mode and interaction mode which is necessary for completing multiple tasks in an operation. Experimental results using an EIH Denso industrial robot show the effectiveness and superior performance of the proposed approach compared to other state-of-the-art methods.

3. Multi-Stage Hybrid Vision and Force

A novel multi-stage method for robust hybrid vision and force control of industrial robots, subject to model uncertainties. It aims to improve the performance of the three phases of the control process: a) free-motion using the image-based visual servoing (IBVS) before the interaction with the workpiece; b) the moment that the end-effector touches the workpiece; and c) hybrid vision and force control during the interaction with the workpiece. First, the camera motion is decomposed into transitional and angular movements. Then, utilizing a switching method, the rotational and translational movements of the camera are controlled in the first two stages, respectively. In the last stage, hybrid vision and force control is activated. For each stage, super-twisting sliding mode controller (STSMC) is utilized. Employing STSMC results in robustness against uncertainties while addressing the chattering problem. A variable-gain sliding surface is also proposed to address the instability and convergence speed issues of the traditional switch

IBVS. The experimental results demonstrated the effectiveness and superiority of the proposed multi-stage method compared to other traditional approaches.

4. Expansion of IBVS Workspace

A novel approach for hybrid vision and force control of eye-in-hand industrial robots is presented which addresses the problem of camera's field-of-view (FOV) limitation. During the interaction with the workpiece, the distance of the camera and the workpiece's surface is rather short. Thus, the FOV is very small which restricts the robot's workspace. To handle this issue, instead of using only a feature object, an array of objects is provided on the workpiece in a way that at least one object is entirely in the FOV. However, conventional IBVS and hybrid vision and force methods cannot be employed for such task. Thus, for this task, using a fuzzy inference system (FIS) and orthogonality principle, a novel hierarchical sliding surface is devised, and the continuous integral sliding mode controller (CISMC) is adopted, which leads to a robust and precise control method, applicable to the mentioned task.

6.2 Future Work

This thesis focuses on introducing new methods of Vision and force control. In the future work, it could be interesting to focus on a hybrid multi-camera framework conceived for an IBVS and force control of a collaborative robot that has to manipulate industrial pieces. The multi-camera approach overcomes the issues related to single-camera schemes, such as object occlusions and view-dependent errors. Also, the robustness design technique could be adopted to overcome the modeling errors and uncertainties of the acquired vision model. Another future work could be developing a sensor-less method for force measurement and designing

uncertainty/disturbance observer-based control approaches. Also, implementing the developed strategies to real applications such as deburring, polishing, etc. could be considered.

REFERENCES

- [1] P. I. Corke, “Visual control of robots: High Performance Visual Servoing,” in *Research Studies Press*, Australia, 1996.
- [2] F. F. Chaumette, “Potential problems of stability and convergence in image-based and position-based visual servoing,” *The confluence of vision and control*, vol. 237, pp. 66–78, 1998.
- [3] F. Chaumette and S. Hutchinson, “Visual servo control part I: basic approaches,” *IEEE Robot. Autom. Mag.*, vol. 13, no. 4, pp. 82–90, 2006.
- [4] M. Keshmiri, “Image based visual servoing using trajectory planning and augmented visual servoing controller,” Concordia University, 2014.
- [5] E. Malis, “2-1 / 2-D visual servoing,” *IEEE Trans. Robot. Autom.*, vol. 15, no. 2, pp. 238–250, 1999.
- [6] L. Villani and J. De Schutter, *Force Control*. Springer handbook of robotics, 2008.
- [7] C. C. Cheah, S. P. Hou, Y. Zhao, and J. J. E. Slotine, “Adaptive vision and force tracking control for robots with constraint uncertainty,” *IEEE/ASME Trans. Mechatronics*, vol. 15, no. 3, pp. 389–399, 2010.
- [8] G. Zeng and A. Hemami, “An overview of robot force control,” *Robotica*, vol. 15, no. 1997, pp. 473–482, 2016.
- [9] J. Marvel and J. Falco, “Best practices and performance metrics using force control for robotic assembly,” 2012.
- [10] N. Hogan, “Impedance control: an approach to manipulation,” in *American Control Conference*, pp. 304–313, 1984.
- [11] N. Mogan, “Impedance control : an approach to manipulation : Part II — implementation,” *J. Dyn. Syst. Meas. Control*, vol. 107, no. 1, pp. 8–16, 1985.
- [12] J. J. Craig and M. H. Raibert, “Hybrid position / force control of manipulators,” *J. Dyn. Syst. Meas. Control*, vol. 103, no. 2, 1981, pp. 126–133.
- [13] Hogan, “Impedance Control: an approach to manipulation,” in *1984 American Control Conference*, San Diego, CA, USA, 1984, pp. 304-313.

- [14] T. Kim et al., “Design and force-tracking impedance control of 2-DOF wall-cleaning manipulator via disturbance observer,” *IEEE/ASME Trans. Mechatronics*, vol. 25, No. 3, pp. 1487-1498, June 2020.
- [15] M. H. Reibert, “Hybrid position/force control of manipulators,” *ASME, J. Dyn. Syst. Meas. Control*, vol. 103, pp. 2–12, 1981.
- [16] Y. Zhang, C. Hua, and J. Qian, “Adaptive robust visual servoing/force control for robot manipulator with dead-zone input,” *IEEE Access*, vol. 7, pp. 129627–129636, 2019.
- [17] C. C. Cheah, S. P. Hou, Y. Zhao, and J.-J. E. Slotine, “Adaptive vision and force tracking control for robots with constraint uncertainty,” *IEEE/ASME Trans. Mechatronics*, vol. 15, no. 3, pp. 389–399, 2009.
- [18] Y. Zhao and C. C. Cheah, “Vision-based neural network control for constrained robots with constraint uncertainty,” *IET Control Theory Appl.*, vol. 2, no. 10, pp. 906–916, 2008.
- [19] S. Hutchinson and F. Chaumette, “Visual servo control, part i: basic approaches,” *IEEE Robot. Autom. Mag.*, vol. 13, no. 4, pp. 82–90, 2006.
- [20] S. Li, A. Ghasemi, W. -F. Xie, and Y. Gao, “An enhanced IBVS controller of a 6DOF manipulator using hybrid PD-SMC method,” *Int. J. Control. Autom. Syst.*, vol. 16, no. 2, pp. 844–855, 2018.
- [21] E. C. Dean-León, V. Parra-Vega, and A. Espinosa-Romero, “Visual servoing for constrained planar robots subject to complex friction,” *IEEE/ASME Trans. Mechatronics*, vol. 11, no. 4, pp. 389–400, 2006.
- [22] H. Wang, H. Ni, J. Wang, and W. Chen, “Hybrid vision and force control of soft robot based on a deformation model,” *IEEE Trans. Control Syst. Technol.*, pp. 1-11, 2019.
- [23] S. Liu et al., “Robust insertion control for precision assembly with passive compliance combining vision and force information,” *IEEE/ASME Trans. Mechatronics*, vol. 24, no. 5, pp. 1974–1985, 2019.
- [24] Y. Mezouar, M. Prats, and P. Martinet, “External hybrid vision and force control,” in *Intl. Conference on Advanced Robotics (ICAR07)*, Daegu, South Korea, 2007, pp. 170–175.
- [25] J. Hu, C. Li, Z. Chen and B. Yao, “Precision motion control of a 6-DoFs industrial robot with accurate payload estimation,” *IEEE/ASME Trans. Mechatronics*, vol. 25, no. 4, pp. 1821-1829, 2020.
- [26] W. Deng and J. Yao, “Extended-state-observer-based adaptive control of electrohydraulic servomechanisms without velocity measurement,” *IEEE/ASME Trans. Mechatronics*, vol. 25, no. 3, pp. 1151-1161, 2020.
- [27] C. Wong, C. Mineo, E. Yang, X. -T. Yan and D. Gu, “A novel clustering-based algorithm for solving spatially-constrained robotic task sequencing problems,” *IEEE/ASME Transactions on Mechatronics*, to be published, DOI: 10.1109/TMECH.2020.3037158.

- [28] W. Xuewu, Y. Shi, D. Ding, and X. Gu “Double global optimum genetic algorithm particle swarm optimization-based welding robot path planning,” *Engineering Optimization*, vol. 48, no. 2, pp. 299–316, 2016.
- [29] Z. Han et al., “Towards mobile multi-task manipulation in a confined and integrated environment with irregular objects,” in *IEEE International Conference on Robotics and Automation (ICRA)*, 2020, pp. 11025-11031.
- [30] P. Kurtser and Y. Edan. “Planning the sequence of tasks for harvesting robots,” *Robotics and Autonomous Systems*, vol. 131, pp. 103591, Sep. 2020.
- [31] S. Diyaley, A. Aditya, and S. Chakraborty, “Optimization of the multi-hole drilling path sequence for concentric circular patterns,” *Opsearch*, vol. 57, no. 3, pp. 746–764, 2020.
- [32] A. Kovcs, “Integrated task sequencing and path planning for robotic remote laser welding,” *Int. J. Prod. Res.*, vol. 54, no. 4, pp. 1210–1224, Feb. 2016.
- [33] X. Xu, Y. Hu, J. M. Zhai, L. Z. Li, and P. S. Guo, “A novel non-collision trajectory planning algorithm based on velocity potential field for robotic manipulator,” *Int. J. Adv. Robot. Syst.*, vol. 15, no. 4, pp. 1-13, Jul. 2018.
- [34] S.-O. Park, M. C. Lee, and J. Kim, “Trajectory planning with collision avoidance for redundant robots using jacobian and artificial potential field-based real-time inverse kinematics,” *Int. J. Control. Autom. Syst.*, vol. 18, no. 8, pp. 2095–2107, 2020.
- [35] T. Zhao, H. Li, and S. Dian, “Multi-robot path planning based on improved artificial potential field and fuzzy inference system,” *J. Intell. Fuzzy Syst.*, vol. 39, pp. 7621–7637, 2020.
- [36] M. ismet Can, “Position/force control of robot manipulators”, M.S. thesis, Dept. Mech. Eng., METU, 2003.
- [37] O. R. Ulises, O. Montiel and R. Sepulveda, “Hybrid path planning algorithm based on membrane pseudo-bacterial potential field for autonomous mobile robots,” *IEEE Access*, vol. 7, pp.156787-156803, 2019.
- [38] O. R. Ulises, O. Montiel and R. Sepulveda, “Mobile robot path planning using membrane evolutionary artificial potential field,” *Applied Soft Computing*, vol. 77, pp. 236-251, 2019.
- [39] A. Alaa, T. Y. Abdalla and A. A. Abed. “Path planning of mobile robot by using modified optimized potential field method,” *International Journal of Computer Applications.*, vol. 113, no. 4, pp. 6-10.
- [40] A. Ameni and K. Nouri, “An advanced potential field method proposed for mobile robot path planning,” *Transactions of the Institute of Measurement and Control*, vol. 41, no. 11, pp. 3132-3144, 2019.

- [41] Y. Zhang, C. Hua, and J. Qian, "Adaptive robust visual servoing/force control for robot manipulator with dead-zone input," *IEEE Access*, vol. 7, pp. 129627–129636, 2019.
- [42] X. Yu, W. He, Q. Li, Y. Li and B. Li, "Human-robot co-carrying using visual and force sensing," *IEEE Transactions on Industrial Electronics*, vol. 68, no. 9, pp. 8657-8666, Sept. 2021, doi: 10.1109/TIE.2020.3016271.
- [43] H. Wang, H. Ni, J. Wang and W. Chen, "Hybrid vision and force control of soft robot based on a deformation model," *IEEE Transactions on Control Systems Technology*, vol. 29, no. 2, pp. 661–671, Dec. 2019.
- [44] J. Baeten, H. Bruyninckx, and J. D. Schutter, "Tool/camera configurations for eye-in-hand hybrid vision and force control," in *IEEE International Conference on Robotics and Automation*, Washington, DC, May 2002, pp. 1704-1709.
- [45] F. Schramm and G. Morel, "Ensuring visibility in calibration-free path planning for image-based visual servoing," *IEEE Transactions on Robotics*, vol. 22, no. 4, pp. 848-854, Aug. 2006.
- [46] M. Keshmiri and W. Xie, "Image-based visual servoing using an optimized trajectory planning technique," *IEEE/ASME Transactions on Mechatronics*, vol. 22, no. 1, pp. 359-370, Feb. 2017.
- [47] B. Ahmadi, W. -F. Xie and E. Zakeri, "Robust cascade vision and force control of industrial robots utilizing continuous integral sliding mode control method," *IEEE/ASME Transactions on Mechatronics*, doi: 10.1109/TMECH.2021.3067619.
- [48] A. Vakanski, F. Janabi-Sharifi, and I. Mantegh, "An image-based trajectory planning approach for robust robot programming by demonstration," *Rob. Auton. Syst.*, vol. 98, pp. 241–257, 2017.
- [49] M. Kazemi, K. Gupta, and M. Mehrandezh. "Randomized kinodynamic planning for robust visual servoing." *IEEE Transactions on Robotics*, vol. 29, no. 5, pp. 1197-1211, 2013.
- [50] A. Hajiloo, M. Keshmiri, W. F. Xie, and T. T. Wang. "Robust online model predictive control for a constrained image-based visual servoing," *IEEE Transactions on Industrial Electronics*, vol. 63, no. 4, pp. 2242-2250, 2015.
- [51] D. Nicolis, M. Palumbo, A.M. Zanchettin, and P. Rocco. "Occlusion-free visual servoing for the shared autonomy teleoperation of dual-arm robots," *IEEE Robotics and Automation Letters*, vol. 3, no.2, pp.796-803, 2018.
- [52] M. Youcef, and F. Chaumette. "Path planning for robust image-based control," *IEEE transactions on robotics and automation*, vol. 18, no. 4 pp. 534-549, 2002.
- [53] T. Shen and G. Chesi. "Visual servoing path planning for cameras obeying the unified model" *Advanced Robotics*, Vol. 26, no. (8-9), pp. 843–860, 2012.
- [54] A. Ghasemi, P. Li, W.F Xie and W. Tian "Enhanced switch image-based visual servoing dealing with featuresloss," *Electronics*, Vol. 8, no. 8, pp. 903, 2019.

- [55] E. Zakeri et al., "Path planning for unmanned underwater vehicle in 3D space with obstacles using spline-imperialist competitive algorithm and optimal interval type-2 fuzzy logic controller," *Lat. Am. J. Solids Struct.*, vol. 13, no. 6, pp. 1054–1085, 2016.
- [56] E. Zakeri, S. A. Moezi, and M. Eghtesad, "Optimal interval type-2 fuzzy fractional order super twisting algorithm: a second order sliding mode controller for fully-actuated and under-actuated nonlinear systems," *ISA Trans.*, vol. 85, pp. 13–32, 2019.
- [57] Y. Pan, C. Yang, L. Pan, and H. Yu, "Integral sliding mode control: performance, modification, and improvement," *IEEE Trans. Ind. Informatics*, vol. 14, no. 7, pp. 3087–3096, 2017.
- [58] S. Akhlaghi, N. Zhou and Z. Huang, "Adaptive adjustment of noise covariance in Kalman filter for dynamic state estimation," in *2017 IEEE Power & Energy Society General Meeting*, Chicago, IL, 2017, pp. 1-5.
- [59] E. Moulay and W. Perruquetti, "Finite time stability and stabilization of a class of continuous systems," *J. Math. Anal. Appl.*, vol. 323, no. 2, pp. 1430–1443, 2006.
- [60] K. Xiong, H. Zhang and L. Liu, "Adaptive robust extended Kalman filter for nonlinear stochastic systems," *IET Control Theory & Applications*, vol. 2, no. 3, pp. 239-250, 2008.
- [61] J. A. Moreno and M. Osorio, "A Lyapunov approach to second-order sliding mode controllers and observers," in *2008 47th IEEE Conference on Decision and Control*, Cancun, 2008, pp. 2856-2861.
- [62] H. Khosravi, E. Zakeri, W.F. Xie, and B. Ahmadi, "Adaptive multi-tracker optimization algorithm for global optimization problems: emphasis on applications in chemical engineering," *Engineering with Computers*, pp. 1-28, 2020.
- [63] S. Katoch, S. S. Chauhan, and V. Kumar. "A review on genetic algorithm: past, present, and future," *Multimedia Tools and Applications*, vol. 80, no. 5, pp. 8091-8126, 2021.
- [64] F. Wang, H. Zhang and A. Zhou, "A particle swarm optimization algorithm for mixed-variable optimization problems," *Swarm and Evolutionary Computation*, vol. 60, pp.100808, 2021.
- [65] P. Hao and B. Sobhani, "Application of the improved chaotic grey wolf optimization algorithm as a novel and efficient method for parameter estimation of solid oxide fuel cells model," *International Journal of Hydrogen Energy*, vol. 46, no.73, pp.36454-36465, 2021.
- [66] E. Zakeri, S. A. Moezi, Y. Bazargan-Lari, and A. Zare, "Multi-tracker Optimization Algorithm: A General Algorithm for Solving Engineering Optimization Problems," *Iran. J. Sci. Technol. - Trans. Mech. Eng.*, vol. 41, no. 4, 2017, doi: 10.1007/s40997-016-0066-9.
- [67] M.T. Hagan, H.B. Demuth, and M. Beale, in *Neural Network Design*. PWS Publishing Co., 1996.
- [68] K. Shojaei, A. Kazemy and A. Chatraei, "An Observer-Based Neural Adaptive PID 2 controller for robot manipulators including motor dynamics with a prescribed performance," *IEEE/ASME Transactions on Mechatronics*, vol. 26, no. 3, pp. 1689-1699, June 2021.

- [69] I. Mohsin, K. He, Z. Li, and R. Du, "Path planning under force control in robotic polishing of the complex curved surfaces," *Applied Sciences*, vol. 9, no. 24, pp. 5489, 2019.
- [70] F. Tian, C. Lv, Z. Li, and G. Liu, "Modeling and control of robotic automatic polishing for curved surfaces," *CIRP Journal of Manufacturing Science and Technology*, vol. 14, pp. 55-64, 2016.
- [71] F. Tian, Z. Li, C. Lv and G. Liu, "Polishing pressure investigations of robot automatic polishing on curved surfaces," *The International Journal of Advanced Manufacturing Technology*, vol. 87, no. 1, pp. 639-646, 2016.
- [72] S. S. Ge and Y. J. Cui, "Dynamic motion planning for mobile robots using potential field method," *Auton. Robots*, vol. 13, no. 3, pp. 207-222, 2002.
- [73] J. S. Smith, B. Wu and B. M. Wilamowski, "Neural network training with Levenberg-Marquardt and adaptable weight compression," *IEEE Transactions on Neural Networks and Learning Systems*, vol. 30, no. 2, pp. 580-587, Feb. 2019.
- [74] S. M. Kay, "Fundamentals of statistical signal processing: estimation theory," *PTR Prentice Hall International, Inc.*, Englewood Cliffs, New Jersey, 1993.
- [75] A. Ghasemi, P. Li, and W. F. Xie, "Adaptive switch image-based visual servoing for industrial robots," *Int. J. Control. Autom. Syst.*, vol. 18, no. 5, pp. 1324-1334, 2020.
- [76] M. G. Krishnan and S. Ashok, "Adaptive gain control law for visual servoing of 6DOF robot manipulator," in *2018 International Conference on Control, Power, Communication and Computing Technologies (ICCPCCT)*, Kannur, 2018, pp. 57-64.
- [77] A. San-Miguel, V. Puig and G. Alenyà, "Disturbance observer-based LPV feedback control of a N-DOF robotic manipulator including compliance through gain shifting," *Control Engineering Practice*, vol. 115, pp. 104887, 2021.
- [78] C.-F. Huang, T.-L. Liao, C.-Y. Chen, and J.-J. Yan, "The design of quasi-sliding mode control for a permanent magnet synchronous motor with unmatched uncertainties," *Comput. Math. with Appl.*, vol. 64, no. 5, pp. 1036-1043, 2012.
- [79] Z. Li, W.-F. Xie, X.-W. Tu, and C. Perron, "Switching control of image based visual servoing with laser pointer in robotic assembly systems," in *2007 IEEE International Conference on Systems, Man and Cybernetics*, 2007, pp. 2383-2389.
- [80] A. Ghasemi, P. Li, and W.-F. Xie, "Adaptive switch image-based visual servoing for industrial robots," *Int. J. Control. Autom. Syst.*, vol. 18, no. 5, pp. 1324-1334, 2020.
- [81] L. Fridman and A. Levant, "Sliding mode control in engineering, chapter 3 'higher order sliding modes'" *Marcel Dekker*, 2002, pp. 53-101.
- [82] L. A. Zadeh, "Fuzzy sets," in *Fuzzy sets, fuzzy logic, and fuzzy systems: selected papers by Lotfi A Zadeh*, World Scientific, 1996, pp. 394-432.

- [83] C. P. Bechlioulis, S. Heshmati-alamdari, G. C. Karras and K. J. Kyriakopoulos, “Robust image-based visual servoing with prescribed performance under field of view constraints,” in *IEEE Transactions on Robotics*, vol. 35, no. 4, pp. 1063-1070, Aug. 2019, doi: 10.1109/TRO.2019.2914333.
- [84] L. Villani and J. De Schutter, “Force control,” in *Springer Handbook of Robotics*, B. Siciliano and O. Khatib, Eds. Berlin, Heidelberg: Springer Berlin Heidelberg, 2008, pp. 161–185.
- [85] Grasping objects on conveyor belts. [Online]. Available: <https://www.machinedesign.com/robotics/baxter-robot-rest-us>.
- [86] Robotic fruit picking. [Online]. Available: <https://strawberryplants.org/strawberry-picking-robot>.
- [87] da vinci. [Online]. Available: <https://www.engadget.com/2009/04/07/video-da-vinci-si-robotic-system-wants-to-be-your-surgeon/>
- [88] J. Markoff, “Google cars drive themselves, in traffic,” *Newyork Times*, p. A1, Oct., 9, 2010.